Different Methods to Constrain Dark Matter

by

Youjia Wu

A dissertation submitted in partial fulfillment
of the requirements for the degree of
Doctor of Philosophy
(Physics)
in The University of Michigan
2022

Doctoral Committee:

       Professor Dragan Huterer, Chair
       Professor Eric Bell
       Professor Katherine Freese
       Professor Wolfgang Lorenzon
       Professor Monica Valluri

Youjia Wu

youjiawu@umich.edu

ORCID iD: 0000-0002-7399-1306

For all the people

ACKNOWLEDGEMENTS

TABLE OF CONTENTS

LIST OF FIGURES

Figure

ABSTRACT

The currently favored cosmological model suggests that over 85% of the matter in our universe is dark, yet the existence of dark matter is still to be confirmed by detecting it through interactions with normal matter. Direct detection experiments hope to observe signals from the scattering of dark matter particles off of cryogenic target nuclei. A null result from direct detection leads to an exclusion curve in the cross section-dark matter particle mass parameter space. Theoretical predictions for exclusion curves involve standard halo model, in which three astrophysical parameters are assumed to control the distribution of dark matter in the Milky Way. This thesis first discusses the uncertainties in these three parameters on the exclusion curve from the XENON1T experiment. Our estimate done with Monte Carlo simulations shows that at a low WIMP mass, the uncertainty in cross section can span six orders of magnitude.

Dark matter self-annihilation might power the first-generation stars and form Dark Stars. The possibility of Dark Stars was originally proposed in the context of Weakly Interacting Massive Particle (WIMP) model. Although the WIMP model is successful in explaining large structures in the universe, it faces difficulties when applied to structures as small as dwarf galaxies. To overcome the small-structure problems, self-interactions between dark matter particles are introduced and the Self-Interacting Dark Matter (SIDM) model was proposed. In the second part of this thesis, we evaluate the probability that Dark Stars can be powered by SIDM. We first propose a simple particle physics model of SIDM that satisfies all the current constraints, and work out the phase space region in which Dark Stars can form.

Then we investigate the gravothermal evolution of SIDM minihalos in the presence of a gas potential, and investigate whether it can lead to a sufficiently high dark matter density for Dark Stars to form. Finally, we present the first study of the properties of Dark Stars assuming they can reach hydrostatic equilibrium.

Dark matter is a major player in the formation of Milky Way-like galaxies. Different dark matter models lead to a different accretion history of Milky Way-like galaxies. This thesis finally studies the recent accretion history of Milky Way-like galaxies using statistical cluster analysis. Stars from the same accreted satellite galaxy are clustered in action space. Since actions are conserved in slow enough gravitational evolution, the accreted satellites should remain clustered until today. We apply the cluster analysis algorithm Enlink to accreted star particles in action space from the halos of three simulated Milky Way-like galaxies in the FIRE-2 simulations. We compare the groups found by our cluster analysis with the actual accreted satellites from these galaxies, and find the well-recovered satellites. The results show that the member stars of satellites which fell into the galaxy less than 7.1 Gyr ago and were more massive than 4.0×10^8 solar mass can be well recovered by cluster analysis.

CHAPTER I

Introduction

The eagerness of humankind to know about the universe can be dated back to ancient times. The first cosmological model was probably the one proposed by Aristotle, saying that Earth is located at the center of the universe, and every other celestial object is orbiting around Earth. Galileo inspired the idea that natural phenomena can be studied quantitatively, signaling the beginning of Scientific Revolution. In 1687, Newton published his law of universal gravity and showed that the celestial and terrestrial gravitational forces have the same underlying physical cause. The law of universal gravity plus his laws of motion provide people with the power to understand the motions of astronomical objects, and can be marked as the beginning of serious cosmology.

The cosmological branch of physics developed rapidly in the 20th century. The observational data of different scales, from different sources, and with different probes culminated in the widely accepted cosmological model — the ΛCDM model, with Λ referring to cosmological constant or dark energy, and CDM referring to cold dark matter. Dark energy is, by definition, the driving force of the current accelerated expansion of the universe. Cold dark matter is cold because its particles are non-relativistic when it affects the formation of galaxies, and is dark because it doesn't participate in electromagnetic interactions and therefore doesn't emit photons. These

two components remain elusive to us. In this thesis, we will focus on dark matter, and more specifically, three probes that can constrain the properties of dark matter: direct detection, Dark Stars and galaxy accretion history. To start the discussion of these topics in detail, we will first introduce the ΛCDM model in general, specifically dark matter.

In this chapter, we will present an overview of the ΛCDM model in Section 1.1. A brief summary of the observational motivations for dark matter will be given in Section 1.2. We will then discuss dark matter models in Section 1.3. Based on dark matter particle models, direct detection experiments are designed to find evidence of dark matter particles. We review this topic in Section 1.4. Since dark matter particles are presumed to exist everywhere and have a long lifetime, we can trace back to the era with redshift $z = 10 - 50$ and study the effects of dark matter particles on the formation of first stars. The self-annihilation of dark matter could power the first stars. These dark matter powered stars are called Dark Stars. An overview of Dark Stars is in Section 1.5. Dark matter assembles itself to form halos which can host galaxies. We can study the stellar properties of long-living stars to infer their birthplaces and therefore investigate the assembly history of galaxies. This topic is vividly referred to as galactic archaeology. We will give a brief introduction to galactic archaeology in Section 1.6.

1.1 Big-Bang Cosmology

People have known matter and radiation as two components of the universe for a long time. The currently favored model ΛCDM indicates two additional important but elusive components exist in our cosmological model: dark energy and cold dark matter. In this model, the universe was created in a Big Bang, and then went through an exponential expansion phase called inflation. The inflation phase lasted for a short period of time and the details of that phase remain unclear to us. Then the universe

slowed down in expansion, cooled down, and created different "flavors" of particles. This process is continuing to the present day.

In cosmology, we use scale factor a to describe the size of the universe compared with today. As the universe expands, the wavelength of photons emitted at ancient times (when a is smaller) gets stretched and becomes longer than emitted when observed today. This effect is called cosmic redshift, and the amount of redshift z is related to the scale factor a by:

$$a = \frac{1}{1+z}.$$ (1.1)

Therefore, smaller a and larger z correspond to earlier periods in the cosmological history, while $a = 1$ or $z = 0$ refers to the present day. The time evolution of the scale parameter a is described by the **Friedmann Equations**:

$$\left(\frac{\dot{a}}{a}\right)^2 = \frac{8\pi G\rho}{3} - \frac{k}{a^2},$$ (1.2)

and

$$\frac{\ddot{a}}{a} = -\frac{4\pi G}{3}(\rho + 3P),$$ (1.3)

where the dot sign indicates the time derivative, G is gravitational constant, ρ is the mass or energy density, P is the pressure, and k is the curvature parameter. A flat universe with $k = 0$ is consistent with the observational evidence (see Ref. [11] for a recent measurement of k). Another useful equation derived from the first law of thermodynamics is:

$$\dot{\rho} = -3H(\rho + P).$$ (1.4)

The combination of $\frac{\dot{a}(t)}{a(t)}$ indicates the expansion rate of the universe, and is the **Hubble parameter**. The current value of Hubble parameter is usually expressed as:

$$H_0 = 100h \text{ km/s/Mpc},$$ (1.5)

where $h = 0.674$ from the *Planck* 2015 results [11].

The energy density corresponding to the flat universe ($k = 0$) is called the **critical density** ρ_{crit}. The current value of critical density is measured to be [11]:

$$\rho_{\text{crit}} = \frac{3H_0^2}{8\pi G} = 4.79 \times 10^{-4} \text{ GeV/cm}^{-3}, \tag{1.6}$$

The critical density includes contributions from different components, such as matter, radiation, dark energy... The relative densities of components are defined as:

$$\Omega_{\text{comp}}(t) = \frac{\rho_{\text{comp}}(t)}{\rho_{\text{crit}}(t)}, \tag{1.7}$$

where the variables are written as functions of time to emphasize the time dependence. Different components are distinguished by different equations of state:

$$P = w\rho. \tag{1.8}$$

With this equation of state, Eqn. 1.4 can be integrated to give out:

$$\rho \propto a^{-3(1+w)}. \tag{1.9}$$

For radiation, $w = \frac{1}{3}$, and $\rho \propto a^{-4}$; for non-relativistic matter without pressure, $w = 0$, and $\rho \propto a^{-3}$; for dark energy, $w = -1$, and $\rho = $ constant. Dark energy is also called cosmological constant due to its constant density as the universe expands. This ρ dependence on scale factor a can be plugged back into the Friedmann Equation 1.2 to get the time evolution of a (when $w \neq -1$ and setting the curvature parameter k to 0):

$$a(t) \propto t^{2/[3(1+w)]}, \tag{1.10}$$

i.e., a matter or radiation dominated universe will expand as a power law in time.

When $w = -1$, the density is constant, and a increases exponentially with time:

$$a(t) \propto e^{\sqrt{\frac{\Lambda}{3}}t}, \tag{1.11}$$

where $\Lambda \propto \rho_{\text{dark energy}}$ is the cosmological constant. Therefore, a universe dominated by dark energy will experience an exponential expansion.

Observations of Type Ia supernovae (e.g. Supernova Cosmology Project and the High-z Supernova Search Team), cosmic microwave background (CMB) (e.g. *WMAP* and *Planck* satellites), and galaxy clustering (e.g. Sloan Digital Sky Survey (SDSS) and Dark Energy Survey (DES)) can give constraints on the cosmological parameters, including relative densities of different components. Fig. 1.1 shows one slice of the 3D galaxy map from the data collected in a few months by DESI. The colored points are galaxies and the dark regions are not explored by DESI. Fig. 1.3 shows the angular spectrum of the correlation of temperature fluctuations in CMB. The overall shape of the spectrum can constrain many cosmological parameters. The current relative densities of radiation (Ω_γ), matter (Ω_m) and dark energy (Ω_Λ) are measured using the probes mentioned above: $\Omega_\gamma = 5.38(15) \times 10^{-5}, \Omega_m = 0.315(7), \Omega_\Lambda = 0.685(7)$. This distribution of relative densities indicates that the current universe is dominated by dark energy, so the universe is experiencing accelerated expansion, as shown in Equation 1.11. Many lines of evidence indicate the existence of not only baryonic matter, but also a non-baryonic component, or **dark matter**. The relative densities of baryonic matter (Ω_b) and dark matter (Ω_χ) are: $\Omega_b = 0.0493(6), \Omega_\chi = 0.265(7)$. We will have a more detailed discussion of dark matter in the following few Sections in this Chapter. All of the component relative density values are taken from the most recent Review of Particle Physics [11].
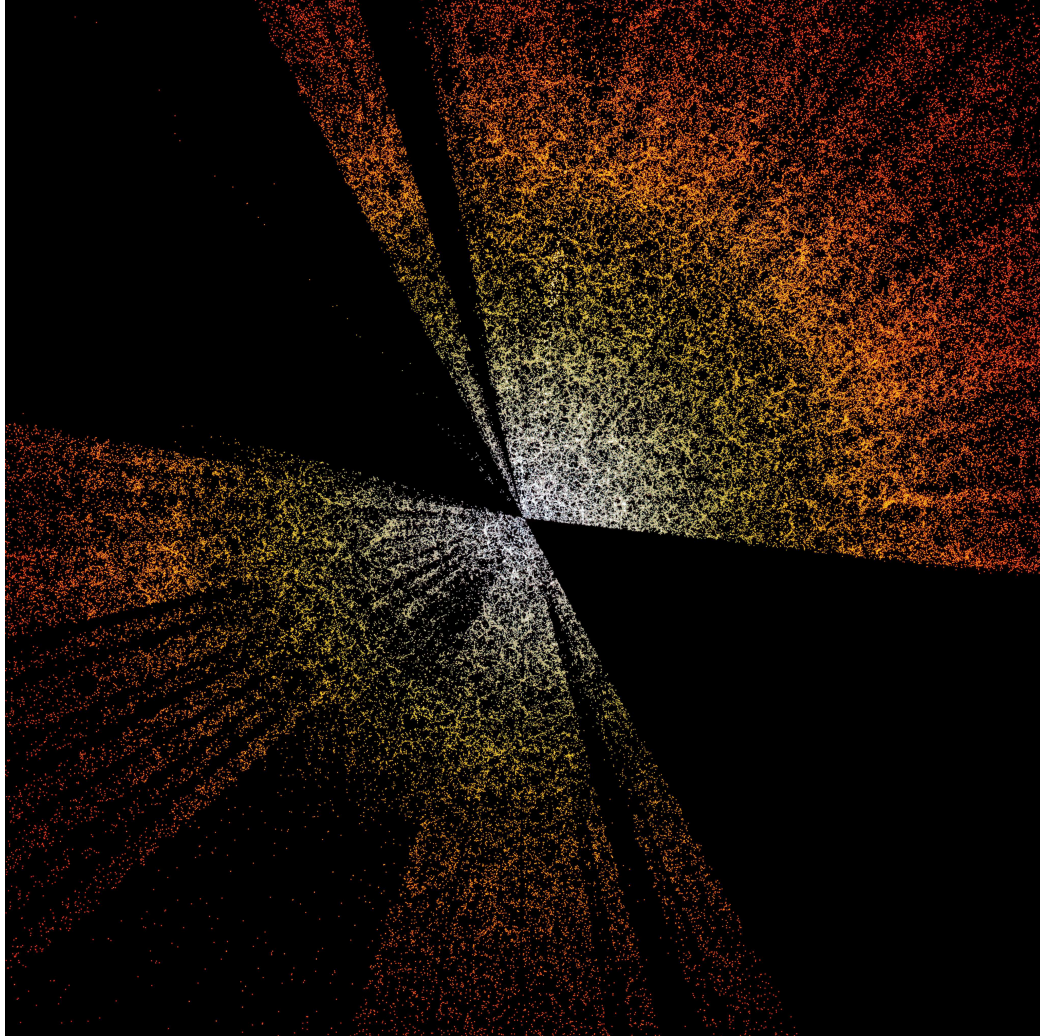
Figure 1.1: A slice of the 3D map of galaxies from the data collected in a few months by DESI. Each colored point represents one galaxy, with a total of 800 thousand galaxies on this slice. We are located at the center of the figure. The dark regions are not explored by DESI. (Credit: D. Schlegel/Berkeley Lab using data from DESI; Acknowledgement: M. Zamani (NSF's NOIRLab))

1.2   Observational evidence for Dark Matter

The first evidence of dark matter can be dated back to 1930s, when Fritz Zwicky analyzed dynamics of galaxies in one galaxy cluster and found mass-to-light ratio in it to be $\gg 1$ [12]. From then on, more and more observational evidence of dark matter has become available. This section will present a summary of some of the most important clues.

The Dynamics of galaxy clusters. In 1937, Fritz Zwicky published an article on the dynamical analysis of galaxies in the Coma galaxy cluster [13]. In this article, Zwicky applied the virial theorem to estimate the total mass of the Coma galaxy cluster using the observed velocity dispersion of galaxies in this cluster. The average mass of galaxies in the cluster was then calculated given the estimate of number of galaxies. With an accepted common average absolute luminosity of galaxies at that time, Zwicky inferred a surprisingly high mass-to-light ratio of 500, in contrast with the mass-to-light ratio of 4 in the solar neighborhood. Shortly thereafter, in 1936 Sinclair Smith estimated the dynamical mass of the Virgo Cluster [12], and obtained a dynamical mass around two orders of magnitude higher than the luminous mass. Many theories have been proposed to explain this discrepancy. One of them argued that the extra mass should come from intergalactic gas in the cluster [14; 15]. However, later observations of the X-ray emission [16] showed that gas can only contribute 2% of the mass to explain the dynamics. With the other theories within the framework of baryonic mass eventually ruled out [17; 18], the non-baryonic dark matter theory became favored.

The Galactic Rotation Curves. Galactic rotation curves depict the circular velocity of stars or gas around the center of a galaxy as a function of the distance from the galactic center. If the mass distribution in galaxies follow the distribution of stellar luminosity, then the rotational curve should experience a Keplerian fall-off $v(r) \propto 1/\sqrt{r}$ when r is larger than the optical radius of a galaxy. However, in

the 1970s, many authors [19; 20; 21; 22; 23] reported that, based on both radio and optical observations, the rotational curves in a lot of galaxies are actually flat instead of decreasing with r beyond the optical radius of galaxies. Fig. 1.2 shows an example of the flat rotation curve of the spiral galaxy NGC 3198 from Ref. [1]. The data observational data are presented as points with error bars, while the curves are fits that assume a halo+disk model. Much more non-luminous mass is required beyond the central region of galaxies to produce these flat rotation curves.

Structure Formation in the Universe. Many structures of different scales exist today in the universe, indicating that the contrast of baryonic density in the universe $\delta_b = \frac{\rho_b - \bar{\rho}_b}{\bar{\rho}_b} >> 1$, where δ_b describes the fluctuation of energy density of baryons. The CMB observations show that, in the era of recombination ($z \approx 1000$), this contrast $\delta_b \approx 10^{-5}$. Cosmological calculations show that the contrast grows by a factor of 10^3 between recombination and now if only baryonic mass is present, which would imply a predicted value of $\delta_b \approx 10^{-2}$ at $z = 0$. This result is in contrast with our observation above, that $\delta_b >> 1$, indicating that extra non-baryonic mass is enhancing the structure formation.

The Structure of Cosmic Microwave Background (CMB) peaks. ΛCDM model explains the structure of CMB peaks very well. The observed CMB angular variation in temperature correlations (TT spectrum) from *Planck* 2015 results [2] and its ΛCDM fitting is shown in Fig. 1.3. With the CMB spectrum we can very accurately constrain the parameters in ΛCDM, including the total mass abundance and total cold dark matter abundance today. Fig. 1.4 taken from Ref. [3] plots the reaction of CMB spectrum under the change of four parameters in ΛCDM: (a) curvature represented with Ω_{tot} (b) relative dark energy density Ω_Λ (c) physical baryon relative density $\Omega_b h^2$ (d) physical mass relative density Ω_m. These panels shows that the shape of CMB spectrum is sensitive to the changes in these four parameters.

DISTRIBUTION OF DARK MATTER IN NGC 3198
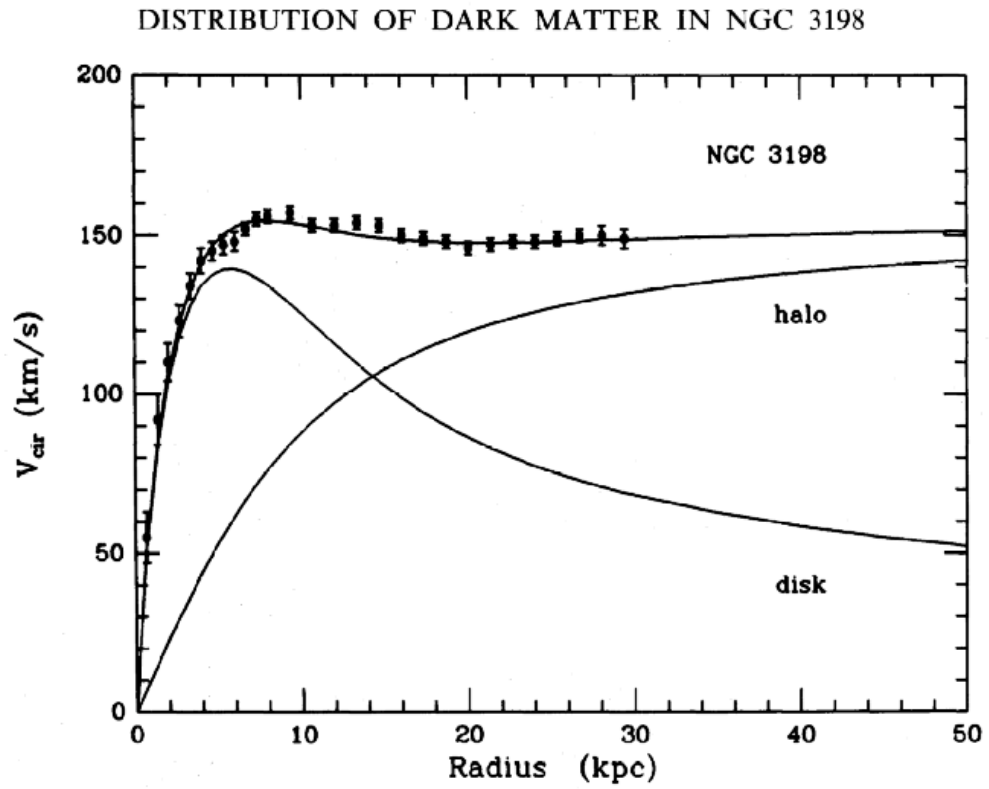
Figure 1.2: Flat rotation curve of galaxy NGC 3198. The data points with error bars are the observations, while the curves are fits that assume a halo+disk model. This figure is taken from Ref. [1].
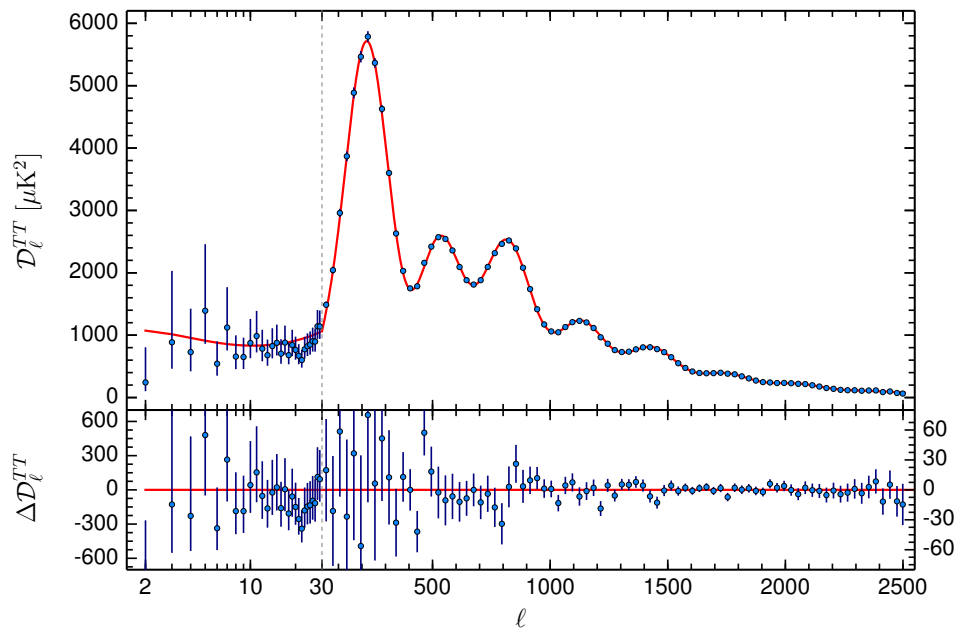
Figure 1.3: CMB angular power spectrum of temperature fluctuations taken from *Planck* 2015 results [2]. The blue data points with error bars are the observations, while the red line shows the best fitting from ΛCDM model.
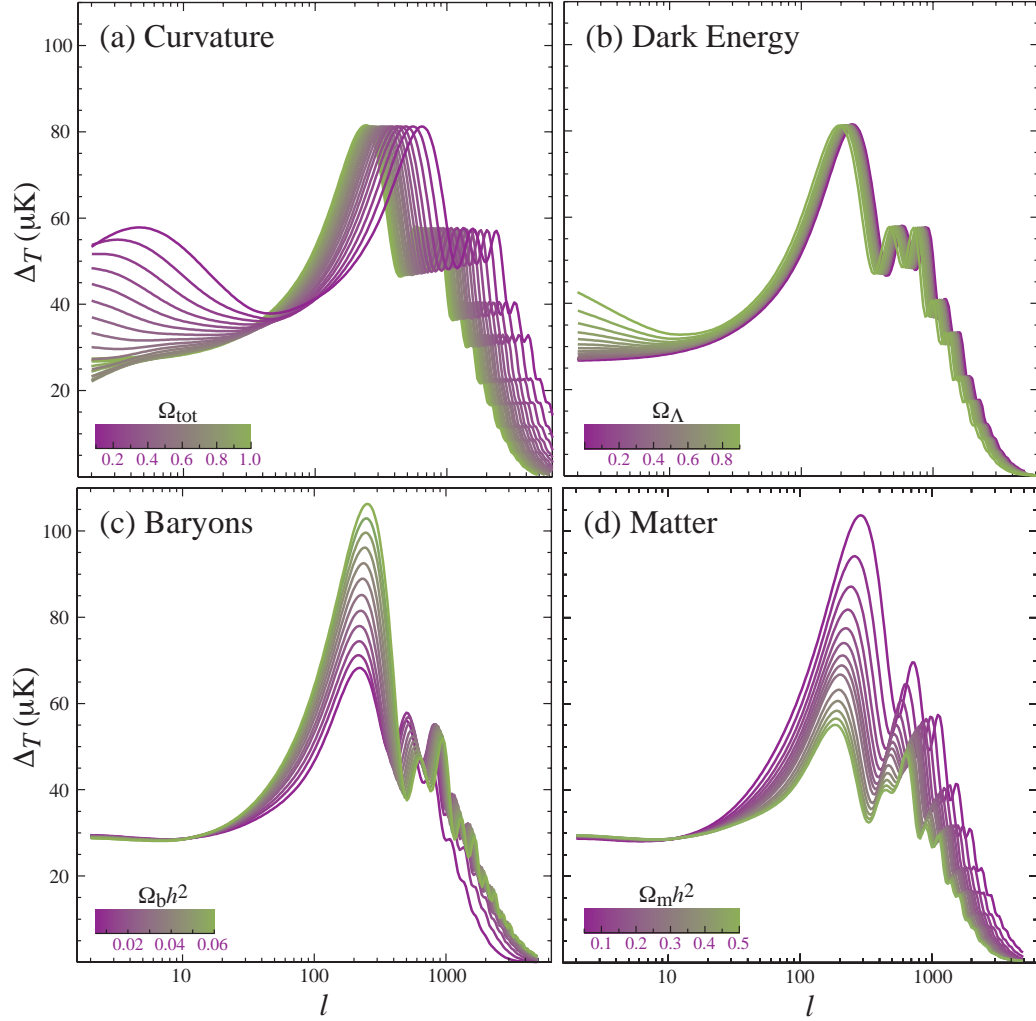
Figure 1.4: Sensitivity of CMB TT spectrum to four different parameters in the ΛCDM model: (a) curvature represented with Ω_{tot} (b) relative dark energy density Ω_{Λ} (c) physical baryon relative density $\Omega_{\text{b}}h^2$ (d) physical mass relative density Ω_{m}. This figure is taken from Ref. [3].

1.3 Dark Matter Models

To explain the need for dark matter in the observations mentioned in Section 1.2, different theories have been proposed. These theories can be divided into two categories: theories with non-particle dark matter and those with particle dark matter. This thesis will focus on particle dark matter, but let us first have a brief introduction on non-particle dark matter. Non-particle dark matter theories are mainly inspired by two ideas: modified Newtonian dynamics (MOND) and primordial black holes. MOND theories propose that the general relativistic dynamics is different on different scales. For a review of modified gravity and its implications in cosmology, see Ref. [24]. Primordial black holes are objects postulated to be formed in the early universe, under high density conditions. They did not go through stellar collapse, so they can be fairly light (in three mass windows: $10^{16}-10^{17}$g, $10^{20}-10^{24}$g, $10-10^3 M_\odot$ [25]). Primordial black holes are a candidate for dark matter because they are "dark" and non-baryonic. For a recent review of primordial black holes as dark matter, see Ref. [25].

Since particles are a key constituent of the standard model of particle physics, dark matter can also be perhaps particles. The known standard-model particles decoupled from the primordial thermal plasma as it was cooling. This process is called thermal production. Dark matter particles can be thermally produced or non-thermally produced, depending on whether they were supposed to be once in thermal equilibrium with the primordial plasma.

Axion is an example of non-thermally produced dark matter. The theory of axion started with the P-Q mechanism, which was proposed to solve the strong CP problem in quantum chromodynamics (QCD) by Peccei and Quinn in 1977 [26]. Later, axion was postulated to be a type of pseudo-Goldstone boson from the spontaneous breaking of P-Q symmetry by Weinberg and independently by Wilczek [27; 28]. This production mechanism of Axions is out of thermal equilibrium with the cosmological

thermal bath.

Popular thermally produced dark matter particles include weakly interacting massive particles (WIMPs), and self-interacting dark matter (SIDM). WIMP model is probably the most well-studied model in the past few decades due to the following apparent coincidence. Assuming that CDM is a thermal relic through the freeze-out process, the abundance of CDM today can be calculated by solving the Boltzmann equation [29]:

$$\Omega_{\chi 0} h^2 \approx 0.331 \frac{x_f}{\sqrt{g_*(m)}} \frac{2.57 \times 10^{-10} \text{GeV}^{-2}}{\langle \sigma v/c \rangle}, \tag{1.12}$$

where $x_f = \frac{mc^2}{k_B T_f} \approx 10$ labels the temperature at which freeze-out takes place, m is the mass of the dark matter particle, $\langle \sigma v/c \rangle$ is the thermal average annihilation cross section of dark matter particles χ, and $g_*(m) \approx 100$ is the effective numbers of relativistic degrees of freedom when $k_B T = mc^2$. If $\langle \sigma v/c \rangle$ takes the value of $G_F^2 \approx 10^{-10} \text{GeV}^{-2}$ then the current dark matter abundance is retained. This coincidence is called "WIMP miracle", meaning if dark matter particles interact weakly (in the sense of **weak interaction**), then the correct abundance is obtained.

In a simple WIMP model, WIMPs do not scatter off each other. They gather together to form structures called dark matter halos through gravitational interaction. Simulations of large scale structures show that the dark matter profiles inside the halos is the NFW profile [30]:

$$\rho(r) = \frac{\rho_0}{\frac{r}{R_s}(1 + \frac{r}{R_s})^2}, \tag{1.13}$$

where r is the distance from the halo center, ρ_0 is scale density, and R_s is scale radius. When measuring density near the halo center, $\rho(r) \propto r^{-1}$. This cuspy density profile is predicted by a number of simulations with collisionless dark matter particles. However, observations of rotation curves of dwarf galaxies and low surface brightness (LSB) galaxies [31; 32; 33; 34; 35; 36; 37; 38; 39; 40; 41; 42; 43] show that the dark matter density in these galaxies near the center is "cored", i.e. $\rho \propto r^0$. These dwarf

and LSB galaxies are supposed to be made mostly of dark matter. This problem is usually referred to as **core-cusp problem**. In small structures, there are even more problems with collisionless dark matter particles. For example, the number of observed satellite galaxies is smaller than predicted by simulations, which is dubbed **missing satellite problem**, and some observed dwarf galaxies are too dense to fail in forming stars, which is called **too big to fail problem**. To solve these problems, researchers introduce scatterings between dark matter particles into the model, and propose self-interacting dark matter (SIDM) models. The introduction of baryons into the dark matter simulations can also solve these problems, and can make it more complicated to distinguish between different dark matter models [44; 45]. In Chapter III we will discuss in more detail the particle physics model of SIDM, and the constraints on it. For a comprehensive review of SIDM and small structure problems, see Ref. [46].

1.4 Dark Matter Direct Detection

The evidence for dark matter mainly comes from its gravitational interactions. After the dark matter particle theories were proposed, experimental particle physicists started to think about detecting dark matter particles through other interactions. Ref. [47] proposed a method of detecting neutrinos through their scattering and deposit of energy onto nuclei in the target. Inspired by this idea, Ref. [48] suggested that the same idea could be used to detect certain dark matter particles. In this paper, the authors investigated three types of dark matter particle-nucleus interactions: 1. spin-independent (SI) interactions; 2. spin-dependent (SD) interactions; 3. strong interactions. This type of detection of dark matter particles through their scattering off the target is called **dark matter direct detection**. The first two categories of interactions in Ref. [48] are still studied in today's direct detection experiments. The first factor to consider when designing direct detection experiments

is the background noise. To avoid the disturbance from cosmic rays, the detector is usually placed deep underground. The noise from detector itself should also be reduced as much as possible, so low-background detectors and/or cryogenic targets are widely implemented. Two early results from low-background Ge detectors are published in 1987 and 1988 [49; 50]. The first series of direct detection experiments made use of kg-level solid state targets, including CDMS [51], EDELWEISS [52], and CRESST [53]. To increase the sensitivity of direct detection experiments, targets with larger mass are required. However, solid state targets scaled up to ton-level mass are hard to build. In the 1990s, the use of cryogenic noble liquid (especially liquid xenon) targets was proposed. In the 2010s, the results from XENON100 (with 100 kg xenon) [54], PandaX-II (with 500 kg of xenon) [55], LUX (with 250 kg of xenon) [56], DarkSide-50 (with 50 kg of argon) [57] and XENON1T (with 1 ton of xenon) [58] experiments which use liquid noble targets were released. In the 2020s, LZ (with 5.5 tons of xenon) [59], XENON-nT (with 5.9 tons of xenon) [60], PandaX-4T (with 3.7 tons of xenon) [61], ARGO (with 360 tons of argon) [62] and DARWIN (in the early stage of development) [63] experiments are/will be in operation and taking data.

The results of direct detection experiments can have two possible outcomes:

- The results are inconsistent with background, then the existence of dark matter particles is confirmed. This type of results hasn't occurred so far. There have been the controversial positive results from DAMA/LIBRA [64; 65], but their validity is still under debate. There are four more experiments—COSINE-100 [66], ANAIS [67], SABRE [68], and COSINUS [69] using the same NaI targets as those in DAMA/LIBRA under construction or taking data. These experiments aim to resolve the controversies about the DAMA/LIBRA results.

- The results are consistent with background. In this case, based on the sensitivity of the detector, the experiment could exclude certain regions in the scattering cross section-dark matter mass ($\sigma - m$) parameter plane. For every

15

dark matter mass m considered in the experiment, there is a threshold cross section $\sigma_{th}(m)$. If the cross section is above this threshold, then with the sensitivity of the detector, the scattering event should already have been discovered (with a certain level of statistical significance). The null result indicates that cross sections above $\sigma_{th}(m)$ are all excluded, so this curve $\sigma_{th}(m)$ in the $\sigma - m$ plane is called **exclusion limit**. With the increase in the sensitivity of direct detection experiments, the exclusion limit curve reaches a lower σ, meaning more and more areas in the parameter plane are excluded.

When the sensitivity of detectors is high enough, the scattering of neutrinos (mostly solar and atmospheric) off nuclei will be detected. Since the signals from coherent neutrino-nucleus scattering (CNNS) and dark matter particle scattering are the same in any detector, CNNS will lead to an irreducible background. This limit is called the neutrino floor. Fig. 1.5 (taken from Ref. [4]) shows the spin- independent exclusion limits from the direct detection experiments mentioned above, and the projected exclusion limits to achieve for the future experiments. The green region above the grey dashed curve is excluded by the current experiments. The orange curves show the neutrino floor from different types of detectors. We can see that DARWIN and ARGO will reach the neutrino floor for WIMP mass above 100 GeV. For comprehensive reviews of the concepts and current status of dark matter direct detection, see Ref. [70; 4].

In Chapter II, we will give a more detailed discussion on the calculations of event rates in dark matter direct detection, and then obtain exclusion limits from event rates. Specifically, we will discuss the effects of astrophysical parameters and their uncertainties from the simple halo model (SHM) on the exclusion limit of XENON1T experiment.
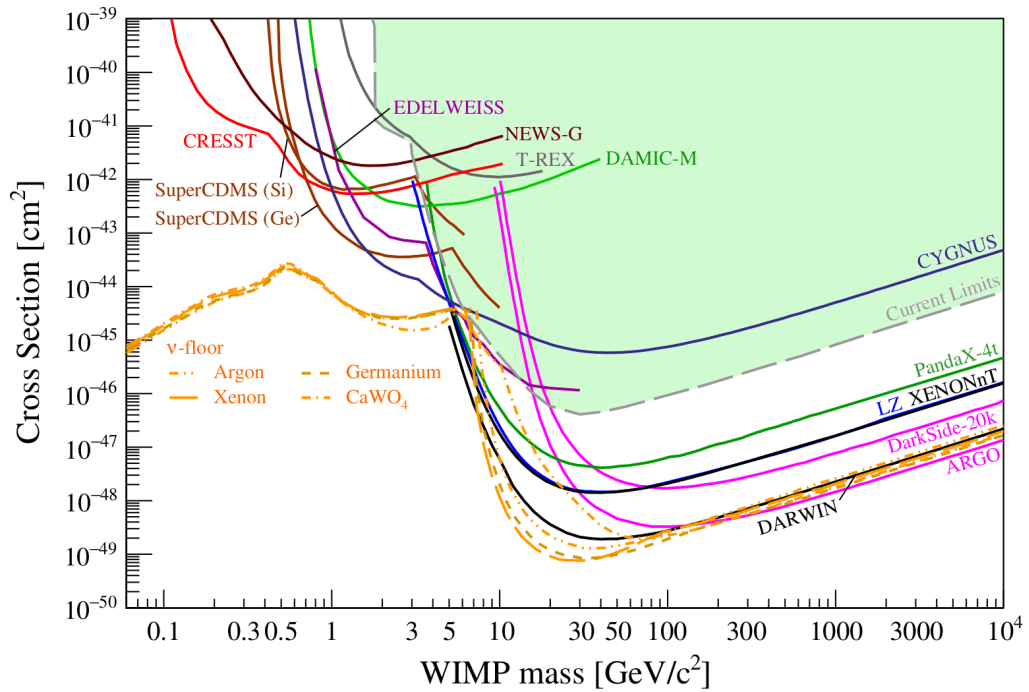
Figure 1.5: Exclusion limits for spin-independent scattering from some previous direct detection searches, and projected exclusion limits for future experiments. The grey dashed curve shows the current limit from conducted experiments. The orange curves show the neutrino floors for different types of detectors. This figure is taken from Ref. [4].

1.5 Dark Stars

A pair of WIMP particles are expected to annihilate into a pair of leptons: $\chi + \bar{\chi} \rightarrow l + \bar{l}$. This process keeps WIMPs in chemical equilibrium with the primordial bath before freeze-out. After freeze-out, WIMP pairs cannot meet each other any more, which means this process is rare in the scale of the universe. However, at the center of dark matter halos, the WIMP density is significantly higher than the average value throughout the universe, and this annihilation might still be frequent. The detection of WIMP annihilation products is an indirect way of dark matter detection. At $z = 10 - 50$, when the first stars were expected to form, the dark matter density at the center of star-forming mini-halos were even higher. The production rate of standard model particles from pair annihilation of WIMPs was also higher, probably high enough to be a source of power for the first stars. Ref. [71] investigated this possibility. In this paper, the authors started from a star-forming baryon density profile inside a 10^6 $M_\odot$ mini-halo from Ref. [72] and an NFW profile for WIMP, and calculated the density of WIMP after the adiabatic contraction. The energy producing rate from WIMP pair annihilation was then calculated to be:

$$Q_{ann} = \langle \sigma v \rangle \rho_\chi^2 / m_\chi. \tag{1.14}$$

The energy produced in this process was then argued to be trapped inside the baryonic gas, heat the protostellar gas up and compete with the cooling of this gas. For dark matter particle mass in the range of 1 GeV to 10 TeV, the dark matter heating was shown to dominate over cooling in the core's evolution. Therefore, stars powered by dark matter pair annihilation, or simply **Dark Stars**, are physically allowed to exist.

A series of follow up studies on Dark Stars powered by WIMP emerged after the idea was first proposed. Ref. [73] studied the stellar structure of WIMP Dark Stars. With the polytrope model of stellar structure, Dark Stars were shown to be made

mostly of ordinary matter, and more massive, cooler, larger, and more luminous than standard metal-free stars. Ref. [74] investigated the gas and dark matter profiles from several cosmological simulations, and showed that the heating from dark matter can overcome the cooling of the gas, in agreement with Ref. [71]. Ref. [75] showed that Dark Stars can grow in mass to become supermassive, which are bright enough to be detected by James Webb Space Telescope (JWST). The stellar evolution MESA code was applied to model dark stars in Ref. [76]. The results from MESA showed agreement with those in Ref. [73]. Ref. [77] further studied the stability of Dark Stars with MESA code, and found Dark Stars to be stable even for very massive ones up to $\approx 1000 \ M_\odot$. This work also looked at the pulsation of Dark Stars, and found the acoustic modes in them. See Ref. [78] for a comprehensive review of dark stars.

The previous research focuses mainly on Dark Stars powered by WIMP. However, simple WIMP models face challenges from small structure problems (see the end of Section 1.3), and SIDM is proposed to solve those problems. Is it possible to form Dark Stars with SIDM? Chapter III gives a systematic study on this question. In this Chapter, we will show that one SIDM model satisfy all of the three requirements for forming Dark Stars: 1. Avoid constraints from experiments; 2. The dark matter core is dense enough to produce heating that can dominate the gas cooling; 3. The energy produced can be trapped inside the gas cloud. We will also build a first stellar model for Dark Stars with SIDM, study their properties, and compare with Dark Stars powered by WIMP.

1.6 Galactic Archaeology

The ΛCDM model predicts that the structures in the universe form hierarchically, i.e. small structures form first and then aggregate together to form larger ones. The formation of the Milky Way galaxy also follows this process. The Milky Way galaxy grows through the accretion of satellite galaxies orbiting around it. Fig. 1.6 shows the
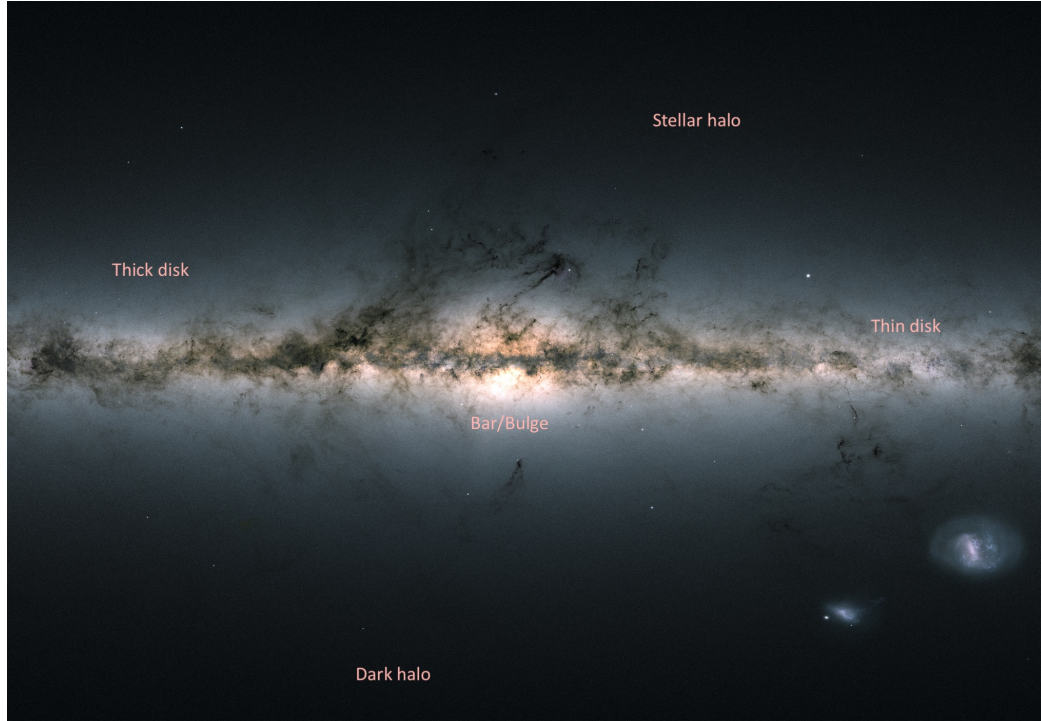
Figure 1.6: The components of the Milky Way galaxy. This photo is constructed based on the data from the second data release of *Gaia* mission [5]. This figure is taken from Ref. [6].

structure of the Milky Way galaxy and its hosting dark matter halo. The accreted stars are mostly located in the stellar halo. Meanwhile, the stars born in the thin disk of main galaxy can sometimes also be ejected into the thick disk and even into the stellar halo. The study on the birth place of stars and eventually the assembly history of galaxies is called galactic archaeology (For a review on galactic archaeology, see Ref. [6]). The knowledge of the assembly history of galaxies can help reveal the mass function of dark matter (sub)halos, which is a strong discriminator of dark matter models [79; 80; 81] (e.g., WIMP, SIDM, and Warm Dark Matter). Galactic archaeology is based on the fact that stars have memory of their origin. Low mass stars can live longer than the universe, so they are the fossil preserved today that can help us understand galaxy formation. There are three different messengers from low mass stars that we can use to understand the galaxy formation history: chemical abundances, stellar ages, and dynamical motion.

The chemical abundances in the atmosphere of stars can reflect the position and time of the formation of stars. One type of chemical elemental abundances used as "chemical tags" is the α-elements (O, Mg, Si, Ca, S, and Ti) accumulated in massive stars and released in Type-II supernovae explosions. The relative abundance of α- and iron peak elements, calculated by:

$$[\alpha/\text{Fe}] = \log \frac{c_\alpha}{c_{\text{Fe}}}, \tag{1.15}$$

is an indicator of the age of a star. The symbol c_e represents the concentration of element e in the atmosphere of the star (see Ref. [82] for a review). Another typical group is heavier elements which are beyond the iron peak produced in slow (s-) and rapid (r-) neutron capture processes. For reviews of these two types of chemical taggings, see Ref. [82] and [83].

Stellar ages can help us date the events that led to the formation of galaxies. Isochrones are curves in the Hertzsprung-Russell diagram representing stars of the same age but different masses. The stellar ages are usually measured by stellar isochrone fitting with photometry data. *Gaia* is a satellite launched by European Space Agency to measure the parallax, magnitude, and proper motion of a large number of stars. Bayesian inference tools using a combination of photometry, *Gaia* data and chemical abundances improve the stellar age measurement results [84; 85; 86]. Information about the internal structures of stars from astroseismology is also a promising tool to help produce more accurate age estimates [87; 88]. For more information on star age measurements, see Ref. [89] and references therein.

Finally, dynamics of stars can tell us about the merger history of a galaxy. The orbits of stars inside a galaxy can be characterized by integrals of motion, such as total energy, angular momentum, and actions J_r, J_z and J_ϕ for axialsymmetric potential [90]. After a substructure gets merged into the main galaxy, it gets disrupted by

the tidal force in the position space, yet the component stars continue to follow trajectories close to the original system. If the accreted substructures are small enough compared with the galaxy, then the stars in the substructure will be clustered in the integrals of motion space. If the gravitational potential of the main galaxy evolve slowly enough, then the integrals of motion will be conserved. Therefore, the stars from the merged substructures will stay clustered in the integrals of motion phase space for a long time, and may be found at $z = 0$ with clustering algorithms.

In Chapter IV we will discuss in detail how the actions J_r, J_z and J_ϕ are defined. The calculation of actions is relatively challenging, but it can be done using the AGAMA software [91] when the 3D position and 3D motion of stars are given, and the potential is axialsymmetric. We will also discuss how clustering analysis in action space can be used to find the mergers in cosmological baryonic zoom-in simulations of MW-mass galaxies from the FIRE project [92]. The groups found by clustering algorithm *Enlink* [93] will be compared with the actual mergers to show the validity of this method.

CHAPTER II

Astrophysical Uncertainties in Dark Matter Direct Detection

[1]

2.1 Introduction

While the evidence of gravitational interactions due to Dark Matter (DM) is well established at a wide variety of scales and epochs in the universe, observation of DM interactions with the Standard Model (SM) remains elusive. One of the most well-studied and theoretically well-motivated DM candidates is the Weakly Interacting Massive Particle (WIMP). Signatures of non-gravitational WIMP interactions can be searched for through missing energy searches at LHC, by looking for the SM byproducts of WIMP annihilation in the Universe, and in Direct Detection (DD) experiments.

Direct Detection experiments search for signatures of DM interactions with nuclei [48; 95]. A significant experimental program is underway to search for nuclear recoils arising from the elastic scattering of WIMPs in the local DM halo. DD experiments are instrumented with various technologies designed to detect recoils of nuclei

---

[1]This chapter is based on the paper [94] published in JCAP.

or electrons with kinetic energies as low as a few eV. In using experimental results to learn about dark matter properties, assumptions must be made about the local DM distribution. In this chapter, we discuss the effect of several large astrophysical uncertainties in the DM distribution on the limits which have been set on the spin-independent (SI) WIMP-nucleon cross section.

Results from direct detection experiments are often analyzed assuming a simple isothermal distribution of dark matter, the Standard Halo Model (SHM). Although the SHM has been shown to be in tension with both cosmological simulations of galaxy formation and observations of baryonic matter in dwarf galaxies within the local group, the SHM is a reasonable first approximation for the calculation of the expected flux of DM particles at direct detection experiments [96; 97; 98]. The effects of variations in astrophysical parameters on the sensitivity of DD experiments, both within the context of and assuming various deviations from the SHM, have been investigated (for example, see [99; 100; 101; 102; 103; 104; 105; 106; 107]). Previous work demonstrates that variations in the escape velocity and circular velocity of dark matter could yield a shift to exclusion limits at smaller WIMP masses in DD experiments (for example, see [100]). Interesting recent work [108] argues for the existence of local tidal debris which would modify the local distribution. These results rely on the argument that low metallicity stars serve as a proxy for dark matter, an idea that is still a matter of debate, as discussed in, for example, [109]. [109] also suggests a refinement to SHM to include the Gaia sausage, updates values of some astrophysical parameters in SHM, and then calculates the effects of these changes on the limits set by DD experiments. In the current chapter, we restrict our studies to the SHM, as this is the primary distribution used by DD experiments for the interpretation of their data, and investigate the effect on dark matter exclusion limits of uncertainties in the astrophysical parameters used to define the SHM .

We focus on the effects of three astrophysical parameters and their uncertainties

on dark matter DD studies: the local escape velocity, the local circular velocity of the solar system around the galaxy and the local dark matter density. A variety of local and global observations of the Milky Way suggest a wide range of possible values for the local DM density, ρ_χ [110; 111; 112; 113; 114; 115; 116; 117; 118; 119; 120; 121; 122; 123]. Although the recoil rate at DD experiments is simply $\propto$ ρ_χ, the uncertainty in the sensitivity of such experiments due to other astrophysical parameters is exacerbated by the possibly large variations in the local DM density. Especially at low WIMP masses, $m_\chi \lesssim 15\text{GeV}$, nuclear recoils with enough kinetic energy to be detected above threshold at DD experiments must be induced by WIMPs at the high velocity tail of the local phase space distribution. Thus, uncertainties both in the shape of the local velocity distribution, characterized by the local circular velocity, and in the local escape velocity can significantly impact the sensitivity of DD experiments to low mass WIMPs.

In this chapter, we investigate the impact of astrophysical uncertainties on the sensitivity of current DD experiments. Specifically, we use DDCalc software [124] to perform a likelihood analysis of the sensitivity of XENON1T [7] to low mass WIMPs while sampling values of the relevant astrophysical parameters from the latest observational data. For the local escape velocity, we compare the sensitivity of DD experiments using the results of the RAVE survey [8] and a recent analysis of *Gaia*-DR2 [125]. We show that, for very low WIMP masses which would only produce recoils near the threshold of DD experiments, the sensitivity can vary by several orders of magnitude in the WIMP-nucleon cross section assuming either measurement of the escape velocity. Thus, a more precise determination of the escape velocity from data could significantly reduce the astrophysical uncertainties in DD experiments. Also, we find that the astrophysical uncertainties in the XENON1T exclusion limits are similar when assuming either the results of the RAVE survey or the more recent determination of the escape velocity based on *Gaia* data.

This chapter is structured as follows: in Section 2.2 we discuss the relevant astrophysical parameters and their uncertainties, in Section 2.3 we present the results of the likelihood analyses and in Section 2.4 we discuss our conclusions.

2.2 Astrophysical Parameters

The differential recoil rate for the elastic scattering of target nuclei in DD experiments (per unit target mass) can be written as a function of the momentum transfer between the WIMP and the nucleus q, and WIMP velocity v, in the lab frame

$$\frac{dR}{dE_R} = 2\frac{\rho_\chi}{m_\chi} \int d^3v \, v f(\mathbf{v}) \frac{d\sigma}{dq^2}(q^2, v) \, , \tag{2.1}$$

where the differential SI WIMP-nucleus scattering cross-section is given by

$$\begin{aligned}
\frac{d\sigma}{dq^2}(q^2, v) &= \frac{[Zf_p + (A-Z)f_n]^2}{\pi v^2} F^2(q)\Theta(q_{\max} - q) \\
&\approx \frac{1}{4\mu_p^2 v^2} A^2 \sigma_{\mathrm{SI}} F^2(q)\Theta(q_{\max} - q) \, ,
\end{aligned} \tag{2.2}$$

with Z as the atomic number, A the atomic mass, f_p the dark matter coupling to protons, f_n the dark matter coupling to neutrons, and F the nuclear form factor. The form factor accounts for the fact that as the energy of the dark matter particle increases, it will eventually only elastically scatter off individual nucleons rather than coherently scattering off the nucleus. We have assumed isospin conserving couplings (i.e. $f_p \simeq f_n$) in the second equivalence to write the recoil rate in terms of the SI WIMP-nucleon cross section, σ_{SI}, and the reduced mass of the WIMP-nucleon system, μ_p. Also, note that, for the small momentum transfers typical of low mass WIMPs scattering off nuclei, the nuclear form factor $F^2(q) \approx 1$.

The Heaviside step function in Eq. 2.2, $\Theta(q_{\max} - q)$, which arises from the maximal momentum transfer allowed by the elastic scattering kinematics, can be exchanged

for a minimum velocity imposed on the phase space integral in Eq. 2.1, which we can rewrite as

$$\frac{dR}{dE_R} = \frac{\rho_\chi}{m_\chi} \frac{A^2}{2\mu_p^2} \sigma_{\mathrm{SI}} \int\limits_{v > v_{\mathrm{min}}} d^3v \, \frac{f(\mathbf{v})}{v} \, , \qquad (2.3)$$

where $v_{\mathrm{min}} = \sqrt{ME_R/2\mu^2}$ for a target nucleus of mass M with the reduced mass of the WIMP-nucleus system μ. We assume the WIMP velocity distribution is given by a truncated Maxwell-Boltzmann distribution of the form

$$f(\mathbf{v}) = \frac{1}{N_{\mathrm{esc}} \, (\pi v_0^2)^{3/2}} \exp\left(-\frac{|\mathbf{v} + \mathbf{v}_E|^2}{v_0^2}\right) \Theta(v_{\mathrm{esc}} - |\mathbf{v} + \mathbf{v}_E|) \, , \qquad (2.4)$$

where $\mathbf{v}_E$ is the velocity of the Earth relative to the galactic rest frame, v_0 is the local circular velocity and v_{esc} is the local escape velocity. The normalization of the velocity distribution is given by

$$N_{\mathrm{esc}} = \mathrm{erf}\left(\frac{v_{\mathrm{esc}}}{v_0}\right) - \frac{2}{\sqrt{\pi}} \frac{v_{\mathrm{esc}}}{v_0} \exp\left(-\frac{v_{\mathrm{esc}}^2}{v_0^2}\right) \, . \qquad (2.5)$$

In a self-consistent model of the Milky Way, the astrophysical parameters ρ_χ, v_0 and v_{esc} will not be independent [102; 103; 107; 126]. However, given both the variation between different observations and the large uncertainties of individual measurements, for simplicity we ignore correlations between astrophysical parameters in the SHM.

We note that, for low mass WIMPs such that $m_\chi \ll M$, we have $v_{\mathrm{min}} \simeq \sqrt{ME_R/2m_\chi^2}$. Thus, for a fixed nuclear recoil energy E_R, the minimum kinematically allowed WIMP velocity will increase for smaller WIMP masses. Also, the mean inverse speed, given by the integral over the velocity distribution in Eq. 2.3, becomes increasingly dependent on the value of v_{esc} as m_χ decreases. While the value for v_{esc} in Eq. 2.4 determines the lower threshold for sensitivity to WIMPs with smaller m_χ at a given experiment, the sensitivity to WIMPs with masses slightly above this threshold will

also be determined by the shape of the velocity distribution, characterized by the local circular velocity v_0. In contrast, $v_{\min}$ is low enough for high mass WIMPs that the sensitivity of DD experiments is only slightly dependent on the shape and cut-off of the velocity distribution.

2.2.1 Local Dark Matter Density

In DD experiments, the most commonly used values for the local dark matter density are either $\rho_\chi = 0.3\,\mathrm{GeV/cm^3}$ or $\rho_\chi = 0.4\,\mathrm{GeV/cm^3}$, while a considerably wider range of measured values is possible. Recent measurements suggest the local dark matter density should lie in the range of $(0.2 - 0.6)\,\mathrm{GeV/cm^3}$ as discussed in Refs. [103; 127]. The relative errors of individual measurements of the local dark matter density are dominated by systematics and are typically $\approx 30\%$ of the central value, as suggested by [109]. In our work, we present the effects of variation in the local dark matter density on the sensitivity of DD experiments in two ways. First we sample a uniform distribution of ρ_χ between $(0.2 - 0.6)\,\mathrm{GeV/cm^3}$. As the individual error bars of each of the measurements of the dark matter density do not overlap for the most part, we sample a uniform distribution over the most likely range of the density. Secondly, since the sensitivity of a given DD experiment has a simple linear scaling with ρ_χ, we also wanted to independently analyze the effects of the uncertainty in the velocity distribution by choosing four discrete values of ρ_χ : $(0.3,\ 0.4,\ 0.5,\ 0.6)\,\mathrm{GeV/cm^3}$.

Finally, to check the impact of uncertainties from individual measurements of the dark matter density, we also sample a Gaussian distribution with central value $0.3\,\mathrm{GeV/cm^3}$ and standard deviation $0.09\,\mathrm{GeV/cm^3}$ (30% of the central value). Assuming the Gaussian distributions for the local circular and escape velocities decribed below, we find that the sets of exclusion curves in the case of a Gaussian dark matter density distribution are essentially the same as exclusion limits in the case of the

uniform distribution described above. The reason for this similarity is straightforward given the linear relationship between the exclusion limits and the dark matter density; the values of the dark matter density falling within $\sim 1\sigma$ of the central value corresponds to a range which resembles a uniform distribution of $(0.2-0.4)\,\mathrm{GeV/cm^3}$. Below we will therefore present results only for the two cases of uniform density distribution between $(0.2-0.6)\,\mathrm{GeV/cm^3}$ and the four discrete values listed in the previous paragraph.

2.2.2 Local Circular Velocity

For the value for the local circular velocity of the Sun around the center of galaxy we will use $v_0 = 220\,\mathrm{km/s}$ [103]. The largest uncertainty for the value of v_0 among recent measurements arises from the orbit of the GD-1 stellar stream, which has a value of 18 km/s or about 8.1% of the central value. Since the error bar for v_0 in this case is symmetric about the central value, we assume v_0 will follow a normal distribution with central value $v_0 = 220\,\mathrm{km/s}$ and dispersion $18\,\mathrm{km/s}$. We note that more precise determinations of the local circular velocity with central values of $\sim 230\,\mathrm{km/s}$ have recently been reported in Refs. [128; 129], while similarly high values of the local circular velocity can be inferred from the proper motion of Sgr A* [130] with recent estimates of the solar radius (for example, see [131; 132]). Although assuming a central value of $v_0 = 230\,\mathrm{km/s}$ can have a small impact on our results near the low WIMP mass threshold for DD experiments, the differences between the most probable values of the exclusion curves are negligible compared to uncertainty bands, which span at least one order of magnitude in the SI WIMP-nucleon cross section at low WIMP masses. In addition, assuming a more precise measurment of the circular velocity with an uncertainty closer to 1% of the central value causes the widths of the uncertainty bands to shrink by an $\mathcal{O}(1)$ factor which depends on m_χ and the other astrophysical parameters.

2.2.3 Local Escape Velocity

We compare the results of DD experiments using two measurements of the local escape velocity: the latest result $v_{esc} = 580 \pm 63\,\text{km/s}$ from the DR2 of the *Gaia* survey [125] (referred to as Monari *et al.* escape velocity) and an older (commonly used) value $v_{esc} = 533^{+54}_{-41}\,\text{km/s}$ [8] from the RAVE survey (referred to as RAVE escape velocity). The errors of these two measurements are about 10% of the central values. In the Monari *et al.* result, the error bar is symmetric about central value, so for v_{esc} we again assume it will follow a normal distribution. In the RAVE result, the uncertainties are asymmetric and, thus, applying a method suggested by [133], the escape velocity from RAVE survey can be assumed to follow a probability distribution given by

$$
f(v_{esc}) = \frac{1}{N} \exp\left(-\frac{1}{2} \left[\frac{\ln\left(1 + \frac{v_{esc} - v_{0esc}}{\gamma}\right)}{\ln \beta} \right]^2 \right),
\tag{2.6}
$$

where $v_{0esc} = 533\,\text{km/s}$ is the central value, $\gamma = \frac{\sigma_+ \sigma_-}{\sigma_+ - \sigma_-}$, $\beta = \frac{\sigma_+}{\sigma_-}$, $\sigma_+ = 54\,\text{km/s}$, $\sigma_- = 41\,\text{km/s}$, and N is the normalization factor. Note that in this choice for the distribution function, the probability that $v_{esc} \leq 362\,\text{km/s}$ is zero. However, $v_{esc} = 362\,\text{km/s}$ is significantly less than the central value of $v_{0esc} = 533\,\text{km/s}$, so this assumption of distribution function does not affect our results. One of the main purposes of this work is to determine how the different measurements of the escape velocity impact the exclusion limits of DD experiments. We note that a recent determination of the local escape velocity, which also uses the most recent *Gaia* data but does not assume the velcoity distribution of halo stars is isotropic, gives a value of $v_{esc} = 528^{+24}_{-25}\,\text{km/s}$ [134]. Although the central value given in [134] is more consistent with the RAVE escape velocity, we will demonstrate that even the larger central value of the Monari *et al.* escape velocity does not broadly change the effects

of astrophysical uncertainties on the senstivity of DD experiments.

2.3   Results

We have performed Monte Carlo simulations of the generated exclusion curves for XENON1T experiment based on their 2017 analysis [7]. At a given dark matter mass, we draw 10^5 points from the previously described distributions of the three astrophysical parameters and calculated the associated exclusion limits on the SI WIMP-nucleon scattering cross section using the DDCalc software [124]. The most probable value at a given WIMP mass is located at the peak of the histogram of the generated exclusion limits. In the following sections, the 2σ region around the respective peaks of the histograms for each WIMP mass is also referred to as the uncertainty band. We note that, due to the loss of detector efficiency and correspondingly high WIMP velocities required for low mass WIMPs to induce nuclear recoils above threshold, DDCalc only calculates limits based on the XENON1T analysis for WIMP masses $m_\chi \geq 3.9\,\text{GeV}$. Since the sensitivity of DD experiments to elastic scattering induced by higher mass WIMPs only trivially depends on ρ_χ, we also require $m_\chi \leq 15\,\text{GeV}$ in our analysis.

An example histogram is shown using the Monari escape velocity for a 4 GeV WIMP in Fig. 2.1 with the 1σ region shaded light grey and the 2σ region shaded dark grey, while the black shaded region lies outside of the 2σ uncertainty band. We find that the distribution of limits on the SI WIMP-nucleon scattering cross section has a very long tail extending towards the higher/weaker cross section limits. The long tail corresponds to the smaller values of v_{esc}, where the sensitivity of an experiment is highly dependent on the escape velocity. In this region of parameter space with a small WIMP mass and small value for the escape velocity, there is a very strong suppression of the number of expected events above the experimental threshold for the SHM. Thus, a modest change in v_{esc} can lead to an orders of magnitude variation in the exclusion limit. Because the relative uncertainties of the Monari and RAVE
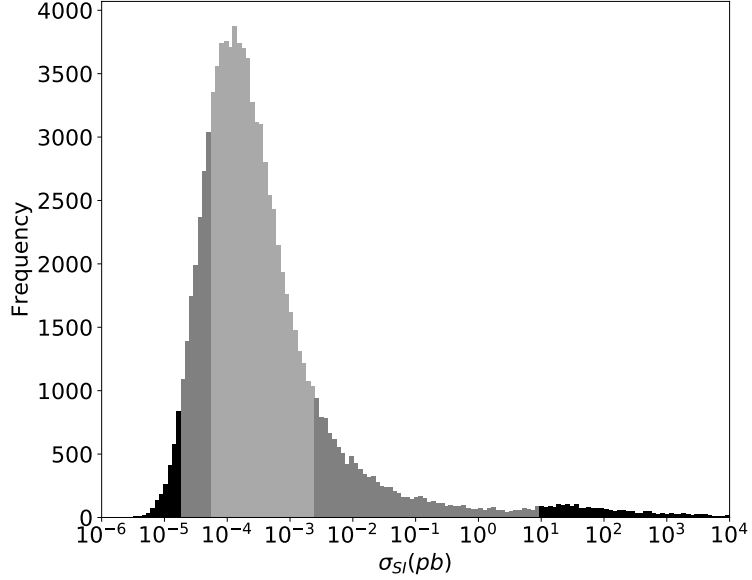
Figure 2.1: A histogram of 10^5 exclusion limits on SI WIMP-nucleon scattering cross section set by the XENON1T experiment [7] for $m_\chi = 4\,\mathrm{GeV}$ and sampling over three astrophysical parameters: the local dark matter density ρ_χ which is assumed to be a uniform distribution between 0.2 and 0.6 GeV/cm^3, while the other two parameters are Gaussian distributed with local escape velocity $v_{esc} = 580 \pm 63$ km/s (the Monari result) and local circular velocity $v_0 = 220 \pm 18$ km/s. The 1σ and 2σ regions are shaded light and dark grey, respectively, on the histogram, while the black shaded region lies outside of the 2σ uncertainty band. The corresponding histogram for the RAVE [8] escape velocity (not shown) looks very similar with small shift to weaker cross section limits. The uncertainty in the cross section limit at low WIMP masses is dominated by the escape velocity, causing the very long tail towards weaker limits due to the very strong suppression of the number of expected recoil events above threshold in a DD experiment.
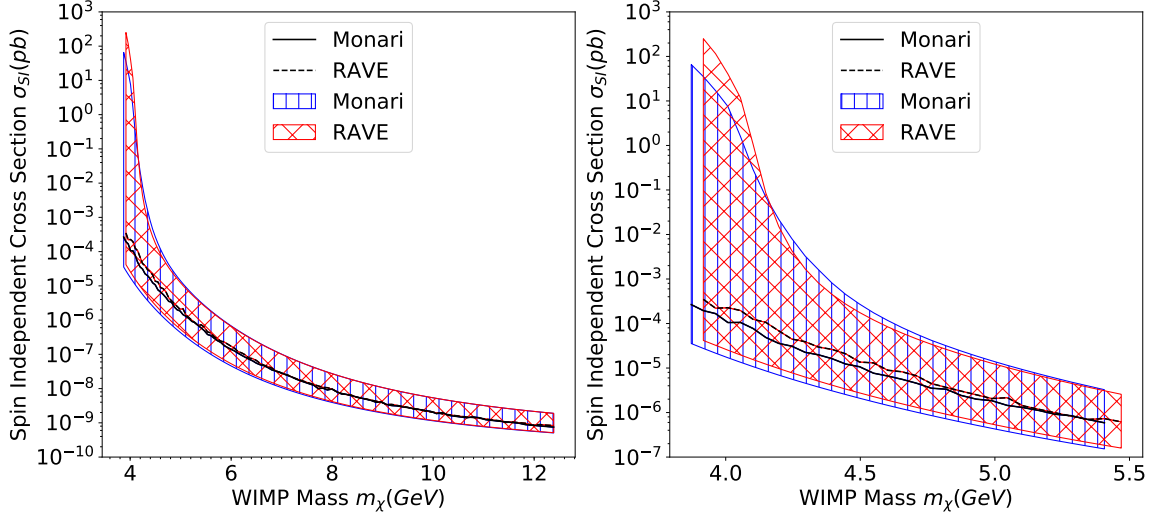
Figure 2.2: The most probable value of the exclusion curve from the XENON1T experiment [7] for the SI WIMP-nucleon cross section along with the corresponding 2σ ranges (hatched regions) using the Monari and RAVE escape velocities. A uniform distribution for ρ_χ between 0.2 and 0.6 GeV/cm^3 is sampled while v_0 and v_{esc} are distributed as described in the text. Left panel: exclusion curves in the range of WIMP masses 3.9–15 GeV. Right panel: exclusion curves zoomed in to WIMP masses below 6 GeV.

escape velocity measurements are similar and the central value of the RAVE result is lower than the central value in Monari $et\,al.$, the lower end of the RAVE v_{esc} distribution reaches smaller velocities. Thus, one would expect not only a weakening of the most probable limits at low WIMP masses assuming the RAVE escape velocity, but also a slightly longer tail in the distribution of exclusion limits at higher cross sections.

2.3.1   Sampling Three Parameters

In this subsection, we present the results of our Monte Carlo simulation of 10^5 points drawn from a uniform distribution for ρ_χ between $(0.2-0.6)\,\mathrm{GeV/cm^3}$ as well as the previously described distributions for the local escape velocity and the local circular velocity. In Fig. 2.2, the most probable values as well as the 2σ regions of exclusion curves for both the Monari escape velocity and the RAVE escape velocity

are plotted based on the analysis of XENON1T data. Very little difference is found in the most probable exclusion curves assuming either the Monari or RAVE distributions for the escape velocity. Even when the WIMP mass is below 6 GeV where the difference is the greatest, the two curves are very similar and any deviations remain well within the 2σ ranges. As expected, the Monari *et al.* most probable exclusion curve is slightly below the RAVE most probable exclusion curve because the Monari escape velocity has a larger central value for v_{esc} than the RAVE result. The sensitivity of DD experiments to low mass WIMPs increases with larger escape velocities because the higher WIMP velocities induce nuclear recoils with energies sufficiently above the experimental threshold. Similarly, the smaller escape velocities from the RAVE distribution explains why the 2σ range extends to higher cross sections at low WIMP masses.

2.3.2 Sampling Two Parameters

In this subsection, we fix the local dark matter density to four discrete values in the range $(0.2 - 0.6)\,\mathrm{GeV/cm^3}$ and draw 10^5 Monte Carlo samples from the distributions for v_0 and v_{esc}. The purpose of this sampling strategy is to determine the effects of the new, larger central value of the escape velocity from the *Gaia* data independently of variations in the dark matter density.

We show the most probable exclusion curves as well as the uncertainty bands corresponding to a fixed value of $\rho_\chi = 0.3\,\mathrm{GeV/cm^3}$ in Fig. 2.3. We find the uncertainty bands shrink quickly as the WIMP mass increases, from about 6 orders of magnitude at 4 GeV to a factor of ~1.6 at 15 GeV. In the previous subsection, in which ρ_χ is uniformly distributed, the width of uncertainty bands becomes approximately constant at a factor of ~3 as the WIMP mass approaches 15 GeV. From this comparison, we can conclude that the uncertainty of the exclusion curve at WIMP masses greater than 6 GeV mainly comes from the uncertainty in local dark matter density. A more
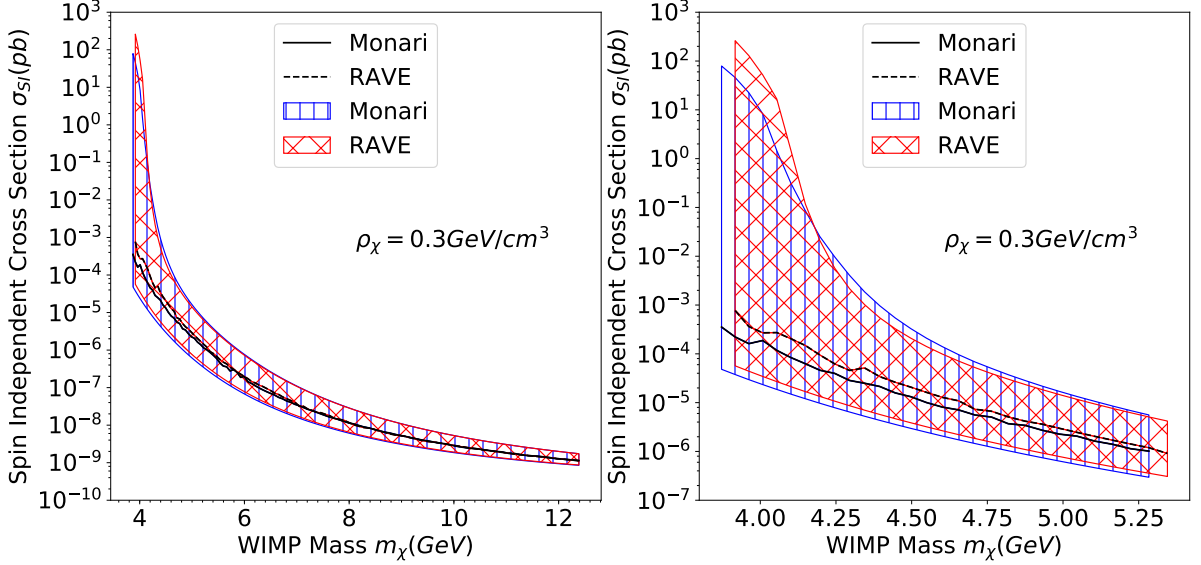
Figure 2.3: The most probable value of the exclusion curve from the XENON1T experiment [7] for the SI WIMP-nucleon cross section along with the corresponding 2σ ranges (hatched regions) using the Monari and RAVE escape velocities. Here ρ_χ is taken to be $0.3\,\text{GeV/cm}^3$ Left panel: exclusion curves in the range of WIMP masses 3.9–15 GeV. Right panel: exclusion curves zoomed in to WIMP masses below 6 GeV. Above WIMP mass 6 GeV, comparison to Fig. 2.2 indicates the uncertainty from local dark matter density begins to dominate; below 6 GeV, the uncertainty from escape velocity dominates.

accurate estimate of ρ_χ could significantly reduce the width of the uncertainty bands on the corresponding exclusion curves. We also notice the consistency of the most probable exclusion curves for Monari $et\,al.$ and RAVE when either scanning over or fixing the dark matter density. This consistency reflects the independence of exclusion limits for WIMPs with masses above 6 GeV from uncertainties in the best fit values of the escape velocity.

At lower WIMP masses, however, a difference between the most probable exclusion curves for Monari $et\,al.$ and RAVE can be observed, as displayed in Fig. 2.3. Comparing Fig. 2.2 and Fig. 2.3, we can see the differences between the most probable exclusion curves for limits calculated using the Monari $et\,al.$ and RAVE data found in Fig. 2.3 are similar to differences between the most probable exclusion curves when

scanning over the uncertainty in local dark matter density in Fig. 2.2. Even though the most probable exclusion curves can differ significantly at low WIMP masses, the uncertainty bands using the Monari *et al.* and RAVE data broadly overlap regardless of whether the dark matter density is fixed or not. Thus, more precise measurements of the escape velocity could significantly reduce the astrophysical uncertainties associated with the sensitivity of DD experiments to low mass WIMPs.

We also performed Monte Carlo simulations of additional fixed values of the dark matter mass extending up to 0.6 GeV/cm^3. In each of these cases, the overall shapes of the curves remained approximately constant. The main change is the curves are scaled vertically to lower/stronger values of the SI WIMP-nucleon cross section limit at all WIMP masses by the ratio of the dark matter density to 0.3 GeV/cm^3. As the nuclear recoil spectrum is directly proportional to ρ_χ, this is the expected scaling of cross section limits with the local dark matter density.

2.4 Conclusions

In this work we have examined the effects of astrophysical uncertainties on the exclusion limits set by XENON1T [7]. While this work was originally motivated by the new value for the escape velocity measured using *Gaia* data [125], we expanded our analysis to include the uncertainties on the local dark matter density and speed of the Sun's orbit around the galactic center. We utilized the DDCalc software [124] to perform the likelihood analyses. To our knowledge, this is the first work that uses DDCalc to quantify these effects specifically for the standard halo model. As this is the model that is canonically assumed in the production of all direct detection exclusion limits, understanding the impact of the astrophysical uncertainties of this model on these limits is important. These uncertainties are typically neglected when collaborations present their final limits.

Several general features emerge from our analysis. Above a WIMP mass of 6 GeV,

the uncertainty of the limits on the SI WIMP-nucleon cross section is dominated by the local dark matter density. The 2σ range for the exclusion limit when sampling a uniform distribution of ρ_χ approaches a factor of $\sim$3 as the WIMP mass increases to 15 GeV and a more accurate estimate on ρ_χ is thus the most important parameter to reduce the effect of astrophysical uncertainties in this mass range. At smaller WIMP masses, where the uncertainty of the escape velocity begins to dominate, we have demonstrated that the associated uncertainty band is $\sim$6 orders of magnitude wide in the cross section near a WIMP mass of 4 GeV. This band is highly asymmetric extending to larger cross sections (weaker limits) as the WIMP mass decreases. The experimental sensitivity is a very strong function of v_{esc} as the WIMP mass decreases, leading to much weaker exclusion limits for fairly modest decreases in the escape velocity.

The astrophysical uncertainties calculated in this work are larger than the statistical fluctuations in the background presented in the XENON1T cross section limits at low WIMP masses. For example, the 2σ band of the expected limit from the statistical fluctuations in the background at $m_\chi = 7\,\text{GeV}$ is less than a factor of $\sim$3 in the XENON1T analysis. By contrast, when we assume a fixed ρ_χ while allowing v_0 and v_{esc} to vary given their respective uncertainties in Fig. 2.3, the astrophysical uncertainties yield more than a factor of $\sim$6 variation in the exclusion limit on the SI WIMP-nucleon scattering cross section for $m_\chi = 7\,\text{GeV}$. If properly incoperated into the XENON1T likelihood analysis, astrophysical uncertainties in the signal can weaken exclusion limits on the SI WIMP-nucleon scattering cross section at low WIMP masses while the statistical fluctuations in the background should remain roughly constant. The effects of astrophysical uncertainties are important to consider when comparing limits generated by xenon-based experiments to experiments focused on detecting low mass dark matter. Targets in low mass dark matter searches are often composed of lighter nuclei and the experiments typically have lower nuclear re-

coil energy thresholds. Although the astrophysical uncertainties from the local escape velocity will still eventually dominate the uncertainty, results from direct detection experiments with lighter target nuclei and lower thresholds should be more robust at lighter WIMP masses.

Additionally, we find that the updated best fit value for the escape velocity based on *Gaia* data does not have a large effect on the astrophysical uncertainties related to the XENON1T limit. In particular, the differences between the most probable exclusion limits for the different measurements of the escape velocities are well within the 2σ uncertainty ranges for the astrophysical uncertainties.

Dark Stars with Self-Interacting Dark Matter

1

3.1 Introduction

The first stars are thought to have formed inside $(10^6$–$10^8)\,M_\odot$ dark matter halos at redshifts $z \sim 20$ when the Universe was about 200 million years old [72; 136; 10]. In the standard picture, the process begins with hydrogen clouds collapsing to $10^{-3}\,M_\odot$ protostellar objects at the center of the halo. The protostar grows further by accretion, and hydrogen fusion turns on providing the stellar heat source for the stars. The accretion process stops once they grow to $\sim 100\,M_\odot$ due to the outward pressure of the hot ionizing photons leaving the stars. However, this standard picture could change if an additional heat source is present, such as dark matter annihilation. In this case, the collapse process could be halted due to dark matter heating, resulting in drastically different objects known as Dark Stars [71; 137; 138].

Dark Stars are composed almost entirely of ordinary matter (mostly hydrogen) and can be very luminous. The name "Dark Star" refers to their power source being dark matter annihilation rather than nuclear fusion for ordinary stars [71; 137; 138; 139; 140; 73; 74; 76; 78; 77]. The products from dark matter annihilation can be

---

[1]This chapter is based on the paper [135] published in PRD.

trapped inside the hydrogen cloud where they heat up the baryonic gas, leading to the formation of a star in hydrostatic equilibrium. The dark matter power is spread out uniformly throughout the star that is too cool and diffuse to ignite nuclear fusion.

Previous studies [71; 137; 138; 139; 140; 73; 74; 76; 78; 77] have focused on Dark Stars powered by Weakly Interacting Massive Particle (WIMP) dark matter. Dark Stars could form for a wide range of WIMP masses and annihilation cross sections. These stars could grow extremely massive and luminous. Their radii are typically $10\,\mathrm{AU}$ and their surface temperatures $10^4\,\mathrm{K}$. They form with a mass of $1\,M_\odot$, but could continue to accrete surrounding matter and become as massive as $10^7\,M_\odot$ with luminosities as large as $10^{10}\,L_\odot$ [76], potentially making Dark Stars detectable with the James Webb Space Telescope [75]. Once the dark matter power runs out, these stars could collapse to black holes at high redshifts, thereby providing seeds for supermassive black holes in the early Universe [75; 141].

In this work, we investigate the possibility of Dark Stars forming within the self-interacting dark matter (SIDM) scenario; see Ref. [46] for a review on SIDM. Dark matter self-interactions can transport heat and thermalize the inner halo [142; 143; 144; 145; 146]. Taking into account the effects of baryons, SIDM predicts more diverse dark matter distributions in galaxies than collisionless dark matter such as WIMPs [147; 148; 149; 150] – it has been shown that SIDM can explain the full range of the observed diversity of rotation curves of spiral galaxies [151; 152; 153], a long standing challenge in astrophysics, see Refs. [154; 155; 156] and references therein as well as Ref. [157] for a recent review. The preferred self-interaction cross section per dark matter particle mass to address this *diversity problem* (as well as a host of other potential "small-scale" problems, see Refs. [158; 79; 159] for reviews) is $\sigma_{\mathrm{SI}}/m_{\mathrm{DM}} \gtrsim 1\,\mathrm{cm^2/g}$ in galaxies, while the cross section is constrained to be $\sigma_{\mathrm{SI}}/m_{\mathrm{DM}} \lesssim 0.1\,\mathrm{cm^2/g}$ in galaxy clusters [146; 160]. Thus, astrophysical observations require a velocity dependent self-interaction cross section, which can be realized in many particle physics

models [46].

In order for a Dark Star to form, dark matter annihilation must start heating the hydrogen cloud faster than it cools due to the various baryonic cooling processes at some point during the collapse of the hydrogen cloud [71]. When this happens, the dark matter power will slow down the contraction of the hydrogen cloud and a Dark Star is formed once the system has reached hydrostatic equilibrium. Two conditions must be met for dark matter heating to overcome the baryonic cooling processes: First, the heating rate from dark matter pair annihilation is proportional to the square of the dark matter density; in order for dark matter to be a sufficiently strong power source, its density in the collapsing hydrogen cloud must be sufficiently high. Second, the dark matter annihilation products must deposit their energy into the hydrogen cloud rather than escape the center of the halo or heat the remaining dark matter.

The purpose of this paper is to show that both of these necessary conditions for the formation of Dark Stars can be met in the SIDM scenario. Let us begin by discussing the first of these conditions. For collisionless dark matter such as WIMPs, the dark matter in the center of the halo follows a cuspy density profile, and the WIMP density increases further in the presence of a deepening baryonic potential as can be modeled by adiabatic contraction [161]. The resulting annihilation rate is high enough for heating from dark matter annihilation to overcome the cooling processes of the collapsing hydrogen cloud. The SIDM scenario must rely on a different mechanism to achieve a high enough dark matter density to power Dark Stars. SIDM-only simulations show that dark matter self-interactions generally lead to a shallow density core in the center of halos [143; 144], in contrast to a density cusp in the WIMP case. In addition, the usual formalism of adiabatic contraction [161; 162; 163; 164; 165; 166] applies to collisionless dark matter only; SIDM, by definition, has efficient self-interactions.

A recent study [9] used a conducting fluid model [167] and showed that if baryons dominate the gravitational potential, their presence can speed up the onset of gravothermal collapse ("catastrophe") of an SIDM halo [167], leading to a cuspy profile with a high central density [168; 169; 170; 171; 172; 173; 174]; see also Refs. [147; 148; 149; 9; 150]. Hydrodynamical simulations of the formation of protogalaxies that host the first stars have shown that baryons indeed dominate the central potential in these systems [10]. Taking into account the baryonic influence on the gravothermal evolution of the SIDM halo, we will show that the central dark matter density in such protogalaxies could reach and exceed the values required for the formation of a Dark Star.

Let us return to the second condition, i.e. that the dark matter annihilation products must heat the baryonic gas. In the WIMP scenario, dark matter annihilates into standard model particles. In the dense protostellar baryon cloud, all electromagnetically-charged annihilation products thermalize quickly with the baryons and hence the power from dark matter annihilation is effectively transferred into the hydrogen gas. In typical SIDM model, dark matter annihilates almost exclusively into non-standard-model particles. Nonetheless, efficient heating of the baryonic gas by dark matter annihilations is achieved if the primary annihilation products decay into electromagnetically-charged standard model particles before they leave the dense baryonic cloud where a Dark Star might form and before they interact with the remaining dark matter.

We will consider a simple but concrete SIDM model by introducing a fermionic dark matter candidate and a light scalar particle [175; 176]. The scalar couples to both the dark matter candidate and the standard model fermions. While the dark matter particles will annihilate predominantly into the light scalars, this new scalar can have short enough decay lengths into standard model particles for SIDM annihilation to heat the protostellar hydrogen cloud. We will systematically study

astrophysical constraints on this model and show that it can simultaneously achieve the observed dark matter density, the favored self-interacting cross section in galaxies, and evade direct and indirect detection constraints. The dark matter annihilation cross section in this model has interesting velocity dependence due to the interplay of p-wave suppression and Sommerfeld enhancement. This velocity dependence allows us to simultaneously achieve the observed relic density via canonical thermal freeze-out, large values of the annihilation cross section in the center of the $\sim 10^7 \, M_\odot$ minihalos where Dark Stars could form, and suppressed annihilation cross sections at recombination allowing the model to evade stringent bounds from cosmic microwave background (CMB) observations.

The determination of the properties of Dark Stars in the SIDM scenario such as their luminosity, surface temperature, or size requires dedicated dynamical simulations of the gravitationally coupled evolution of the hydrogen and the SIDM distributions while simultaneously computing baryonic cooling rates and the effects of dark matter self-interactions and annihilation on both distributions. As a first step towards the study of the properties of Dark Stars in the SIDM scenario, we discuss the Lane-Emden equations describing a Dark Star once it has reached hydrostatic equilibrium. We solve these equations for the simplifying assumptions that the self-interactions in the Dark Star are fast enough to thermalize the SIDM such that the dark matter is described by an isothermal distribution. Without the aforementioned dedicated simulations, we do not know the dark matter density in the Dark Star; instead, we parameterize our solutions in terms of the SIDM-to-baryon mass ratio in the Dark Star. Our results suggest that the properties of Dark Stars in the SIDM scenario are similar to those in the WIMP scenario, although SIDM-powered Dark Stars might be slightly larger and cooler than WIMP-powered ones.

The remainder of the paper is organized as follows: In Sec. 3.2, we introduce the SIDM model and study the viable parameter space. In Sec. 3.3, we investigate the

possibility of achieving a sufficiently high dark matter density for powering a Dark Star via gravothermal evolution of the SIDM. In Sec. 3.4, we describe how to gain a first glimpse on the properties of SIDM powered Dark Stars under the assumptions described above and present numerical results. We summarize and conclude in Sec. 3.5. Throughout this work we use natural units with $\hbar = c = 1$.

3.2 Particle Physics Model of SIDM

We consider an SIDM model extending the standard model by a gauge-singlet Dirac fermion χ which plays the role of the dark matter candidate and a gauge-singlet real scalar ϕ which mediates dark matter self-interactions as well as interactions between χ and standard model particles. In order to realize the velocity dependence of the dark matter self-interactions required to explain observations from dwarf galaxies to galaxy clusters [146; 160], i.e. strong dark matter self-interactions at galactic scales and weaker self-interactions at the galaxy cluster scale, we will consider a mediator much lighter than the dark matter candidate, i.e. $m_\phi \ll m_\chi$. If such a light mediator couples not only to the dark matter but also to standard model particles, strong constraints arise from direct and indirect detection experiments as well as from observations of the CMB [177; 178; 179; 176; 180; 181; 182; 183; 184; 185]. As we will discuss in this section, the model we consider can simultaneously give rise to the observed dark matter relic density via thermal freeze-out, satisfy bounds from direct and indirect detection as well as the CMB, and, crucial for the possibility of a Dark Star, the energy from dark matter annihilation can be deposited in the baryonic gas in the environments where a Dark Star might form. The interplay of p-wave suppression and Sommerfeld enhancement due to the light mediator gives rise to an interesting velocity dependence of the dark matter annihilation cross section, which plays an important role in satisfying these requirements simultaneously.

We assume that the couplings of ϕ to dark matter particles χ and standard model

fermions f take the form

$$\mathcal{L} \supset -y_\chi \overline{\chi}\chi\phi - y_f \sum_f \frac{\sqrt{2}m_f}{\langle V \rangle} i\overline{f}\gamma^5 f\phi \,, \tag{3.1}$$

where y_χ (y_f) are dimensionless couplings between χ (f) and ϕ, and we chose the couplings of ϕ to standard model fermions to be proportional to their standard model Yukawa couplings $\sqrt{2}m_f/\langle V \rangle$ with the mass of the fermion m_f and the vacuum expectation value of the standard model Higgs boson $\langle V \rangle = 246\,\text{GeV}$. Throughout this work, we assume dark matter self-interactions to be much stronger than interactions of χ with the standard model, i.e. we take $y_f \ll y_\chi$. The coupling structure in Eq. (3.1) is maximally CP-violating: ϕ couples to χ like a CP-even scalar, but to standard model fermions like a CP-odd pseudo-scalar. Such a structure can, for example, be realized in a two Higgs doublet model extension of the standard model [176]. This coupling structure has various important phenomenological consequences. The dominant annihilation channel in this model is $\overline{\chi}\chi \to 2\phi$. For the CP-even $\overline{\chi}\chi\phi$ coupling, this process is p-wave suppressed such that the model can avoid constraints from indirect detection experiments and on the energy injection into the standard model bath in the early Universe while producing the observed dark matter relic density via thermal freeze-out. The CP-odd $\overline{f}\gamma^5 f\phi$ coupling leads to velocity suppressed spin-independent direct detection cross sections [186; 187; 188], hence direct detection constraints are mitigated.

Let us discuss in some more detail the velocity dependence of the $\overline{\chi}\chi \to 2\phi$ annihilation cross section arising from the interplay of p-wave suppression and Sommerfeld enhancement. At tree level and in the nonrelativistic limit, the annihilation cross section is

$$(\sigma v) = \frac{3\alpha_\chi^2 v^2}{4m_\chi^2}\sqrt{1 - \frac{m_\phi^2}{m_\chi^2}} \,, \tag{3.2}$$

where $\alpha_\chi \equiv y_\chi^2/4\pi$ and v is the relative velocity of dark matter particles. In the limit

$m_\phi \ll m_\chi$, the annihilation cross section receives non-perturbative corrections due to the effects of Sommerfeld enhancement,

$$(\sigma v)_{\text{eff}} = S_p \times (\sigma v) , \tag{3.3}$$

with

$$
\begin{aligned}
S_p &= \frac{(c-1)^2 + 4\,(ac)^2}{1 + 4\,(ac)^2} S_s , \\
S_s &= \frac{\pi \sinh(2\pi ac)}{a\left\{\cosh(2\pi ac) - \cos\left[2\pi\sqrt{c - (ac)^2}\right]\right\}} ,
\end{aligned}
\tag{3.4}
$$

where $a = v/2\alpha_\chi$ and $c = 6\alpha_\chi m_\chi/(\pi^2 m_\phi)$ [189; 175]. Thermal freeze-out (FO) occurs at $v \sim 0.1$, and the observed relic density is obtained for $(\sigma v)_{\text{eff}}^{\text{FO}} \simeq 6 \times 10^{-26}\,\text{cm}^3/\text{s}$. In the remainder of this work, we set the coupling y_χ to the value required to obtain the observed relic density via thermal freeze-out.

To illustrate the velocity dependence of $(\sigma v)_{\text{eff}}$ arising from the interplay between p-wave suppression and Sommerfeld enhancement, we plot $(\sigma v)_{\text{eff}}/(\sigma v)_{\text{eff}}^{\text{FO}}$ against the relative velocity v for different choices of m_χ and m_ϕ in Fig. 3.1. There are three overall regimes: For $v \gtrsim 0.1$, the Sommerfeld enhancement is negligible and the p-wave suppression leads to $(\sigma v)_{\text{eff}} \propto v^2$. For velocities below $v \sim 0.1$, the enhancement becomes effective and the annihilation cross section scales as $(\sigma v)_{\text{eff}} \propto 1/v$. However, for $v \lesssim m_\phi/m_\chi$, the Sommerfeld enhancement saturates and one recovers the usual p-wave scaling $(\sigma v)_{\text{eff}} \propto v^2$. In Fig. 3.1, we also indicate velocity regions relevant for different phenomenological aspects with the vertical gray bands. Thermal freeze out occurs at velocities $v \sim 0.1$–1, as indicated by the band labeled "relic density"; recall that throughout this work, we set the coupling y_χ to the value required to obtain the observed relic density.

In environments where Dark Stars form, dark matter has velocities of order

$v \sim 10^{-3}$–10^{-4} as indicated by the band labeled "Dark Stars". As we can see from Fig. 3.1, due to the effects of Sommerfeld enhancement, the effective annihilation cross section at these temperatures can be *larger* than at freeze-out. If the Sommerfeld enhancement saturates at velocities $v \lesssim 10^{-3}$, which occurs for $m_\phi/m_\chi \lesssim 10^{-3}$, Sommerfeld enhancement is stronger than the *p*-wave suppression at the velocities relevant for the Dark Star, see the different cases shown in Fig. 3.1.

In addition, in the model we consider, dark matter annihilates into light scalars which ultimately decay into electromagnetically charged standard model particles. Observations of the CMB yield strong constraints on energy injection into the standard model bath at recombination times; for dark matter annihilation into electromagnetically charged standard model states this sets an upper limit of $\langle \sigma v \rangle_{\mathrm{eff}}^{\mathrm{CMB}} \lesssim 10^{-25}\,\mathrm{cm}^3/\mathrm{s} \times (m_\chi/100\,\mathrm{GeV})$ [190; 191; 192].[2]

The characteristic velocity of dark matter during the recombination epoch depends on the kinetic decoupling temperature T_{kd} of dark matter. For the model we consider, the elastic scattering processes $\chi f \to \chi f$ and $\chi \phi \to \chi \phi$ are present below the freeze-out temperature $T_{\mathrm{FO}} \sim m_\chi/20$. Elastic scattering processes of dark matter with standard model fermions are suppressed by the small standard model Yukawa couplings as well as our assumption of $y_f \ll y_\chi$, hence, $\chi \phi \to \chi \phi$ is the dominant process in setting T_{kd}. In fact, the elastic scatterings between χ and ϕ particles keep dark matter in thermal equilibrium until the mediator becomes nonrelativistic [195], setting the scale for the kinetic decoupling of dark matter to $T_{\mathrm{kd}} \sim m_\phi$. The corresponding values for T_{kd} are generally slightly smaller than what is obtained in the WIMP scenario, and a later kinetic decoupling is a general feature of SIDM models (see e.g. Refs. [196; 197; 198; 199; 200]).

The temperature at which kinetic decoupling occurs has an impact on the dark matter velocity v at recombination. As long as the dark matter is in thermal equilib-

---

[2]The future CMB-S4 observations [193] will improve the sensitivity on the annihilation cross section by a factor of 3 [194].

rium, the dark matter velocity scales as $v \propto \sqrt{T}$ with the temperature of the standard model plasma T. However, after kinetic decoupling, i.e. for $T \lesssim T_{\text{kd}}$, the dark matter velocity scales as $v \propto T$. Hence, the lower T_{kd}, the higher the value for v at recombination. We are mainly interested in mediator masses in the range $m_\phi \sim 1$–100 MeV. For $m_\chi = 100$ GeV, this corresponds to dark matter velocities of $v \sim 10^{-9}$–10^{-10} at recombination as indicated by the band labeled "CMB" in Fig. 3.1. As long as the Sommerfeld enhancement of the annihilation cross section saturates at velocities $v \gg 10^{-9}$, corresponding to $m_\phi/m_\chi \gg 10^{-9}$, the effective dark matter annihilation cross section during recombination is much smaller than during freeze-out and the CMB bounds are satisfied.[3] Another early Universe constraint on the model arises from energy injection during big bang nucleosynthesis (BBN), which we will discuss later in this section.

For the bounds on the coupling y_f between ϕ and standard model fermions, the most stringent constraints stem from flavor physics measurements, in particular, constraints on charged kaon decays of the type $K^+ \to \pi^+ + \text{invisible}$ [202; 176], yielding

$$y_f \leq \begin{cases} 8 \times 10^{-5}, & \text{for } m_\phi \leq 100 \, \text{MeV}, \\ 2 \times 10^{-3}, & \text{for } 100 \, \text{MeV} \leq m_\phi \leq 1 \, \text{GeV}. \end{cases} \tag{3.5}$$

With the upper bounds on y_f in Eq. (3.5), we check if the energy from dark matter annihilation can be deposited in the baryonic gas in the environments where a Dark Star might form. As mentioned above, in our model dark matter annihilates predominantly into a pair of the new (light) scalars, $\overline{\chi}\chi \to 2\phi$. However, ϕ is not stable but decays into standard model particles – if such decays happen before the ϕ's leave the dense hydrogen cloud and before the ϕ's interact with dark matter

---

[3]The Sommerfeld enhancement features well-known resonances for fine-tuned combinations of the coupling y_χ and the ratio m_ϕ/m_χ [201], see Eq. (3.4). If the parameters of the models match the resonance condition, relevant bounds from the CMB can arise even for mass ratios as large as $m_\phi/m_\chi \sim 10^{-4}$–$10^{-5}$. However, as these bounds arise only for extremely fine-tuned combinations of y_χ and m_ϕ/m_χ, we will neglect them in this work.
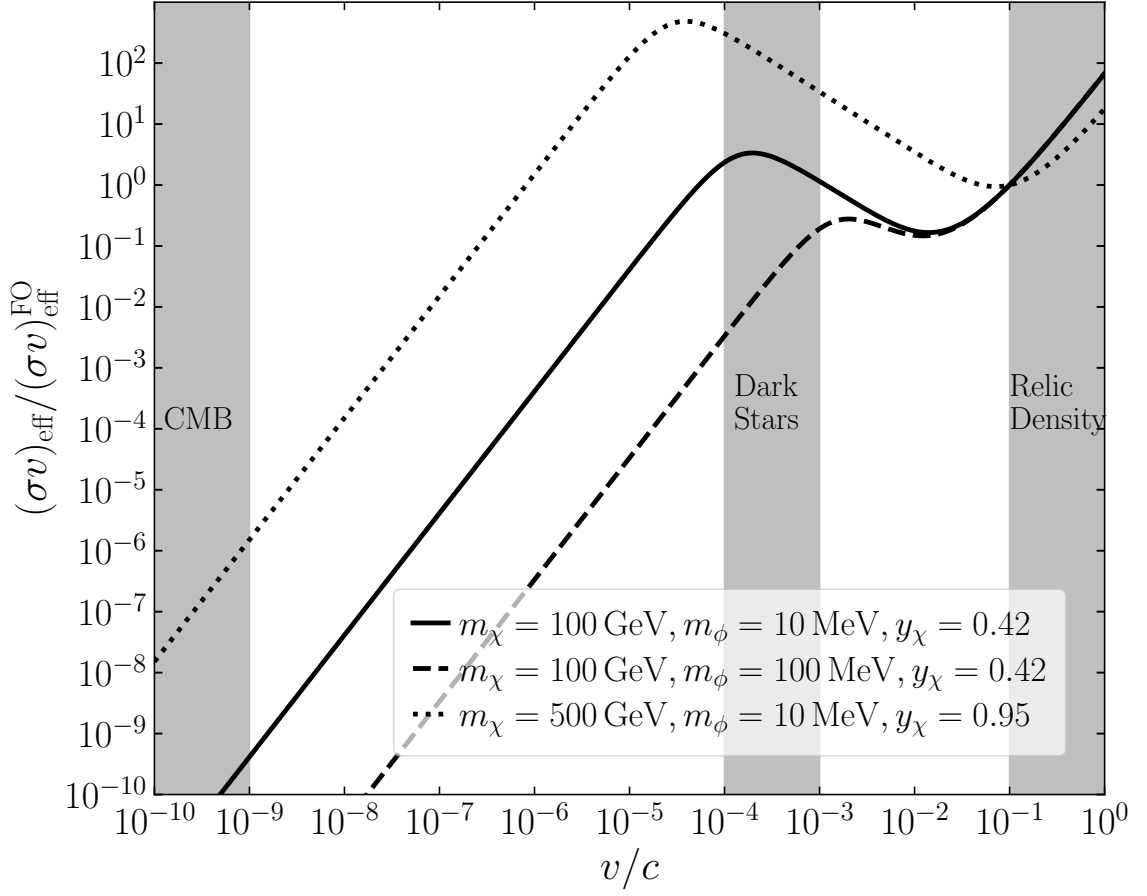
Figure 3.1: Velocity dependence of the annihilation cross section $(\sigma v)_{\text{eff}}$, normalized to $(\sigma v)_{\text{eff}}^{\text{FO}} = 6 \times 10^{-26} \, \text{cm}^3/\text{s}$, for different choices of m_χ and m_ϕ. The shaded areas show characteristic velocities during the recombination epoch relevant for CMB constraints, in Dark Stars, and at freeze-out relevant for setting the relic density.

particles, dark matter annihilation can still heat the baryons and power a Dark Star. For $m_\phi < 2m_e \approx 1\,\mathrm{MeV}$, all decays of ϕ into pairs of electromagnetically charged standard model fermions are forbidden. The dominant decay mode then becomes the loop-suppressed $\phi \to \gamma\gamma$, with typical decay lengths much longer than the size of a Dark Star. For $m_\phi \gtrsim 1\,\mathrm{MeV}$, on the other hand, decays into pairs of charged standard model states are allowed, and the associated decay length can be sufficiently small. We will be most interested in the mass range $1\,\mathrm{MeV} \lesssim m_\phi \lesssim 100\,\mathrm{MeV}$, where the dominant decay mode will be into a pair of electrons.[4] The associated decay width is

$$\Gamma(\phi \to e^+ e^-) = \frac{y_f^2}{4\pi} \frac{m_e^2}{\langle V \rangle^2} m_\phi \sqrt{1 - \frac{4m_e^2}{m_\phi^2}}, \tag{3.6}$$

and the corresponding decay length is

$$\lambda_{\mathrm{decay}} = \frac{\gamma}{\Gamma_{\phi \to e^+ e^-}} \tag{3.7}$$

$$\sim 1\,\mathrm{AU} \left(\frac{8 \times 10^{-5}}{y_f} \right)^2 \left(\frac{10\,\mathrm{MeV}}{m_\phi} \right)^2 \left(\frac{m_\chi}{100\,\mathrm{GeV}} \right),$$

where $\gamma \sim m_\chi / m_\phi$ accounts for the relativistic boost of ϕ's from $\overline{\chi}\chi \to 2\phi$ annihilation, and $y_f = 8 \times 10^{-5}$ is the largest value allowed by the flavor physics constraints for $m_\phi \lesssim 100\,\mathrm{MeV}$, see Eq. (3.5). The most important competing process is the scattering off dark matter particles, $\phi\chi \to \phi\chi$. If such scattering occurs before the ϕ's decays, the energy from dark matter annihilation will heat the dark matter rather than the baryons. The corresponding scattering cross section is $\sigma_{\phi\chi \to \phi\chi} \sim y_\chi^4 / 24\pi s$, where s is the center-of-mass energy. The mean free path for ϕ's from $\overline{\chi}\chi \to 2\phi$ annihilation scattering off dark matter particles is

$$\lambda_{\mathrm{scattering}} \sim \frac{1}{n_\chi \sigma_{\phi\chi \to \phi\chi}} \sim 10^{11}\,\mathrm{AU} \left(\frac{10^{12}\,\mathrm{cm}^{-3}}{n_\chi} \right), \tag{3.8}$$

---

[4]For larger m_ϕ, additional decay channels are relevant, e.g. into muons or pions, leading to even shorted decay lengths.

where n_χ is the dark matter number density with typical values of the order of $n_\chi \sim 10^{12} \, \mathrm{cm}^{-3}$ in a Dark Star as we will see below, we have set $m_\chi = 100 \, \mathrm{GeV}$, and fixed the coupling y_χ to yield the observed dark matter relic density. Comparing Eqs. (3.8) and (3.7) we see that ϕ's from dark matter annihilation decay into electrons much faster than they scatter off dark matter particles. For comparison to the decay length, a WIMP Dark Star is typically a few AU [76] in radius and, as we will discuss in Sec. 3.4, SIDM Dark Star could have similar or even larger sizes. Hence, requiring $\lambda_{\mathrm{decay}} < 1 \, \mathrm{AU}$, as we will do in the following, is a conservative criterion for the ϕ's resulting from dark matter annihilation to decay into electromagnetically charged standard model particles before they leave the baryon cloud or scatter off dark matter, ensuring that SIDM annihilation could power a Dark Star.

Another important constraint on the mediator lifetime arises from BBN. As the temperature becomes lower than the mediator mass, ϕ becomes nonrelativistic. The energy injection from ϕ decays could change the abundance of the light elements predicted in the standard scenario. We use Eq. 3.6 to estimate the ϕ lifetime as

$$\tau_\phi \approx 0.03 \, \mathrm{s} \left(\frac{8 \times 10^{-5}}{y_f} \right)^2 \left(\frac{10 \, \mathrm{MeV}}{m_\phi} \right) \ . \tag{3.9}$$

If the mediator decays before weak decoupling, $\tau_\phi \lesssim 1 \, \mathrm{s}$, we are assured that the light element abundances will not be modified.[5] As we can see from Eq. (3.9), this condition is easily satisfied in our model.

Last but not least, we comment on indirect detection constraints. As discussed above, the dominant dark matter annihilation mode is $\chi \bar{\chi} \to 2\phi$. In the parameter region we are interested in for Dark Stars, the ϕ's decay into pairs of electrons with decay length $\lambda_{\mathrm{decay}} \lesssim 1 \, \mathrm{AU}$, such that for the purposes of indirect detection, the relevant annihilation mode is $\chi \bar{\chi} \to \phi\phi \to e^+ e^- e^+ e^-$. The strongest constraints on this annihi-

---

[5]See Refs. [203; 204] for dedicated discussion of BBN constraints on models of this type, showing that $\tau_\phi \lesssim 1 \, \mathrm{s}$ is a conservative criterion.
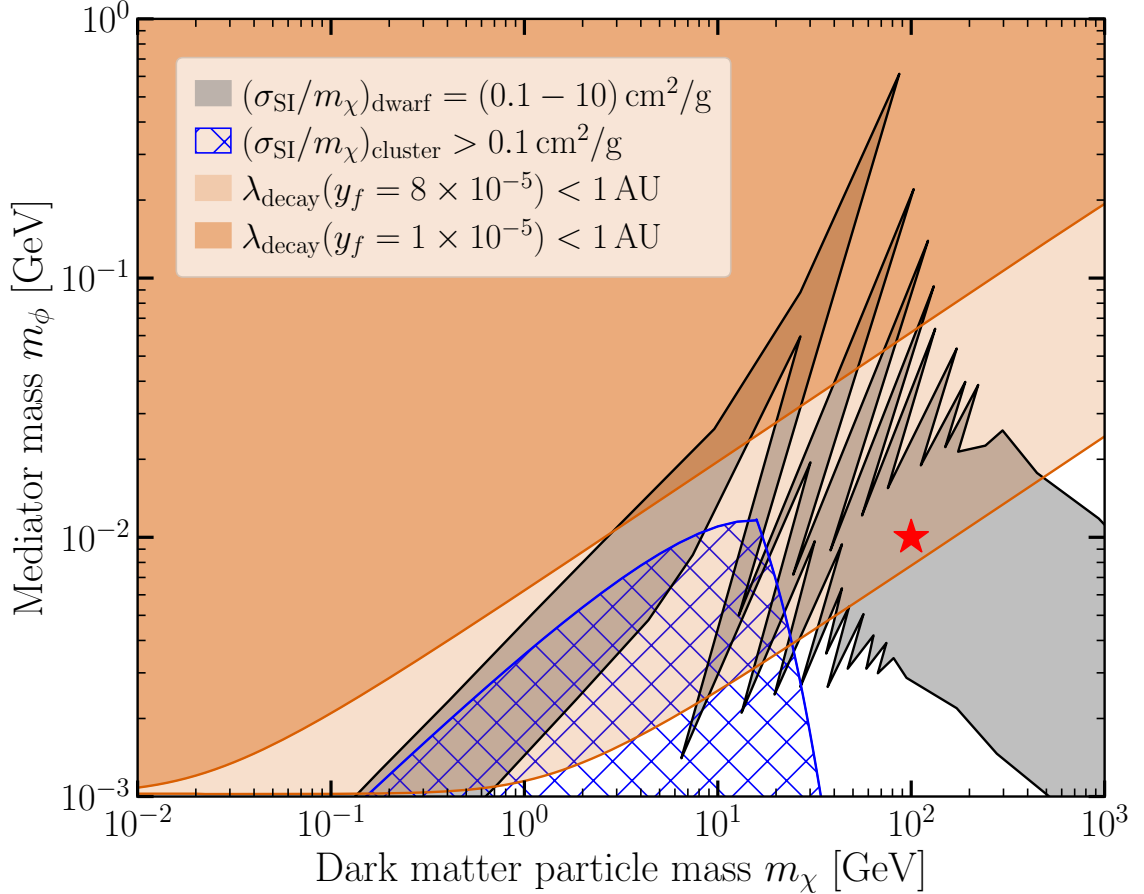
Figure 3.2: Different constraints on our model in the m_ϕ–m_χ plane as summarized in the final paragraph of section 3.2. In the gray-shaded band dark matter self-interactions at dwarf galaxy scales could alleviate the small-scale problems of collisionless dark matter. The blue hatched area is disfavored, in this region of parameter space dark matter self-interactions at galaxy-cluster scales lead to conflicts with observations. In the orange-shaded regions (the different orange shades are for different values of the coupling to standard model fermions as indicated in the legend), the decay length of the ϕ's from $\overline{\chi}\chi \to 2\phi$ annihilation are shorter than 1 AU such that dark matter annihilation could power a Dark Star. The red star marks the benchmark point we will use in the remainder of this work.

lation channel in the dark matter mass range we are interested in arise from gamma rays produced in final state radiation of the electrons and positrons. As shown in Fig. 3.1, the interplay of the p-wave suppression and the Sommerfeld enhancement can lead to rather large effective annihilation cross sections, $(\sigma v)_{\text{eff}} \sim 10^{-25}$–$10^{-24}\,\text{cm}^3/\text{s}$, at the velocities relevant to indirect detection from the satellite galaxies of the Milky Way, $v \sim 10^{-4}$. Nonetheless, current indirect detection constraints do not exclude such cross section for $m_\chi \gtrsim 10\,\text{GeV}$, see e.g. Refs. [205; 206; 207; 208], even before taking into account that these constraints assume cuspy dark matter profiles rather than the cored profiles one would expect for SIDM. At the galactic center of the Milky Way where $v \sim 10^{-3}$, the electrons and positrons from the $\chi\bar{\chi}$ annihilation could scatter with starlight and produce gamma-ray signals; searches for such gamma-rays are sensitive to cross sections close to those giving rise to the observed relic density via freeze-out production [209]. This constraint can be weakened if starlight and dark matter densities at the center are smaller than assumed in Ref. [209]. The benchmark case with $m_\chi = 100\,\text{GeV}$ and $m_\phi = 10\,\text{MeV}$ we are going to use satisfies these constraints.

In Fig. 3.2 we summarize the constraints on the parameter space discussed above. Recall that as a function of the dark matter mass m_χ, we fix the coupling constant y_χ to obtain the observed dark matter relic abundance. The gray-shaded band (taken from Ref. [176]) shows the region of parameter space where the dark matter self-interaction cross section is in the range $\sigma_{\text{SI}}/m_\chi = 0.1$–$10\,\text{cm}^2/\text{g}$ in dwarf halos (where $v \approx 5 \times 10^{-4}$), such that dark matter self-interactions can address the various small-scale problems of collisionless dark matter. In the blue hatched region, dark matter self-interaction at velocities corresponding to those in galaxy clusters are $\sigma_{\text{SI}}/m_\chi \gtrsim 0.1\,\text{cm}^2/\text{g}$; this region of parameter space is excluded by observations of galaxy clusters [146; 160]. As discussed above, there are no relevant constraints in the region of parameter space shown in Fig. 3.2 arising from direct detection or CMB

constraints. In the orange-shaded regions in Fig. 3.2, the decay length of ϕ's from $\overline{\chi}\chi \to 2\phi$ annihilation is shorter than $1\,\mathrm{AU}$, such that SIDM annihilation could power a Dark Star. The different shades of orange in Fig. 3.2 correspond to different values of the coupling of ϕ to standard model fermions, note that both values of y_f chosen in Fig. 3.2 are allowed by the flavor physics constraints discussed above. Considering all of these constraints, Fig. 3.2 demonstrates that there is a viable region of parameter space where our model exhibits the desired dark matter phenomenology, experimental and observational bounds are satisfied, and the energy from dark matter annihilation can be deposited in the baryonic gas in the environments where a Dark Star might form. In the remainder of this work, we use a benchmark case from this preferred region: $m_\chi = 100\,\mathrm{GeV}$, $m_\phi = 10\,\mathrm{MeV}$, and $y_f = 8 \times 10^{-5}$, as highlighted by the red star in Fig. 3.2.

3.3 Gravothermal Evolution of SIDM Halos

As discussed in the introduction, there are two necessary conditions for the formation of Dark Stars. In the previous section we showed that the first condition can be met in a consistent SIDM model, namely that the power from dark matter annihilation can be deposited in the hydrogen cloud. In this section, we argue that the second condition can be satisfied, i.e. that the dark matter density in the collapsing hydrogen cloud can be high enough for dark matter heating to overcome the baryonic cooling processes.

The heating rate resulting from dark matter annihilation integrated within a sphere of radius R is

$$L_{\mathrm{DM}} = \frac{(\sigma v)_{\mathrm{eff}}}{2m_\chi} \int_0^R \mathrm{d}r \, 4\pi r^2 \rho_{\mathrm{DM}}^2(r) \,, \tag{3.10}$$

where ρ_{DM} the dark matter density and $(\sigma v)_{\mathrm{eff}}$ is the annihilation cross section which,

for the SIDM model, is expressed by Eqs. (3.2)–(3.3). Up to $\mathcal{O}(1)$ factors[6], Eq. (3.10) is also applicable for a Dark Star powered by WIMP annihilation [71]. Hence, we can use the results from the studies of Dark Stars in the WIMP scenario to estimate the required dark matter densities for dark matter heating to overcome the baryonic cooling processes. As discussed in Sec. 3.2, at the dark matter velocities relevant in a dark star, $(\sigma v)_{\text{eff}}$ in the SIDM scenario can be much larger than the benchmark value $(\sigma v)_{\text{eff}} \sim 3 \times 10^{-26} \, \text{cm}^3/\text{s}$ appropriate for Majorana fermion WIMPs produced via s-wave freeze-out. Thus, requiring SIDM to reach larger densities than the minimal dark matter densities previous studies for WIMP powered Dark Stars found for Dark Star formation is a *conservative* criterion – due to the larger $(\sigma v)_{\text{eff}}$, SIDM is more effective at heating the baryons than WIMPs for the same ρ_{DM}.

In the WIMP case, the dark matter density in the collapsing hydrogen cloud is controlled by adiabatic contraction. This leads to a relation between ρ_{DM} and the gas number density n_{gas} at the edge of the baryonic core as $\rho_{\text{DM}} \approx 5 \, \text{GeV} \, \text{cm}^{-3} \, (n_{\text{gas}}/\text{cm}^{-3})^{0.81}$ [71]. For a $m_\chi = 100 \, \text{GeV}$ WIMP mass and $(\sigma v)_{\text{eff}} = 3 \times 10^{-26} \, \text{cm}^3/\text{s}$, Ref. [71] found that dark matter heating overcomes the baryonic cooling processes for a gas density of $n_{\text{gas}} \sim 10^{13} \, \text{cm}^{-3}$ [71]. The baryonic core has a size of $r \sim 4 \times 10^{-4} \, \text{pc}$ at that stage, and the dark matter density at the edge of the baryonic core is $\rho_{\text{DM}} \sim 2 \times 10^{11} \, \text{GeV/cm}^3$.

Can such densities be reached in an SIDM halo? Consider a $\sim 10^7 \, M_\odot$ halo at redshift $z \sim 20$, which simulations suggest to be the birth place of the first stars in the Universe [72; 136; 10]. For these halos, the scale radius and characteristic density are typically $r_s \sim 50 \, \text{pc}$ and $\rho_s \sim 100 \, \text{GeV/cm}^3$, respectively. For a pure SIDM halo, self-interactions produce a shallow density core with the central density approaching ρ_s, which is many orders of magnitude lower than the threshold densities required to power a Dark Star.

---

[6]In the case of WIMPs, typically a third of the heating rate will be lost to neutrinos escaping the star. Furthermore, for Majorana fermion dark matter an additional factor 2 must be included compared to Dirac fermions.

However, the presence of the baryonic gas in the protogalaxies that host the first stars dramatically changes the gravothermal evolution of the halo, resulting in high central dark matter densities. Ref. [9] performed simulations of the evolution of an SIDM halo under the influence of the baryonic potential in such protogalaxies. The initial conditions in Ref. [9] were based on the result of Ref. [10] for such protogalaxies: the initial dark matter profile for a $3.5 \times 10^7 \, M_\odot$ halo at $z \approx 16$ is fit by a Navarro-Frenk-White (NFW) profile [30] with scale radius $r_s \approx 73 \, \mathrm{pc}$ and characteristic density $\rho_s \approx 98.9 \, \mathrm{GeV/cm^3}$, while the gas density profile is fit by a power law, $\rho_{\mathrm{gas}} \propto r^{-2.4}$.

Fig. 3.3 shows the evolution of SIDM density profiles in the presence of the baryonic potential, based on the simulations in Ref. [9], where time is measured in units of the characteristic time $t_0 = 1/\sqrt{4\pi G \rho_s} \approx 2.6 \, \mathrm{Myr}$, a convenient time-scale to measure the evolution of self-gravitating systems. As we can see in Fig. 3.3, the dark matter density in the inner regions of the halo increases rapidly, for example, at $t = 2t_0$, the density at a radius $r \sim 4 \times 10^{-4} \, \mathrm{pc}$ reaches $\rho_{\mathrm{DM}} \gtrsim 10^{12} \, \mathrm{GeV/cm^3}$, *larger* than the threshold density for a WIMP Dark Star discussed above. For a more global comparison of the dark matter densities, we also show the density profile for WIMP dark matter after adiabatic contraction starting from the same NFW profile and under the effect of the same gas density as for the SIDM case in Fig. 3.3. This result is obtained using the publicly available `contra` code [165]. The density of SIDM at $t = 2t_0$ already surpasses the density of WIMPs after adiabatic contraction in the inner region ($r \lesssim 10^{-2} \, \mathrm{pc}$) of this halo. Thus, via the gravothermal evolution of SIDM under the influence of the gravitational potential of the baryons, the inner region of the SIDM halo could provide sufficiently high dark matter densities to form a Dark Star and the influence of the gravitational potential of the baryons dramatically changes the gravothermal evolution of the SIDM halo. An SIDM-only halo would have first formed a shallow isothermal core, and the gravothermal core collapse (or gravothermal catastrophe) would only have occurred on much longer timescales,

$t \sim (10^2\text{–}10^3)t_0$ [167; 168; 171]; see also Refs. [210; 211; 212] for recent work on the gravothermal evolution of SIDM-only halos. The deep baryonic potential can trigger the onset of gravothermal collapse of the SIDM halo [147; 148; 149; 9; 150] on timescale of order t_0, leading to extremely high central dark matter densities [167; 168; 169; 170; 171; 172; 173; 213; 214; 215; 216; 217; 218].

The results in Fig. 3.3 stem from the simulations in Ref. [9]. These simulations use a semi-analytical conducting fluid model and assume a static baryonic potential, allowing Ref. [9] to achieve sufficiently high spatial resolution to resolve the central halo, necessary for us to evaluate the conditions of Dark Star formation. The overall results are consistent with the findings in recent hydrodynamical N-body simulations [216], showing that in the presence of a highly concentrated baryon profile, the inner SIDM halo is more dense than its collisionless dark matter counterpart.

In addition, Ref. [9] considers a fixed dimensionless cross section parameter $(\sigma_{\rm SI}/m_\chi)(r_s\rho_s) = 0.2$. Taking the halo parameters $\rho_s = 73\,{\rm pc}$ and $\rho_s = 98.9\,{\rm GeV/cm^3}$, this corresponds to $\sigma_{\rm SI}/m_\chi \approx 7.3\,{\rm cm^2/g}$, which is within the favorable range of $\sigma_{\rm SI}/m_\chi$ shown in Fig. 3.2. Given the rapid growth rate of the central SIDM density indicated in Fig. 3.3, we expect that smaller values of $\sigma_{\rm SI}/m_\chi$ would still lead to sufficiently high dark matter densities for dark matter heating to overcome baryonic cooling processes. However, determining the range of self-interaction strengths for which the evolution of the SIDM halo under the influence of the collapsing hydrogen cloud leads to sufficiently high dark matter densities for Dark Stars would require running a suite of simulations which we leave for future work.

3.4 Properties of SIDM Dark Stars

In Secs. 3.2 and 3.3 we have shown that the necessary conditions for the formation of Dark Stars can be met in the SIDM scenario, namely that the dark matter density in the environments where Dark Stars would form can be high enough to make dark
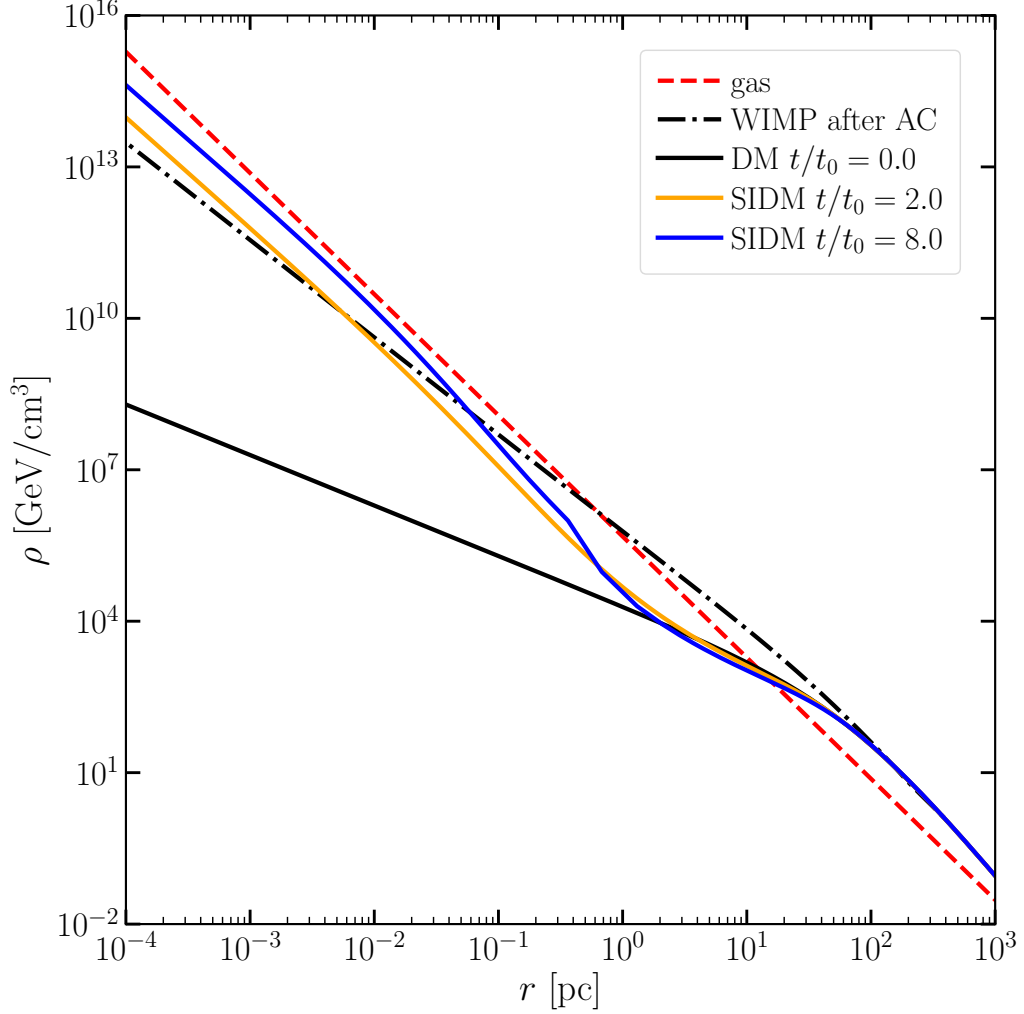
Figure 3.3: Gravothermal evolution of an SIDM halo in the presence of a static gravitational potential source by baryonic gas (measured in units of the characteristic time $t_0 = 1/\sqrt{4\pi G \rho_s} \approx 2.6\,\text{Myr}$). The different lines show the dark matter density profiles at $t/t_0 = 0$ (solid black), 2 (solid orange) and 8 (solid blue); based on SIDM simulations in Ref. [9], where the gas (dashed red) and initial dark matter (solid black) density profiles are from hydrodynamical cosmological simulations of protogalaxies [10]. For comparison, the dash-dotted black line shows the density profile for a WIMP halo with the same initial dark matter profile undergoing adiabatic contraction by the same gas profile.

matter annihilation a sufficiently strong power source to overcome the baryonic cooling processes, and that the energy from dark matter annihilation can be deposited in the hydrogen cloud to power a Dark Star. Once the energy injection from dark matter annihilation surpasses the energy loss due to baryonic cooling, the dissipative collapse of the gas slows down. Eventually, the baryons can reach hydrostatic equilibrium, resulting in a Dark Star.

As discussed in Sec. 3.3, the evolution of the baryonic and SIDM densities are deeply intertwined, hence, determining the properties of SIDM Dark Stars such as their luminosity, surface temperature, or size requires detailed simulations of the coupled evolution of the baryonic and SIDM fluids including the various baryonic cooling mechanisms, the heat transport in the SIDM component, and the coupled gravothermal evolution of the baryonic and SIDM fluids. Such dedicated numerical studies are beyond the scope of this work. In order to gain a first glimpse on the properties of SIDM powered Dark Stars and how they compare with their counterparts in the WIMP scenario, we will make the simplified assumption that the SIDM distribution in the Dark Star is isothermal. This assumption is motivated by the fact that while SIDM efficiently self-scatters (and hence self-thermalizes), the interactions of SIDM with baryons are much weaker. Furthermore, we initially treat the SIDM-to-baryon mass ratio inside the photosphere of the Dark Star $f_{\rm DM}$ as a free parameter, which we later fix when discussing numerical results using a prescription described below.

The dark matter and baryonic gas distributions in the Dark Star are described by

$$\nabla p_{\rm DM} = -\rho_{\rm DM} \nabla \Phi \,, \quad \nabla p_{\rm gas} = -\rho_{\rm gas} \nabla \Phi \,, \tag{3.11}$$

where $\rho_{\rm DM}$ ($\rho_{\rm gas}$) and $p_{\rm DM}$ ($p_{\rm gas}$) are dark matter (gas) density and pressure, respectively, and Φ is the gravitational potential. The two components are coupled via the

Poisson equation,

$$\nabla^2 \Phi = 4\pi G(\rho_{\text{gas}} + \rho_{\text{DM}}) \,. \tag{3.12}$$

We assume that the baryonic gas satisfies a polytropic equation of state, $p_{\text{gas}} = K_{\text{gas}} \, \rho_{\text{gas}}^{1+1/n}$, where n is the polytropic index and $K_{\text{gas}} \equiv p_{\text{gas}}(0)/\rho_{\text{gas}}^{1+1/n}(0)$ is a constant of proportionality evaluated at radius $r = 0$. Furthermore, we assume that the SIDM profile is described by an isothermal distribution, corresponding to a polytrope with $n = \infty$ or $p_{\text{DM}} = K_{\text{DM}}\rho_{\text{DM}}$. Since Dark Stars are dominantly composed of baryons ($f_{\text{DM}} \ll 1$), the baryonic mass dominates the gravitational potential with $\Phi(R) \approx -GM_\star/R$, where $M_\star$ is the baryonic mass enclosed in a given stellar radius R. Assuming that the dark matter in the Dark Star is virialized, we have $K_{\text{DM}} = GM_\star/(3R)$. In addition, we evaluate the SIDM annihilation cross section in the star using the dark matter root-mean-square speed $\sqrt{\langle v^2 \rangle} = \sqrt{GM_\star/R}$.

Assuming spherical symmetry, we obtain dark matter and stellar density profiles iteratively in the following way. We take $M_\star$ and f_{DM} as input parameters and make an initial guess for the stellar radius R, then solve Eqs. (3.11)-(3.12), supplemented with the equations of state for SIDM and gas. Following the prescription in [219], we interpolate the polytropic index of the gas profile between $n = 3/2$ (fully convective star) and $n = 3$ (fully radiative star), depending on the gas density. We write the pressure profile inside the star as a sum of the matter and the radiation pressures,

$$p_{\text{gas}}(r) = \frac{\rho_{\text{gas}}(r)}{\mu \, m_u} k_B T_{\text{gas}}(r) + \frac{1}{3} a T_{\text{gas}}^4(r) \,, \tag{3.13}$$

where $\mu \approx 0.588$ is the mean molar mass of gas particles [73], $m_u \approx 0.933\,\text{GeV}$ is the atomic mass unit, k_B is Boltzmann's constant, and the radiation constant $a = 4\sigma_{\text{SB}}$ is related to the Stefan-Boltzmann constant σ_{SB} (we remind that we use units with $c = 1$). We invert Eq. (3.13) to obtain the temperature profile $T_{\text{gas}}(r)$. From $T_{\text{gas}}(r)$ and $\rho_{\text{gas}}(r)$ profiles, we calculate the Rosseland mean opacity κ by interpolating zero-
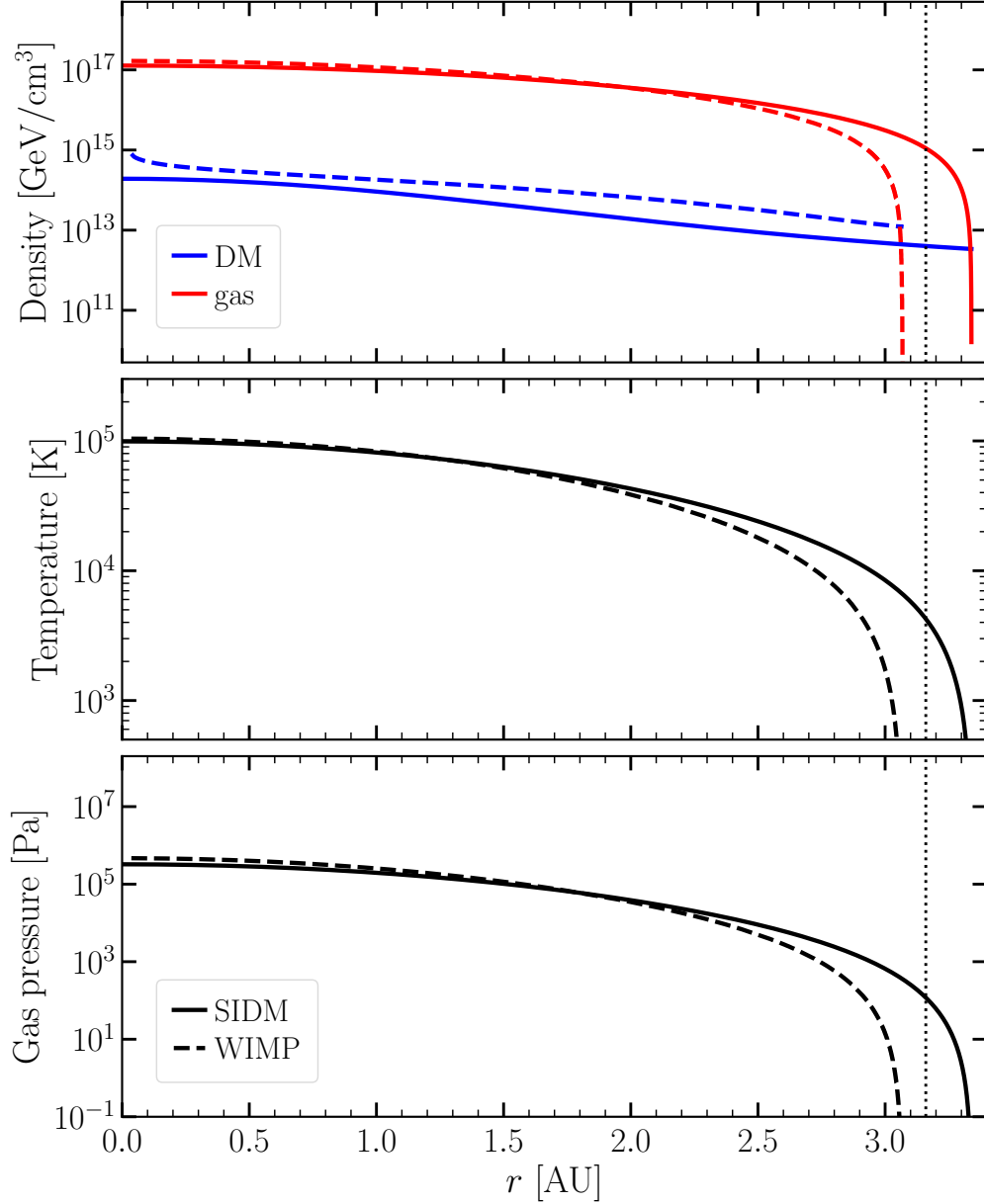
Figure 3.4: The profiles of gas (red) and dark matter (blue) densities (top), temperature (middle) and pressure (lower) of $10\,M_\odot$ SIDM-powered (solid lines) and WIMP-powered (dashed lines) Dark Stars. Both cases are for a dark matter particle mass of $m_\chi = 100\,\mathrm{GeV}$. For the SIDM-powered Dark Star, we set the SIDM-to-baryon mass ratio in the Dark Star to $f_{\mathrm{DM}} = 7.4 \times 10^{-4}$ such that both Dark Stars have the same total luminosity, $L_{\mathrm{eff}} = 1.5 \times 10^5\,L_\odot$. The vertical dotted black line indicates the photosphere radius of the SIDM-powered Dark Star, $R_\star = 3.2\,\mathrm{AU}$, and the photosphere temperature of the SIDM Dark Star is $T_{\mathrm{eff}} = 4300\,\mathrm{K}$. For the WIMP Dark Star, we find $R_\star = 2.9\,\mathrm{AU}$ and $T_{\mathrm{eff}} = 4600\,\mathrm{K}$.

metallicity tables [220; 221]. The photosphere radius $R_\star$ is given by the condition

$$\kappa p_{\text{gas}}(R_\star) = \frac{2}{3} \frac{\mathrm{d}\Phi(r)}{\mathrm{d}r}\bigg|_{r=R_\star}. \qquad (3.14)$$

At the photosphere radius $R_\star$, we calculate the effective temperature as $T_{\text{eff}} = T_{\text{gas}}(R_\star)$ and the effective luminosity,

$$L_{\text{eff}} = 4\pi\sigma_{\text{SB}} R_\star^2 T_{\text{eff}}^4. \qquad (3.15)$$

We compare L_{eff} with the total luminosity L_{DM} produced from dark matter annihilation, see Eq. (3.10). We iteratively adjust the stellar radius R and repeat the procedure described above until L_{DM} and L_{eff} match: $|L_{\text{DM}} - L_{\text{eff}}|/(L_{\text{DM}} + L_{\text{eff}}) < 0.05$. We do not consider nuclear fusion as a power source; the radii of the smallest Dark Stars considered in the iterative process are much larger than those of ordinary Pop-III stars and the cores of Dark Stars are not dense and hot enough to start nuclear fusion.

In Fig. 3.4 we show the gas and dark matter density profiles (top) as well as the temperature (middle) and pressure (bottom) profiles for $M_\star = 10\,M_\odot$ SIDM-powered (solid) and WIMP-powered (dashed) Dark Stars. The solution for the WIMP-powered Dark Star is found following the procedure outlined in Ref. [71]; in particular, the dark matter density profile in the Dark Star is obtained by adiabatic contraction of a $10^7\,M_\odot$ NFW halo at redshift $z \sim 20$ with concentration parameter $c_{\text{NFW}} = 3$. We assume a WIMP of mass $m_\chi = 100\,\text{GeV}$ and set the annihilation cross section to $(\sigma v)_{\text{eff}} = 3 \times 10^{-26}\,\text{cm}^3/\text{s}$, yielding the observed dark matter relic density for a Majorana fermion WIMP annihilating via s-wave processes. For the SIDM Dark Star, we take the benchmark case from the end of Sec. 3.2: $m_\chi = 100\,\text{GeV}$ dark matter particle mass, $m_\phi = 10\,\text{MeV}$ mediator mass, and the annihilation cross section in the Dark Star is calculated using Eq. (3.3) fixing the effective annihilation cross section at

freeze-out to $(\sigma v)_{\mathrm{eff}} = 6 \times 10^{-26} \, \mathrm{cm}^3/\mathrm{s}$ such that one obtains the observed dark matter relic density for the Dirac fermion dark matter candidate χ. In order to match the total luminosity of the SIDM-powered Dark Star to that of the WIMP-powered Dark Star, $L_{\mathrm{tot}} = 1.5 \times 10^5 \, L_{\odot}$, we set the SIDM-to-baryon mass ratio to $f_{\mathrm{DM}} = 7.4 \times 10^{-4}$.

In Fig. 3.4, we also indicate the photosphere radius $R_{\star} = 3.2 \, \mathrm{AU}$ of the SIDM Dark Star with the vertical dotted black line. The dark matter density drops gradually with increasing radius r, and it extends beyond the photosphere. For the gas, its density, temperature, and pressure profiles follow a similar trend within $R_{\star}$, but drop quickly for $r \gtrsim R_{\star}$. Comparing the profiles of the SIDM- and WIMP-powered Dark Stars, we can note that their properties are rather similar – while the SIDM Dark Star has $R_{\star} = 3.2 \, \mathrm{AU}$, the WIMP Dark Star is slightly smaller/denser with $R_{\star} = 2.9 \, \mathrm{AU}$. In turn, the SIDM Dark Star is somewhat colder; its effective photosphere temperature is $T_{\mathrm{eff}} = 4300 \, \mathrm{K}$, while the photosphere temperature of the WIMP Dark Star is $T_{\mathrm{eff}} = 4600 \, \mathrm{K}$.

3.5 Summary and Conclusions

We have shown that the necessary conditions for the formation of Dark Stars can be met in the SIDM scenario. In particular, this work demonstrates that in a concrete SIDM particle physics model satisfying all current constraints, the power from dark matter annihilation can be deposited in the baryonic gas. When the baryonic gas cloud in the $(10^6$–$10^8) \, M_{\odot}$ protohalos thought to be the birthplaces of the first star collapses, the deepening gravitational potential can lead to gravothermal evolution of the SIDM fluid resulting in very high central dark matter densities. These densities are sufficiently high for the power from dark matter annihilation deposited in the baryons to overcome all baryonic cooling processes, giving rise to the appropriate conditions for forming a Dark Star. While investigating the detailed properties of such Dark Stars in the SIDM scenario once they have reached hydrostatic equilibrium is beyond

the scope of this work, we have given a first estimate of their properties assuming that the SIDM distribution in the Dark Star is isothermal and using the SIDM-to-baryon mass ratio in the Dark Star as an input parameter.

There are several relevant topics that require further investigations. In order to form a Dark Star, a high central density in the dark matter halo is required. In SIDM models, the presence of the baryonic gas can deepen the gravitational potential and increase the density accordingly. This effect has been confirmed in hydrodynamical simulations for Milky Way-like systems at low redshifts [216]. In order to study the properties of Dark Stars in the SIDM scenario such as their luminosity and surface temperature, dedicated dynamical simulations are needed. Such simulations need to model the gravitationally coupled evolution of the hydrogen and the SIDM distributions while simultaneously computing baryonic cooling rates and the effects of dark matter self-interactions and annihilation on both distributions. Furthermore, in the WIMP case, a Dark Star could grow through various processes such as baryon accretion [71; 75] or dark matter capture [137; 139]. In SIDM, dark matter particles could experience self-capture due to the large self-interaction cross section [222; 223]. Such a self-capture process could affect the formation and evolution of Dark Stars. It would also be interesting to study observational prospects of SIDM Dark Stars with, for example, the James Webb Space Telescope [224].

CHAPTER IV

Cluster Analysis in Action Space to Constrain Accretion History of Milky Way-like Galaxies

[1]

4.1 Introduction

In the currently favored cosmological paradigm galaxies form hierarchically through the accretion and merger of numerous satellite subhalos. N-body simulations of galaxy formation make strong predictions about the number of dark matter subhalos and their mass functions and the mass assembly rates of halos. Using cosmological simulations it has been shown that mass functions of subalos (at different redshifts) is a strong discriminator between cold dark matter (CDM) and alternative forms of dark matter (e.g. Warm Dark Matter (WDM), Self-interacting Dark Matter (SIDM)). In particular the number of subhalos in present day Milky Way (MW) mass halos in the mass range $10^6 - 10^{10} \, \mathrm{M_\odot}$ is sensitive to the nature of dark matter [for recent reviews see, 79; 80]. In addition, in ΛCDM the merger rate of dark matter halos per unit mass ratio (relative to the host halo at the time of accretion), per redshift interval has a nearly universal functional form [226].

---

[1]This chapter is based on the paper [225] published in MNRAS.

Several novel methods are being used to detect dark (or nearly dark) subhalos in the Milky Way's halo: modeling gaps in thin stellar streams that may have resulted from impact with a dark subhalo [e.g. 227; 228; 229], perturbations to the Galactic disk by dark matter subhalos, which might produce bending modes or wiggles or corrugations in the density of the disk [230] which may already have been detected in the solar vicinity [231] and on slightly larger scales [232]. Dark matter subhalos of masses $\gtrsim 3 \times 10^9 \, \mathrm{M_\odot}$ tend to be massive enough to retain their baryons and form stars [e.g. 233]. Many of these subhalos are currently detectable as satellites (dwarf spheroidal galaxies and ultra faint dwarf galaxies) in the Local Group. In addition, satellites that were accreted throughout the Milky Way's history have been tidally disrupted by the Galactic potential and now form much of the stellar halo of the Milky Way. If it is possible to observationally dissect the stellar halo of the Milky Way to reliably identify the stellar debris of such satellites, one could use the kinematics and chemical abundance signatures in the debris to determine properties (e.g. masses) of the progenitors. We would also be able to use this information to determine the accretion history of our Galaxy and possibly quantify the mass function of accreted satellites.

Early work [e.g. 234; 235; 236; 237] showed that merger remnants remain coherent in phase space (or integrals-of-motion space) long after they have become so phase mixed that they are impossible to detect via their spatial distributions. Most early works have focused on finding coherent structures in energy, angular-momentum, or velocity space. Since stars in a galaxy are collisionless, the space of orbital actions, integrals-of-motion that are conserved even under adiabatic changes to the underlying gravitational potential, are particularly promising [for a detailed introduction see, 90]. Since accreted substructures are much less massive than the host halo, they occupy a much smaller volume in the action space defined by the gravitational potential of the host halo, implying that stars from the same progenitor could still be clustered

in the action space at $z = 0$, making it possible to detect these mergers events.

The advent of *Gaia* [238; 239; 240; 241; 242; 243] is making it possible to obtain 6-dimensional phase space information for hundreds of thousands to tens of millions of halos stars. Numerous efforts are underway to automatically identify substructures in the phase space. With the SDSS-*Gaia* DR1 catalogue of ~ 80000 main sequence turn-off halo stars in 7D phase space (3D position+3D velocity+metallicity), Ref. [244] showed that metal-rich halo stars were on significantly more radial orbits than metal poor stars. They inferred that this highly anisotropic velocity distribution was consistent with a single, head-on accretion event by a satellite with mass above $10^{10}\,\mathrm{M_\odot}$. This satellite was named the "*Gaia* Sausage" at that time. It was soon after re-discovered in *Gaia*-DR2 data based on chemistry, dynamics and stellar population analysis, and was named "*Gaia* Enceladus" [245]. Now this satellite is referred to as "*Gaia* Enceladus Sausage" (GES).

Ref. [246] analyzed the same SDSS-*Gaia* catalog in action space ($\{J_r, J_z, J_\phi\}$) to show that the metal-rich stars were more extended toward high radial action J_r and more concentrated around the $J_\phi = 0$, showing different patterns from metal-poor stars, in agreement with Ref. [244]. Ref. [247] developed an algorithm to find over-densities in action space, and used the metallicity as a secondary check. They identified 21 substructures in the SDSS-*Gaia* catalogue, and argued that 5 of them are associated with the accretion of the progenitor of ω Centauri, inferring the minimum mass of the ω Centauri progenitor to be $5 \times 10^8\,\mathrm{M_\odot}$. Ref. [248] applied the clustering algorithm DBSCAN to search for streams in integrals of motion space. Ref. [249] applied several clustering algorithms to energy+actions space coordinates for 35 nearby r-process-enhanced field halo stars (obtained using *Gaia* proper motions, radial velocities and parallaxes) and were able to identify 8 separate clusters with statistically distinct[2] iron abundances, supporting the view that the 35 stars were likely to have

---

[2]The spread in iron abundance, $\sigma_{[Fe/H]}$, in their clusters was significantly smaller than the spread for randomly drawn groups of halo stars of the same size, from their sample.

been accreted in 8 distinct satellites (clusters) in the action space. Ref. [250] searched for dynamical substructures in the LAMOST DR3 catalog of very metal-poor stars cross-matched with *Gaia* DR2 by applying the self-organizing map algorithm StarGO. They identified 57 dynamically tagged groups, many of which belonged to previously identified accretion events. Ref. [251] applied the clustering algorithm HBSCAN to 4D energy-action data of 1500 very metal poor stars based on spectroscopic data from the HK and Hamburg/ESO surveys, and found 38 dynamically tagged groups, with many of them corresponding to previously known substructures and 10 of them being new. Ref. [252] used HBSCAN on 4D energy-action data of 446 r-process-enhanced stars in the halo and the disk of the Milky Way, and found 30 chemo-dynamically tagged groups (CDTGs), with stars from the same CDTG showing statistically significant similarities in their metallicities, indicating that stars from the same CDTG have experienced common chemical evolution histories in their parent substructures prior to entering the Milky Way halo. Ref. [253] and Ref. [254] used clustering algorithms to identify clusters in phase space (primarily position-velocity space) and have found debris of several previously known and newly discovered satellites, including evidence for the accretion of a prograde satellite close to the disk plane that they named "Nyx". Recently, Ref. [255] have used chemical abundances and stellar parameters data from the GaLAH and APOGEE surveys to argue that the "Nyx" stream is more consistent with a high-velocity component of the thick disk origin, rather than a dwarf galaxy origin.

Hamiltonian dynamics tells us that accretion events should remain coherent in the action space for a very long time, as long as the potential changes slowly enough. However, it is as yet uncertain how long one can expect structures to remain coherent in a Milky Way like galaxy that grows hierarchically. The discovery of fairly massive past mergers like the "*Gaia* Sausage" and the "Sequoia" [256] galaxy, the on-going mergers like the Sagittarius stream [257] and future mergers like the LMC [258; 259]

raises questions about how "adiabatic" the evolution of the Milky Way has been and therefore how well one might distinguish other individual merger events. Is there a boundary in infall time such that satellites that fell in before this time have experienced so much phase mixing, that we can no longer find them through cluster analysis in the action space? The average density of satellite within its tidal radius relative to the mean density of the host within the satellite's orbit roughly determines its rate of tidal disruption. However, the mass of the satellite also determines the initial dispersion of its stars in action space and hence its expected degree of clustering. Therefore is there an optimal range of mass for satellites that can be detected via cluster analysis in phase space? The reliability of cluster analysis algorithms in finding substructures is also poorly understood: while numerous clusters are often identified by such algorithms, it is unclear how many of them correspond to discrete building blocks (individual satellites), how many are comprised of multiple satellites, how many are subcomponents of individual satellites and how many are spurious. The primary goal of this chapter is to find a metric (or metrics) computed from cluster analysis that quantify the correspondence between groups identified by cluster analysis and real galactic building blocks in the hierarchical galaxy formation framework when we complete and error free data. In a future paper we will consider how observational error and partial data on individual satellites affect the recovery process.

The cosmological hydrodynamic zoom-in simulations of Milky Way (MW)-mass galaxies from the Feedback In Realistic Environments (FIRE) project [3] [260] provide a great testbed for addressing these questions. We focus on three MW-mass galaxies from the Latte suite of FIRE-2 simulations which have different merger histories, ranging from one with a very quiescent recent history to one with a very active recent history. In Section 4.2 we describe how the simulation snapshots were analyzed to identify the accreted stars in the three halos at $z = 0$. In Section 4.3.1 we provide a

---

[3]website: https://fire.northwestern.edu/

brief introduction to the calculation of actions $\{J_r, J_z, J_\phi\}$ in cylindrical coordinates using publicly available AGAMA code [91]. In Section 4.3.2 we describe the density-based hierarchical cluster analysis algorithm *Enlink* [93] which we use to perform the cluster analysis in 3D action space. In Section 4.4.1 we study the overlap between the real stellar building blocks (disrupted satellites) of the three MW-mass galaxies and the groups found by *Enlink*. We define several metrics that we use to evaluate the accuracy of recovery of substructure with *Enlink*. We also use a binary classification tree to statistically determine boundaries in infall time (T_{infall}), total progenitor mass (M_{tot}) and stellar mass at $z = 0$ (M_{stellar}) for well-recovered and poorly-recovered satellites. The stellar halo of the host galaxy contains both accreted stars and *in situ* stars. The *in situ* stars are formed in the host galaxy and are in the stellar halo of the host galaxy at $z = 0$. In Section 4.4.2 we include varying fractions of *in situ* star particles into our analysis and study the robustness of our results against contamination from these stars. Finally, in Section 4.5 we discuss how the boundaries (in T_{infall} M_{tot} and M_{stellar}) separating well-recovered and poorly recovered satellites depend on the dynamical history of the host MW-like galaxies. We then summarize our results and conclude.

4.2   Simulation Data

Our analysis uses cosmological baryonic zoom-in simulations of MW-mass galaxies from the FIRE project [260]. These simulations are run with `GIZMO` [261] which uses an optimized TREE+PM gravity solver and a Lagrangian mesh-free, finite-mass method for accurate hydrodynamics. Star formation and stellar feedback are also implemented. All halos were simulated in ΛCDM cosmology at particle mass resolution of $\sim 7100\,\mathrm{M}_\odot$ and spatial resolution of 1–4 pc for star/gas particles, and a particle mass resolution of $\sim 35,000\,\mathrm{M}_\odot$ and spatial resolution of 40 pc for dark matter particles. The complete sample currently consists of 8 MW-mass galaxies and

3 Local-Group-like pairs. Ref. [92] and Ref. [262] show that when baryonic physics is included, the properties of dwarf galaxies in the FIRE-2 simulations agree well with observations of Local Group (LG) satellites down to the resolution limit (just below classical dwarf mass of $\sim 10^6 \, \mathrm{M_\odot}$ in stellar mass). Of particular importance for this work, the simulations produce satellites with mass–size and mass–velocity dispersion relations consistent with observations of the MW and M31 [262] distributed similarly with respect to their massive hosts [263; 264]. This implies that we expect the sizes and relative positions of the accreted structures in action space to resemble those in the Milky Way.

To assign the accreted star particles to particular progenitor galaxies, the dark matter particles in each snapshot of the simulations are first processed with `Rockstar` to produce halo catalogs, which then are connected in time to form a merger tree [265; 266]. `Rockstar` computes the maximum circular velocity v_{max} and the virial radius for each halo and subhalo identified in the dark matter distribution. A star particle is considered part of a halo or subhalo if it is within the virial radius *and* its velocity with respect to the center of that halo or subhalo is less than $2v_{\mathrm{max}}$[267; 268]. Within the host halo, this selection does a good job in picking out star particles gravitationally bound to a subhalo rather than the host halo.

One of the challenges with identifying substructure in the stellar halo is that there are indications from cosmological hydrodynamical simulations that some fraction of the stars in the halo of a Milky Way like galaxy were not accreted from satellites but were born *in situ* in the host galaxy, both at very early times before the disk was well established [e.g. 269] and in smaller proportions at later times, in gas propelled into the halo by star-forming winds [e.g. 270]. These stars then remain in the stellar halos of these MW-like galaxies at $z = 0$, a generic prediction of multiple simulations using independent codes and differing star-formation and feedback prescriptions [271; 272; 273; 274; 275; 276; 277]. However, these various cosmological

simulations predict a wide range of values for the *fraction* of halo stars that were formed *in situ* , which probably varies with assembly history and likely also depends on the feedback prescriptions adopted by different codes. While some simulations predict that up to 80% of the stellar halo was formed *in situ* , observations of the MW stellar halo [278; 279] find that almost all of it shows significant substructure, implying that a significant portion of the Milky Way stellar halo was accreted (although *in situ* stars formed in outflows may also be clustered; [270]) Analysis of data from the cross match between several stellar surveys like *Gaia*, RAVE and APOGEE shows that a fraction of halo stars in the solar neighborhood (within a few kpc from the Sun) are formed *in situ* in the Milky Way galaxy [280; 245; 281; 282; 283; 284].

Recently Ref. [285] showed that they were able to train and validate a deep learning neural network algorithm on 5D mock *Gaia* kinematical data [286] from the same simulations we use here [92; 260] to separate *in situ* halo stars from accreted stars. They then applied this method to 72 million stars in the *Gaia* DR2 catalog with parallax measurement errors of less than 10% and were able to identify over 650,000 stars as accreted. They then used a cluster finding algorithm to identify clusters in phase space and their comparisons with other datasets allowed them to validate both robustness of their neural network algorithm for separating *in situ* stars, and identify several new structures [253; 254]. Based on the success of such algorithms to separate accreted and *in situ* stars, we assume in this chapter that such separation is possible, and we use information derived from the analysis of simulation snapshots to identify accreted satellites in the simulations.

We focus on three MW-mass galaxies: m12i, m12f and m12m. For each galaxy there are 600 snapshots from $z = 99$ to $z = 0$, with a time difference between snapshots of approximately 25 Myr at late times. This relatively high "framerate" allows us to track the time-evolution of accreted structures in much of the host galaxy with ∼10–100 snapshots per dynamical time. Since it takes several dynamical times

for a self-bound satellite to be tidally disrupted and turn into a stream, we select luminous halos that are self-bound between 2.7 to 6.5 Gyr ago and that are within the virial radius of the host galaxy at present day. These time scales correspond to redshift $z \approx 0.25 - 0.75$. During this time window, these luminious halos can either be inside (bound) or outside (unbound) the virial radius of the host galaxy. We follow each substructure throughout its evolution to recover most of the star particles that once belonged to the satellite. These star particles are then tracked forward to $z = 0$. The stellar mass of each substructure at $z = 0$ is summed up to get M_{stellar}. From $z = 0$, star particles belonging to a particular substructure are also traced back in time until the substructure is no longer bound to the host halo. This time is defined as the infall time T_{infall} of the substructure, and all the mass belonging to this substructure at T_{infall} is summed up to get the total mass of the satellite (stars, gas and dark matter) M_{tot}. Extending the sampling time window to a time beyond 6.5 Gyr ago might help detect satellites that are tidally disrupted very early on. However, these additional satellites are less likely to be clustered in action space because the evolution of the host galaxy potentials are non-adiabatic until ~ 5 Gyr ago, which is the end of the bursty phase of star formation in these simulations [270]. The satellites disrupted prior to this epoch will be studied in Horta et al. (in prep.). Moreover, for $z \gtrsim 2$–4, there is no clear "host" galaxy in terms of mass [269], and the disk of what eventually becomes the most massive galaxy is not usually formed yet at that point [287], so the question of what is accreted onto what is not well-defined.

Starting with the star particles assigned to each accreted structure, we make three selections on both real space and velocity space to identify disrupted satellites, both phase-coherent (streams) and phase-mixed satellites. In the first selection, we choose satellites with stellar mass between $M_\star \approx 10^6 \, \mathrm{M_\odot}$ and $10^9 \, \mathrm{M_\odot}$ at $z = 0$. In the second selection, we use the fact that the "size" of disrupted substructures in physical space is larger than that of satellite galaxies that are still self-gravitating at $z = 0$. In

practice, we define the "size" of a substructure as the maximum value of the pairwise distance between two star particles in a substructure at $z = 0$. To take advantage of this fact and rule out the self-gravitating satellite galaxies in the $z = 0$ snapshots, we require the "size" of each substructure we tracked to be greater than 120 kpc, as 120 kpc is much larger than the characteristic size of self-gravitating dwarf galaxies, as well as dwarf galaxies that are only slightly tidally deformed but without prominent tails [see Fig. 2 from 288].

The remaining accreted structures are classified by eye into two categories, coherent streams and phase-mixed debris, by viewing their configuration in position and velocity space. Ref. [288] shows that this by-eye classification corresponds to a selection in the space of stellar mass and local velocity dispersion, where "local" velocity dispersion is defined for each particle using nearest neighbors in phase space rather than position (at fixed stellar mass, phase-mixed satellites have higher local velocity dispersion compared to coherent streams). Although this classification is mildly resolution-dependent, the overall results when this classification is applied to the full sample of streams from all 13 analyzed systems in [288] demonstrate the mass- and time-dependence expected from theory for the relative abundance of phase-mixed versus coherent debris, implying that resolution effects do not dominate our classification of coherent streams and phase-mixed structures that are accreted.

In this work, we are interested in the action space clustering of tidally disrupted systems. Self-bound dwarf galaxies at $z = 0$ are already spatially clustered. Therefore, in this manuscript, the terms "satellites" and "accreted satellites" refer to disrupted satellites, including both present-day coherent streams and phase-mixed debris. Fig. 4.1 shows the tidally disrupted satellites in galaxy m12f in position space (left column), velocity space (middle column, velocities are shown in cylindrical coordinates) and r vs. v_r phase space (right column), where ρ is the radial coordinate, ϕ is the angular coordinate and z is the height in cylindrical coordinate system. Star par-
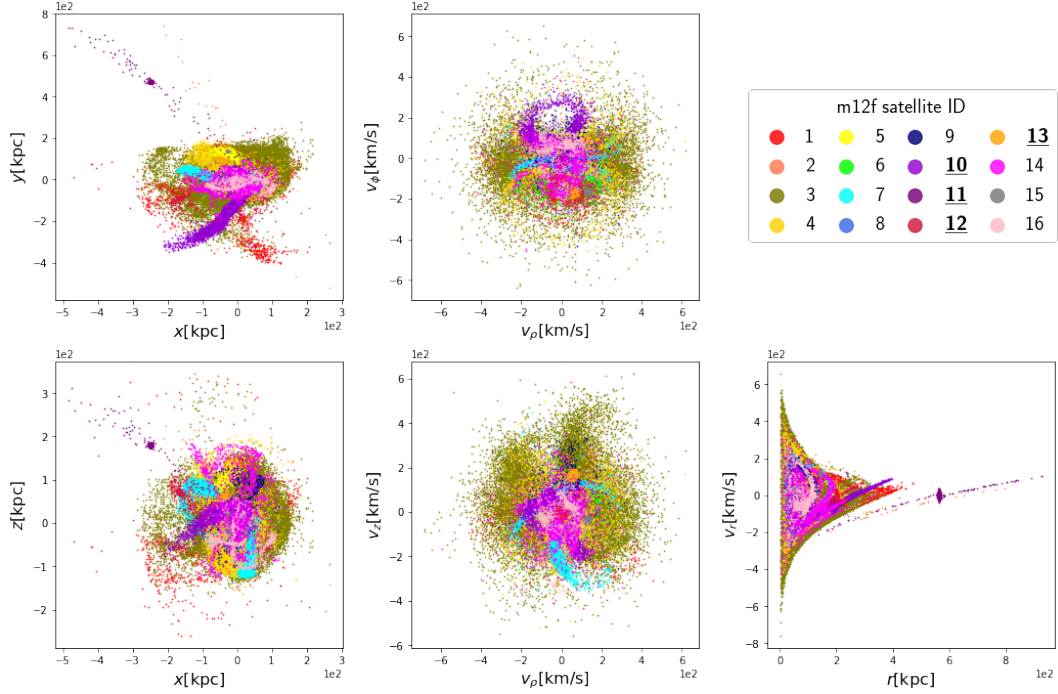
Figure 4.1: Tidally disrupted satellites in galaxy m12f are plotted in position space (left column), velocity space (middle column) and r vs. v_r phase space (right column). Star particles are colored differently according to different satellites they are assigned to by the tracking process. The well-recovered satellites are indicated with bold and underlined IDs in the legend. The well-recovered satellites outside $T_{\mathrm{infall}} < 7.1$ Gyr ago and $M_{\mathrm{tot}} > 4.0 \times 10^8 \, \mathrm{M}_\odot$ ($M_{\mathrm{stellar}} > 1.2 \times 10^6 \, \mathrm{M}_\odot$) are marked by bold and underlined IDs with a star (*) in the legend. We will explain the terms well-recovered, T_{infall}, M_{tot} and M_{stellar} in Section 4.4.1.

ticles from different satellites are colored differently. For similar plots of the satellites in the other two galaxies, see Appendix A.1

4.3   Methods

The orbits in a galactic potential are largely quasi-periodic and regular. Therefore the orbits of most satellites and individual stars in the halo of a galaxy can be described by an elegant set of variables – the action-angle variables. Orbital actions are particularly powerful for understanding the evolution of a galaxy since they are conserved under adiabatic evolution of the potential. Section 4.3.1 gives a brief

introduction to action-angle variables. We then use a publicly available dynamical modeling toolbox AGAMA [91], to numerically compute actions (under the assumption of axisymmetry) for the accreted star particles in the three MW like galaxies in FIRE-2 described in Section 4.2.

The initial actions of all the stars in a satellite as it orbits a larger galaxy have a small spread compared to the range of possible actions in the Galactic potential. Because actions are adiabatically invariant by construction, star particles from the same progenitor are expected to remain clustered in the action space at $z = 0$ if the gravitational potential of the host halo has changed only adiabatically (i.e. slowly enough) following their infall. Therefore, the accreted satellites found in Section 4.2 should be recoverable through cluster analysis in the action space. In Section 4.3.2, we feed the cluster analysis algorithm *Enlink* with the three-dimensional orbital actions of accreted star particles, and find several groups. To measure how well the groups found by *Enlink* recover the satellites tracked in Section 4.2, we define various metrics in Section 4.3.3.

4.3.1 Action Evaluation with AGAMA

In order to compute actions from the positions and velocities of star particles at $z = 0$ one needs an estimate of the gravitational potential. In the case of the real MW, this is derived using a multitude of observational tracers which provide the masses of the various stellar components (the bulge, thin and thick disk and stellar halo) and kinematics of disk stars and halo objects to derive the mass and density profile of the dark matter halo.

In this chapter we study 3 simulated disk galaxies from the FIRE-2 simulations with different accretion histories. We use the masses and positions of all the particles (dark matter, gas, stars) within 600 kpc from the center of galaxy to compute the gravitational potential of each galaxy at $z = 0$. This is done using AGAMA [91] which

76

approximates the gravitational potential via an axisymmetric multipole expansion on a hybrid cylindrical-polar grid (to compute the potential of the flattened stellar disk) and spherical polar grid (to compute the potential of the dark matter halo). The potential generated by dark matter and hot gas in the dark matter halo is represented by an expansion in spherical harmonics with $l_{max} = 4$; the potential from stars and cold gas in the disk is expanded in azimuthal-harmonics up to $m_{max} = 4$. The star, gas and dark matter particles within 600 kpc of the galactic center are used to calculate the potential. [for a detailed introduction to how these expansions work see, 91].

With the gravitational potential in hand, we use the positions and velocities of all accreted halo star particles (at $z = 0$) to compute the three actions J_r, J_ϕ and J_z defined by,

$$J_q = \frac{1}{2\pi} \oint \frac{p_q}{m} \, dq \qquad (4.1)$$

where m is the mass of a star particle, $q = r, \phi$ or z, and p_q is the canonical momentum corresponding to q. $\{J_r, J_\phi, J_z\}$ is the most useful set of actions in cylindrical or spherical coordinate systems. For context, J_ϕ is the same as angular momentum L_z. J_r and J_z describes the extent of oscillations in spherical radius and z dimension respectively. In AGAMA, the three actions are evaluated approximately using the Stäckel fudge method [289]. However, the error in actions introduced by the Stäckel fudge approximation is smaller than the error from assuming axisymmmetry in a potential that is actually triaxial (as is the case for the FIRE-2 galaxies). The assumption of oblate-axisymmetry is unavoidable since the current version of AGAMA's action-finder does not support triaxiality.

In this work we have assumed that all space coordinates for dark matter particles, gas particles and star particles are assumed known and without error when computing the potential. The main deviation from the potential used for computing the actions and the true gravitational potential comes from the spherical harmonic expansion. When computing the actions we further assume that the phase space coordinates for

all accreted star particles are known perfectly (i.e. no errors are added).

Fig. 4.2 shows three projections of the actions $\{J_r, J_\phi, J_z\}$ for accreted star particles for each of the three MW-like galaxies m12f, m12i and m12m in FIRE-2 simulation. The color coding in Fig. 4.2 corresponds to the individual satellites that are identified by analyzing the snapshots from simulation data as described in Section 4.2 and is shown by the legend in the bottom row.

4.3.2 Finding Clusters with *Enlink*

We apply algorithm *Enlink* [93], a density-based hierarchical group finding algorithm capable of identifying structures of any shape and density in multi-dimensional datasets, to the action space variables $\{J_r, J_z, J_\phi\}$ for the 3 galaxies from FIRE-2. *Enlink* is especially useful for astrophysical data as it can effectively detect groups which are not globular. Here we summarize the basic principles behind *Enlink*. For more details see Ref. [93].

1. **Build a locally adaptive Mahalanobis (LAM) metric $\Sigma^{-1}(\mathbf{x})$.** The distance squared between two data points $\mathbf{x_i}$ and $\mathbf{x_j}$ is defined as:

$$s^2(\mathbf{x_i}, \mathbf{x_j}) = |\Sigma(\mathbf{x_i}, \mathbf{x_j})|^{\frac{1}{d}}(\mathbf{x_i} - \mathbf{x_j})^{\mathsf{T}}\Sigma^{-1}(\mathbf{x_i}, \mathbf{x_j})(\mathbf{x_i} - \mathbf{x_j}) \qquad (4.2)$$

where d is the dimension of data, $\Sigma^{-1}(\mathbf{x_i}, \mathbf{x_j}) = 0.5(\Sigma^{-1}(\mathbf{x_i}) + \Sigma^{-1}(\mathbf{x_j}))$. To build this LAM metric $\Sigma^{-1}(\mathbf{x})$, first divide the whole data set into regions with each region containing $(d+1)$ data points, and the particles in each region are distributed as uniformly as possible. Then calculate the local covariance matrix $\Sigma(\mathbf{x})$ of the data points in each region and smooth it so that this local matrix changes continuously and smoothly from region to region.

2. **Calculate a local density $D(x)$ for each data point.** For each data point, find k nearest neighbors to it based on distance squared defined in Eq. (4.2).
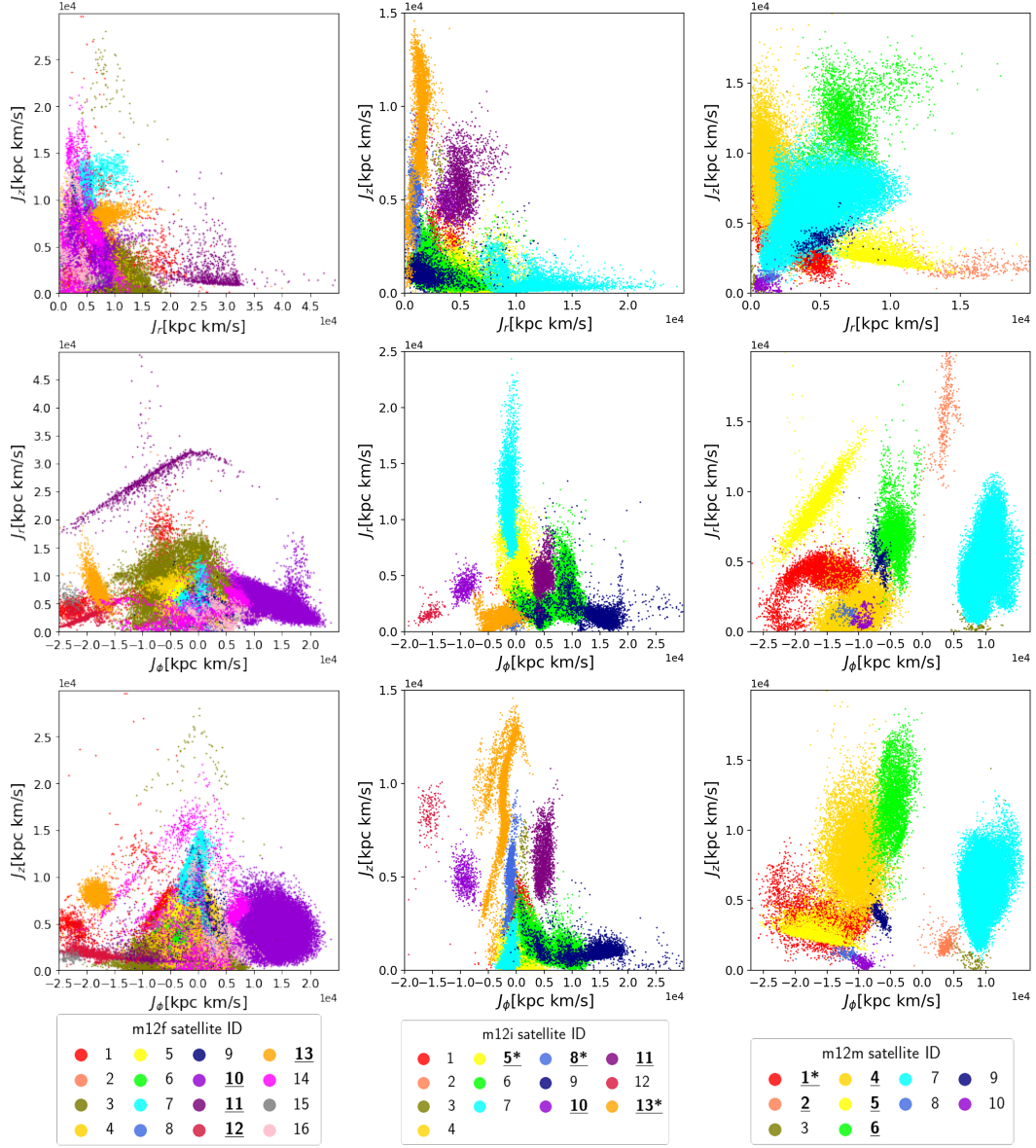
Figure 4.2: Two dimensional projections of actions $\{J_r, J_z, J_\phi\}$ for accreted star particles from 3 MW-like galaxies in FIRE-2 simulations. The three columns correspond to the three galaxies in FIRE-2 simulations: m12f, m12i and m12m, from left to right. Each accreted satellite identified from analyzing snapshots from the simulation is indicated by a different color. The meaning of bold and underlined IDs, and IDs with stars (*) is the same as that in Fig. 4.1.

79

The size of neighborhood k has a pre-defined default value in *Enlink* : $k = 10$.
We have tried $k = 5 - 20$, and the results are robust against the variation of k
in this range. Calculate density as:

$$D(\mathbf{x_j}) = \sum_{i=1}^{k} \frac{m_i}{h^d |\Sigma(\mathbf{x_j})|^{\frac{1}{2}}} W(\sqrt{(\mathbf{x_i} - \mathbf{x_j})^{\mathsf{T}} \Sigma^{-1}(\mathbf{x_j})(\mathbf{x_i} - \mathbf{x_j})}/h) \qquad (4.3)$$

where h is the smoothing length corresponding to a given k, d is the dimension-
ality of data space, W is a kernel function to normalize the integral of density
and m_i is the mass of each particle.

3. **Identify clusters based on density and preserve significant groups.** We
start building groups at local density peaks, and these groups grow by absorbing
nearby points. Once two groups try to absorb a common particle, a saddle point
is reached and the smaller group is absorbed into the bigger one as a subgroup
(the subgroup is not canceled and still treated as a separate group). After all
the (sub)groups are identified, the *significance S* of each group is calculated:

$$S = \frac{\ln(D_{\text{max}}) - \ln(D_{\text{min}})}{\sigma_{\ln(D)}} \qquad (4.4)$$

where D_{max} and D_{min} are maximum and minimum densities in that group.
$\sigma_{\ln(D)}$ is the standard deviation of log of densities in one group. *Significance*
measures how inhomogeneous a group is, and should not be confused with
statistical significance. We define the size of a satellite as the number of star
particles it contains. We denote the minimum size of satellites we tracked by
N_S. The minimum number of particles in a group, N_{min} , is chosen to be of the
same order of magnitude as N_S. Then any group with number of particles lower
than N_{min} would have its *significance* set to 0. For two intersecting groups, we
compare their values of *significance* to a pre-determined threshold S_{Th}. If both

groups have $S > S_{Th}$, then keep both of them. Otherwise, the one with lower S is eliminated and its particles are absorbed into the group with higher S.

As can be seen from the description above, four parameters determine the result of cluster finding: size of neighborhood k, threshold *significance* S_{Th}, mass of each particle m_i and minimum size of group N_{min}. In this work, we neglect the mass of star particles, so all the m_i is set to 1. Three other parameters have their default values pre-defined in the *Enlink* program. During our runs, k and S_{Th} are varied slightly around their default values and N_{min} is chosen to be in the same order of magnitude as the minimum size of satellites, so that the number of groups that the algorithm yields is close to the number of accreted satellites in a galaxy.

Groups that were identified by *Enlink* with $k = 10$, $N_{min}= 300$ and S_{Th} at its default value for the three galaxies from the FIRE-2 simulations are shown in Fig. 4.3. The minimum number of star particles in each of the satellites in the three galaxies is around 150 (corresponding to a minimum stellar mass of around $6.0 \times 10^5 \, M_\odot$), so a reasonable value for N_{min} would seem to be 150. With $N_{min}= 150$, many small random groups emerge in all three galaxies. With $N_{min}= 300$ the identification of large and clear satellites is not affected in m12f and m12m, but in m12i, a satellite with size 184 (located in action space at around $J_\phi = -12000\mathrm{kpc} \times \mathrm{km/s}$, $J_z = 8000\mathrm{kpc} \times \mathrm{km/s}$, $J_r = 2000\mathrm{kpc} \times \mathrm{km/s}$) cannot be identified. However, when $N_{min}= 150$, large coherent satellites are devided into several groups, which makes it harder to identify the large coherent satellites. Therefore, we keep $N_{min}= 300$, which corresponds to a minimum stellar mass of around $1.2 \times 10^6 \, M_\odot$ for groups found by *Enlink*.

In applications to observational data, since the sizes of datasets are expected to be much larger and the number of accreted satellites is completely unknown, these 4 parameters should be determined carefully. It is also likely that one satellite could be split into multiple groups by cluster analysis [250]. Adding additional information,

such as metallicity or abundances of specific elements [e.g. Ca, N, Fe, Eu, 290; 249] can help to confirm the identification of a satellite or identify subcomponents of a single satellite, but this is beyond the scope of this chapter. In this chapter, we are testing how well cluster analysis in the action space alone can perform under optimum conditions: perfect knowledge of all 6 phase space coordinates, accurate representation of the galactic potential, and prior insights into the optimum values of parameters like N_{min}. We also assume that this perfect data is available throughout the halo (out to the radius of the furthest particles) and that all members of a given satellite are detected and in the dataset. While these assumptions are not observationally justified, these assumptions allow us to assess how the hierarchical merger history of the galaxy affects our ability to recover accreted satellites. In a future paper we will repeat this exercise imposing observational errors and selection functions for *Gaia* and upcoming surveys with the Rubin Observatory and the Roman Space Telescope. These simplifying assumptions enable us to assess how well cluster analysis can perform in the best-case scenario.

4.3.3 Metrics to Assess Identification of Satellites by Clusters

In order to quantify the ability of *Enlink* to identify accreted satellites in action space, we define three matrices: R_{ij}, P_{ij} and M_{ij}; and four quantities based on these matrices: *recovery, purity, merit* and *contrast*. We refer to the clusters identified by *Enlink* as "groups". The number of star particles contained in a group is called the size of the group. In order to quantify the degree to which a group identified by *Enlink* matches one of the original accreted satellites we also define the "*best recovery group*" (similarly for *purity, merit*) and best fit group. Based on *recovery, purity, merit* and best fit group, we select out the "well-recovered satellites".

1. **Three matrices** R_{ij}, P_{ij}, M_{ij}**:** The ij component of these three matrices de-

scribes the similarity between satellite j and group i:

$$R_{ij} = \frac{\text{number of particles shared by satellite } j \text{ and group } i}{\text{number of particles in satellite } j},$$

$$P_{ij} = \frac{\text{number of particles shared by satellite } j \text{ and group } i}{\text{number of particles in group } i},$$

$$M_{ij} = R_{ij} \times P_{ij}$$

2. **Recovery, purity, merit:** For satellite k, the maximum values of R_{ik}, P_{ik} and M_{ik} are called the *recovery* (r_k), *purity* (p_k) and *merit* (m_k) of this satellite:

$$r_k = \max_i\{R_{ik}\}, \text{for } i \text{ in range of group indices}$$

$$p_k = \max_i\{P_{ik}\}, \text{for } i \text{ in range of group indices}$$

$$m_k = \max_i\{M_{ik}\}, \text{for } i \text{ in range of group indices}$$

3. **Best** *recovery, purity, merit* **group and best fit group:** For satellite k, the group which yields r_k is called the "best *recovery* group", and likewise p_k and m_k define the "best *purity* group" and "best *merit* group" of satellite k, respectively. If a group is both the "best *recovery* group" and the "best *purity* group" of satellite k, then it is defined as the "best fit group" of satellite k.

4. **Contrast**: To compare the size of satellite k and its best fit group, we define *contrast* (c_k) as:

$$c_k = \frac{r_k - p_k}{\sqrt{r_k p_k}} \tag{4.5}$$

where r_k and p_k are *recovery* and *purity* of satellite k. Note *contrast* is only defined for a satellite with a best fit group. When c_k is positive, satellite k is smaller than its best fit group (the group contains contaminants - i.e. stars that were not originally part of the satellite), and when c_k is negative, satellite k is larger than its best fit group (not all of the members of the satellite have been

identified as group members).

5. **Well-recovered satellite:** If the *recovery, purity* and *merit* of a satellite are all greater than 0.5 and this satellite has a best fit group, then this satellite is called *well-recovered* or is said to have a *high identifiability score.* A satellite that is not well-recovered is called poorly-recovered.

4.4   Results

We do a cluster analysis with *Enlink* on actions $\{J_r, J_z, J_\phi\}$ of accreted star particles from three MW-like galaxies in FIRE-2 simulations. In Section 4.4.1, we calculate the values of *recovery, purity, merit* and *contrast* for each satellite in three galaxies to evaluate how well these satellites are recovered by *Enlink*. We study the distribution of well-recovered satellites on the M_{tot}-T_{infall} plane and M_{stellar}-T_{infall} plane, and find the boundaries in M_{tot} M_{stellar} and T_{infall} values that separate well-recovered and poorly-recovered satellites by the classification tree method. We also investigate the relation between *significance* of a group and the identification power of this group (that is, whether this group corresponds to a well-recovered satellite or not). In Section 4.4.2, we include certain percentages of *in situ* stars into the input data set for cluster analysis. We pick out the well-recovered satellites which are identified when *in situ* star particles are absent. Calculate the values of *merit* of these satellites under different *in situ* star contamination ratios and demonstrate the robustness of the identification of these satellites under the contamination of *in situ* star particles.

4.4.1   Cluster Analysis on Accreted Star Particles

We apply *Enlink* to the actions $\{J_r, J_z, J_\phi\}$ for accreted star particles from the MW-like galaxies m12f, m12i and m12m in FIRE-2 simulations. In a manner similar to Fig. 4.2 three projections of the actions for accreted star particles $\{J_r, J_\phi, J_z\}$ are

Figure 4.3: Same as Fig. 4.2, but with substructures identified by *Enlink* to see how well *Enlink* can reproduce the actual satellites in the simulations as shown in Fig. 4.2. Particles from different groups identified by *Enlink* are indicated by different colors. Results plotted here are obtained from *Enlink* runs with size of neighborhood $k = 10$, minimum group size $N_{\min} = 300$ and *significance* threshold S_{Th} at its default value. .

shown in Figure 4.3, but now the color coding corresponds to the individual *groups* that are identified by *Enlink*. The legend in the bottom row now indicates the color coding for the individual groups identified. A comparison with Fig. 4.2 shows visually that while in m12i and m12m the number of groups identified is one larger than the number of satellites., in m12f only 15 groups (of 16 satellites) are identified. Overall however, there is an excellent correspondence between the groups identified by *Enlink* and the original satellites seen in Fig. 4.2.

Fig. 4.4 shows the values of *recovery, purity, merit* and *contrast* of 39 satellites in the three simulated galaxies m12f, m12i and m12m, on a M_{tot} vs. T_{infall} plot. Each symbol corresponds to one accreted satellite and symbols are color coded by the value of their *recovery* (panel a), *purity* (panel b), *merit* (panel c) and *contrast* (panel d), with red colored points indicating better results. In panels a, b, and c, satellites are also shape coded by whether their best *recovery* group match their best *purity* group (triangle) or not (circle) (in other words, whether the satellite has a best fit group (triangle) or not (circle)). White numbers indicate the group ID (as shown in Fig. 4.3) signifying best *recovery* (panel a), best *purity* (panel b), best *merit* (panel c) or best fit (panel d) for each satellite. A white letter associated with each data point indicates which galaxy this satellite is from: 'f' for 'm12f', 'i' for 'm12i' and 'm' for 'm12m'. Among the 39 satellites, 14 of them are "well-recovered" (their values of *recovery, purity* and *merit* are larger than 0.5 and they have best fit groups), while 25 of them are poorly-recovered. With T_{infall} and $\log_{10}(M_{\text{tot}}/\,\text{M}_\odot)$ as inputs, we grow a classification tree to predict whether a satellite is well-recovered or not. (For a brief introduction to classification tree method, see Appendix A.3) The boundaries that the classification tree finds out are: $T_{\text{infall}}= 7.1$ Gyr ago and $M_{\text{tot}}= 10^{8.6}\,\text{M}_\odot$, which are shown as vertical and horizontal blue dashed lines in Fig. 4.4. 91% (10/11) of the satellites in the region bounded by $M_{\text{tot}}> 4.0 \times 10^8\,\text{M}_\odot$ and $T_{\text{infall}}< 7.1$ Gyr ago are "well-recovered" satellites. Of the satellites outside this region, 86% of the sample

(24/28) are poorly-recovered. Three satellites in galaxy m12i (marked by 3i, 4i and 7i on the plot) fell into the host galaxy far more than 7.1 Gyr ago (T_{infall}= 9.08-10.33 Gyr ago), but are still well-recovered. This can be attributed to the unique dynamic history of galaxy m12i. See Section 4.5 for more discussion. Group 1 in each galaxy is the "best" group of many satellites, because Group 1 is the largest group and contains star particles from many "poorly-recovered" satellites. Group 1 in each of the galaxies can be considered as the "background" group. Panel d plots the *contrast* of satellites, shape coded by whether the *contrast* is positive (diamond) or negative (square). Only the satellites with a best fit group are plotted in panel d. Note that a positive *contrast* means that a satellite is smaller than its best fit group, and a negative *contrast* means the opposite. Most of the values of contrast are close to 0, with a few extremely large values (above 20). These extremely large values belong to satellites with Group 1 as best fit group, indicating that Group 1 is much larger than these satellites, consistent with the fact that Group 1 contains star particles from many satellites and is the background group. The values of contrast of "well-recovered" satellites are close to 0, meaning the number of particles in these satellites is similar to that in their best groups.

Similar to Fig. 4.4, in Fig. 4.5 we plot the values of *recovery, purity, merit* and *contrast* of 39 satellites in the three simulated galaxies m12f, m12i and m12m, on the M_{stellar} vs. T_{infall} plane. The color code, shape code and the meaning of the white numbers/letters are the same as those in Fig. 4.4. The boudaries separating well-recovered and poorly-recovered satellites found by the classification tree method in the M_{stellar} vs. T_{infall} plane are: $M_{\text{stellar}} = 1.2 \times 10^6\,M_\odot$ and T_{infall}= 7.1 Gyr ago, marked by the horizontal and vertical blue dashed lines in the four panels. The T_{infall} boundaries found in M_{tot} vs. T_{infall} and M_{stellar} vs. T_{infall} planes agree with each other. 91% (10/11) of the satellites with M_{stellar} greater than $1.2 \times 10^6\,M_\odot$ and fell into the halo less than 7.1 Gyr ago are well-recovered by *Enlink*.

For more plots showing values of recovery, purity, merit and contrast against infall time, total mass and stellar mass, see Appendix A.2. To see where the well-recovered satellites are located in position space, velocity space and action space, we mark the well-recovered satellites with bold and underlined IDs in the legends of Fig. 4.2, Fig. 4.1, Fig. A.1 and Fig. A.2. The well-recovered satellites outside the $M_{\text{tot}} > 4.0 \times 10^8 \, \text{M}_\odot$, $M_{\text{stellar}} > 1.2 \times 10^6 \, \text{M}_\odot$ and $T_{\text{infall}} < 7.1$ Gyr ago ranges are marked by bold and underlined IDs with a star (*) in those legends.

In Section 4.3.2, we find that 150 star particles are corresponding to $M_{\text{stellar}} \approx 6 \times 10^5 \, \text{M}_\odot$, so setting $N_{\text{min}} = 300$ is equivalent to setting the lower bound of M_{stellar} to be around $1.2 \times 10^6 \, \text{M}_\odot$ for groups found by *Enlink* . Any group with less stellar mass than $1.2 \times 10^6 \, \text{M}_\odot$ (number of particles smaller than $N_{\text{min}} = 300$) will not be found by *Enlink* under our choice of N_{min}. This lower bound in M_{stellar} agrees with the $M_{\text{stellar}} = 1.2 \times 10^6 \, \text{M}_\odot$ boundary for well-recovered satellites. This agreement raises a caveat that the boundary on M_{stellar} (probably also on M_{tot}) might be an artifact due to a particular choice of N_{min}.

To appreciate how well the boundaries $M_{\text{tot}} = 4.0 \times 10^8 \, \text{M}_\odot$, $M_{\text{stellar}} = 1.2 \times 10^6 \, \text{M}_\odot$ and $T_{\text{infall}} = 7.1$ Gyr ago work in separating out well-recovered satellites, we show three kernel density plots of 39 satellites from three galaxies in M_{tot}(left), M_{stellar} (middle) and T_{infall}(right) in Fig. 4.6. In all three panels, the dotted density curve represents well-recovered satellites, while the solid curve represents poorly-recovered satellites. The two curves are normalized separately. The vertical dashed lines in three panels show the boundaries in Fig. 4.4 and Fig. 4.5: $M_{\text{tot}} = 4.0 \times 10^8 \, \text{M}_\odot$, $M_{\text{stellar}} = 1.2 \times 10^6 \, \text{M}_\odot$ and $T_{\text{infall}} = 7.1$ Gyr ago. In the left panel, the dotted curve peaks at a higher M_{tot} than the solid curve, indicating that well-recovered satellites tend to be more massive. However, the peaks of both curves are greater than $4.0 \times 10^8 \, \text{M}_\odot$, indicating that the boundary in M_{tot} alone cannot distinguish between well-recovered and poorly-recovered satellites. In the middle panel, the solid curve peaks at a lower
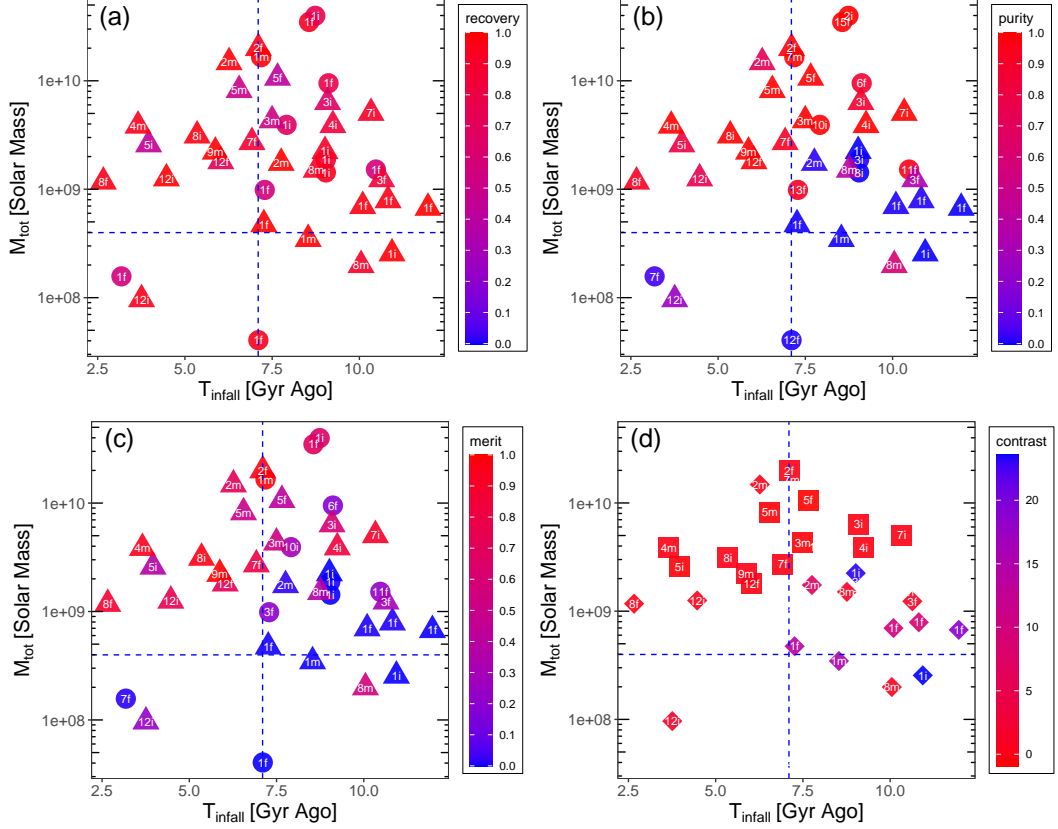
Figure 4.4: 39 satellites in 3 MW-like galaxies from the FIRE-2 simulations plotted on the M_{tot} vs. T_{infall} plane. Data points are color coded by the *recovery* (panel a), *purity* (panel b), *merit* (panel c) or *contrast* (panel d), with red points indicating better results in all panels. The white number on each symbol indicates the group ID (as shown in Fig. 4.3) of the "best *recovery*" (panel a), "best *purity*" (panel b), "best *merit*" (panel c) and "best fit" (panel d) group corresponding to each satellite. The white letters associated with each data point indicates which galaxy each satellite is from: "f" for "m12f", "i" for "m12i" and "m" for "m12m". Group 1 in all three galaxies is the "best" group of many satellites because it is the largest group, as shown in Fig. 4.3, and is generally considered as the "background". A satellite is marked as a triangle if it has a "best fit group" and as a circle otherwise. Satellites are from the analysis of simulation data in Section 4.2, and groups are identified by *Enlink*. In panel d, only satellites with best fit groups are plotted, and shapes indicate whether the *contrast* is positive (diamond) or negative (square). Among the 39 satellites, 14 of them are well-recovered and 25 of them are poorly-recovered. The vertical and horizontal dashed lines mark $M_{\mathrm{tot}} = 4.0 \times 10^8 \, \mathrm{M}_\odot$ and $T_{\mathrm{infall}} = 7.1$ Gyr ago, which are the boundaries identified by the classification tree method. 91% (10/11) of the satellites with M_{tot} greater than $4.0 \times 10^8 \, \mathrm{M}_\odot$ and fell into the halo less than 7.1 Gyr ago are well-recovered by *Enlink*.
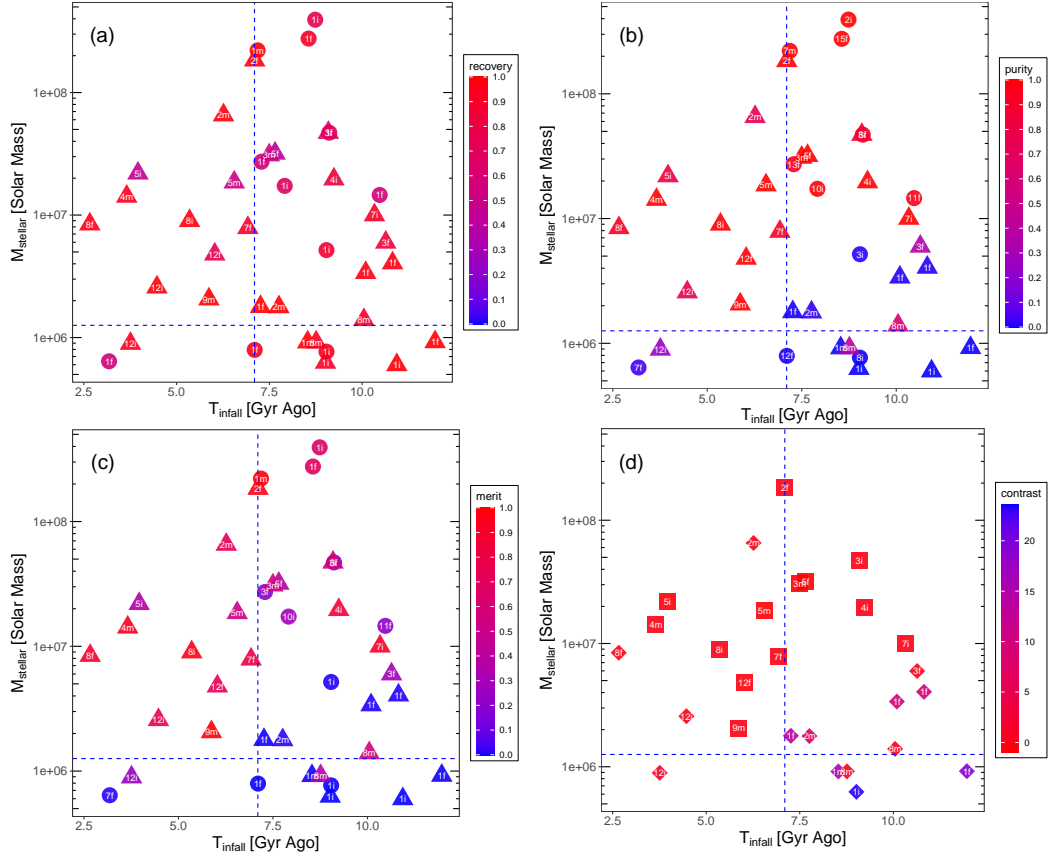
Figure 4.5: Same as Fig. 4.4, but the y axes of these plots are labeling M_{stellar}. The vertical and horizontal dashed lines mark $M_{\text{stellar}} = 1.2 \times 10^6 \, \text{M}_\odot$ and $T_{\text{infall}} = 7.1$ Gyr ago, which are the boundaries separating well-recovered and poorly-recovered satellites identified by the classification tree method. 91% (10/11) of the satellites with M_{stellar} greater than $1.2 \times 10^6 \, \text{M}_\odot$ and fell into the halo less than 7.1 Gyr ago are well-recovered by *Enlink*.
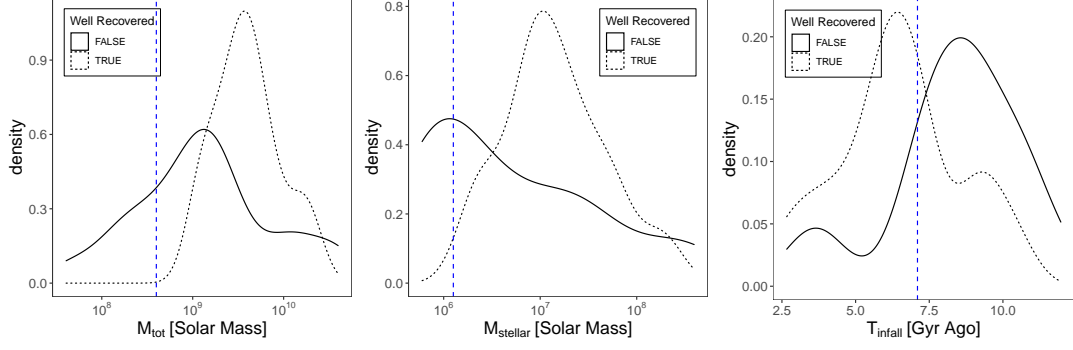
Figure 4.6: Kernel density plots of 39 satellites from three galaxies in M_{tot}(left), M_{stellar} (middle) and T_{infall} (right). The three blue vertical dashed lines label the boundaries in Fig. 4.4 and Fig. 4.5: $M_{\text{tot}} = 4.0 \times 10^8\,\text{M}_\odot$ (left), $M_{\text{stellar}} = 1.2 \times 10^6\,\text{M}_\odot$ (middle) and $T_{\text{infall}} = 7.1$ Gyr ago (right). In all three panels, the dotted density curve labels the well-recovered satellites, while the solid curve labels the poorly-recovered satellites. In the left panel, both the dotted and solid density curves peak above $M_{\text{tot}} = 4.0 \times 10^8\,\text{M}_\odot$, with the dotted curve peaking at a higher M_{tot}, indicating that well-recovered satellites tend to be more massive. In the middle panel, the dotted curve peaks at a higher M_{stellar}, indicating that well-recovered satellites tend to be have more stellar mass. In the right panel, the peaks of dotted and solid curves are on the two sides of $T_{\text{infall}} = 7.1$ Gyr ago

.

value than the dotted curve, indicating that well-recovered satellites tend to have more stellar mass than poorly-recovered ones. The peak of the solid curve is close to the $M_{\text{stellar}} = 1.2 \times 10^6\,\text{M}_\odot$ boundary, indicating that M_{stellar} alone cannot distinguish well-recovered satellites and poorly-recovered satellites either. In the right panel, the peaks of dotted and solid density curves are on the two sides of the T_{infall} boundary, justifying the boundary $T_{\text{infall}} = 7.1$ Gyr ago.

We have seen that massive satellites fell into MW-like galaxies relatively recently can be reliably recovered by cluster analysis in action space with *Enlink*. In future applications to observational data it will be necessary to use a statistical metric provided by *Enlink* to determine which groups are most likely to correspond to real satellites. The variable *significance*, assigned by *Enlink* to each group and calculated by Equation (4.4), is a good indicator of whether a group corresponds to a real satellite or not. In Fig. 4.7 we plot the values of *significance* of 34 non-background
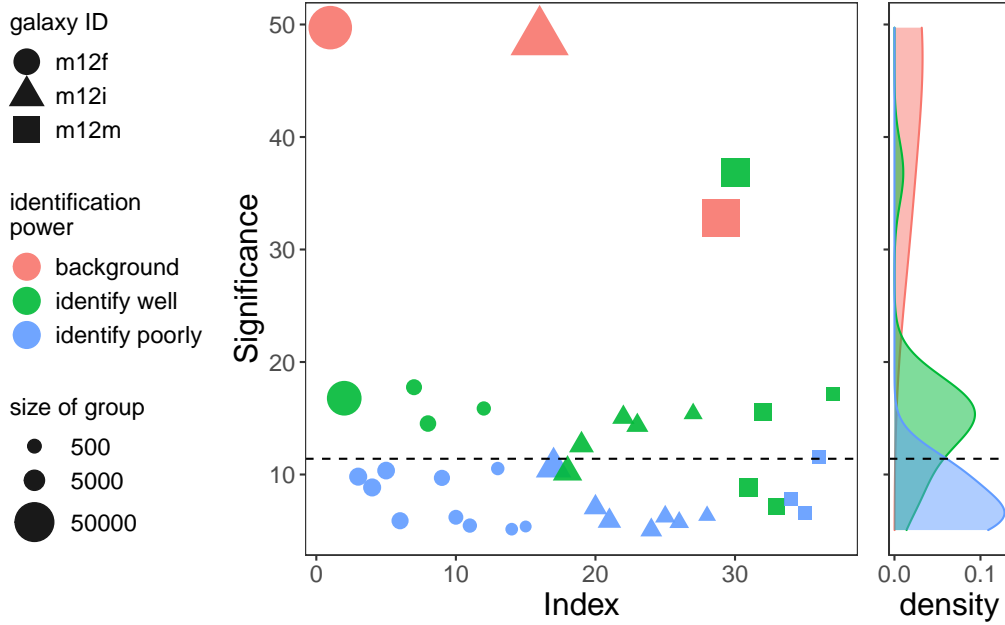
Figure 4.7: The values of *significance* of 37 (34 non-background+3 background) groups identified by *Enlink* in 3 MW-like galaxies (as shown in Fig. 4.3) are plotted. "Index" is a number between 1 and 37 to label each group. The size of a data point is proportional to the number of particles in the group. Groups from galaxies m12f, m12i and m12m are marked by circles, triangles and squares, respectively. The color of a data point indicates whether the groups is a background group (salmon), corresponds to a well-recovered satellite (green) or does not identify any satellite (blue). A kernel density plot is attached on the right hand side of the scatter plot. The black dashed line labeling the valley between green and blue curve peaks shows the cutoff in *significance* for groups corresponding to well-recovered satellites. The cutoff value in *significance* for groups corresponding to well-recovered satellites is 11.4, the 66th percentile of the *significance* of non-background groups.

groups and 3 background groups. The size of a data point is proportional to the number of particles in the group, while the shape shows which galaxy this group is from, and the color indicates whether the group is a background group (salmon), identifies a satellite well (green) or does not identify a single satellite (blue). A kernel density plot is attached on the side of the scatter plot. The green curve showing the distribution of *significance* peaks at a higher *significance* than the blue curve. The black dashed line shows the valley between the green and blue peaks. This valley, located at *significance* = 11.4 or the 66th percentile of the values of *significance* of the non-background population, is the cutoff in *significance* for groups corresponding to well-recovered satellites. Note the cutoff in *significance* here should not be confused with S_{Th} in Section 4.3.2. Among 12 non-background groups with *significance* above the cutoff, 11 of them are corresponding to "well-recovered" satellites. This result implies that with the results of *Enlink* cluster analysis in action space alone (i.e. no other information on satellites, and ignoring the largest group identified by *Enlink* assuming it to be "background"), *groups with higher significance than 66% of groups found by Enlink are very likely to be corresponding to true satellites.*

4.4.2   The Effect of *In-situ* Stars

Besides accreted stars, cosmological hydrodynamical simulations predict that *in situ* stars may also contribute to a significant part of the halo star population in a galactic halo. As mentioned earlier, the fraction of *in situ* halo stars is highly uncertain, but estimates in the MW [278; 279] suggest that it could be as small as 5% overall, while studies of resolved halo stellar populations in external galaxies find that the properties of these halo stars are consistent with being purely accreted [291] (beyond 30 kpc from the galactic center). Recent work [279] shows that in the MW halo, the relative fraction of *in situ* stars drops below 0.5 when $|Z_{\mathrm{gal}}| > 5\,\mathrm{kpc}$, where $|Z_{\mathrm{gal}}|$ is the distance from the disk plane. We also note that over 95% of the accreted

star particles in disrupted satellites in the three MW-like galaxies have $|Z_{\mathrm{gal}}| > 5\,\mathrm{kpc}$. We contaminate the data sets of accreted star particles with *in situ* star particles drawn from each of the three individual galaxies. The *in situ* star particles in the three simulated galaxies are selected by applying the following three filters: (i) the distance between the birth place of a star particle and center of host galaxy was required to be smaller than 30 kpc, (ii) the current distance of the star particle from the center of galaxy is smaller than 300 kpc, and (iii) the star particle's current $|Z_{\mathrm{gal}}| > 5\,\mathrm{kpc}$. Since our goal in this chapter is to understand how well action space clustering works with complete, error-free data we do not impose additional spatial cuts. This selection yields around 5×10^5 *in situ* star particles in each of the three FIRE-2 galaxies, while only 1×10^5 star particles in each galaxy are from disrupted accreted satellites. We show the distribution of *in situ* star particles in $\{J_r, J_z, J_\phi\}$ action space in Fig. 4.8 for each of the three galaxies. The fractions of *in situ* star particles in the simulated stellar halos (beyond $r \sim 30\mathrm{kpc}$ and $Z_{\mathrm{gal}} > 5\mathrm{kpc}$) are much higher than is observed in the Milky Way [278; 279]. Therefore to study the effects of *in situ* stars on the robustness of satellite identification by cluster analysis in the action space, we build numerous mock data sets with *in situ* contamination ratios equaling 0.1, 0.2, 0.3, 0.4 and 0.5 (where contamination ratio of 0.5 implies that 50% of the halo star sample consists of *in situ* stars) in three MW-like galaxies by randomly sampling the *in situ* star particles in the three galaxies from the FIRE-2 simulations with $|Z_{\mathrm{gal}}| > 5\,\mathrm{kpc}$. We then calculate the actions $\{J_r, J_z, J_\phi\}$ and do cluster analysis with *Enlink* in the action space on these "contaminated" data sets. We pick out the well-recovered satellites in Section 4.4.1 and study their values of *merit* at different contamination ratios. To reduce the effect of the randomness in sampling the *in situ* star particles, for every contamination ratio in each galaxy, we repeat the selection of the *in situ* "contaminant" population 100 times, randomly picking the same fraction of *in situ* stars each time. We then generate the value
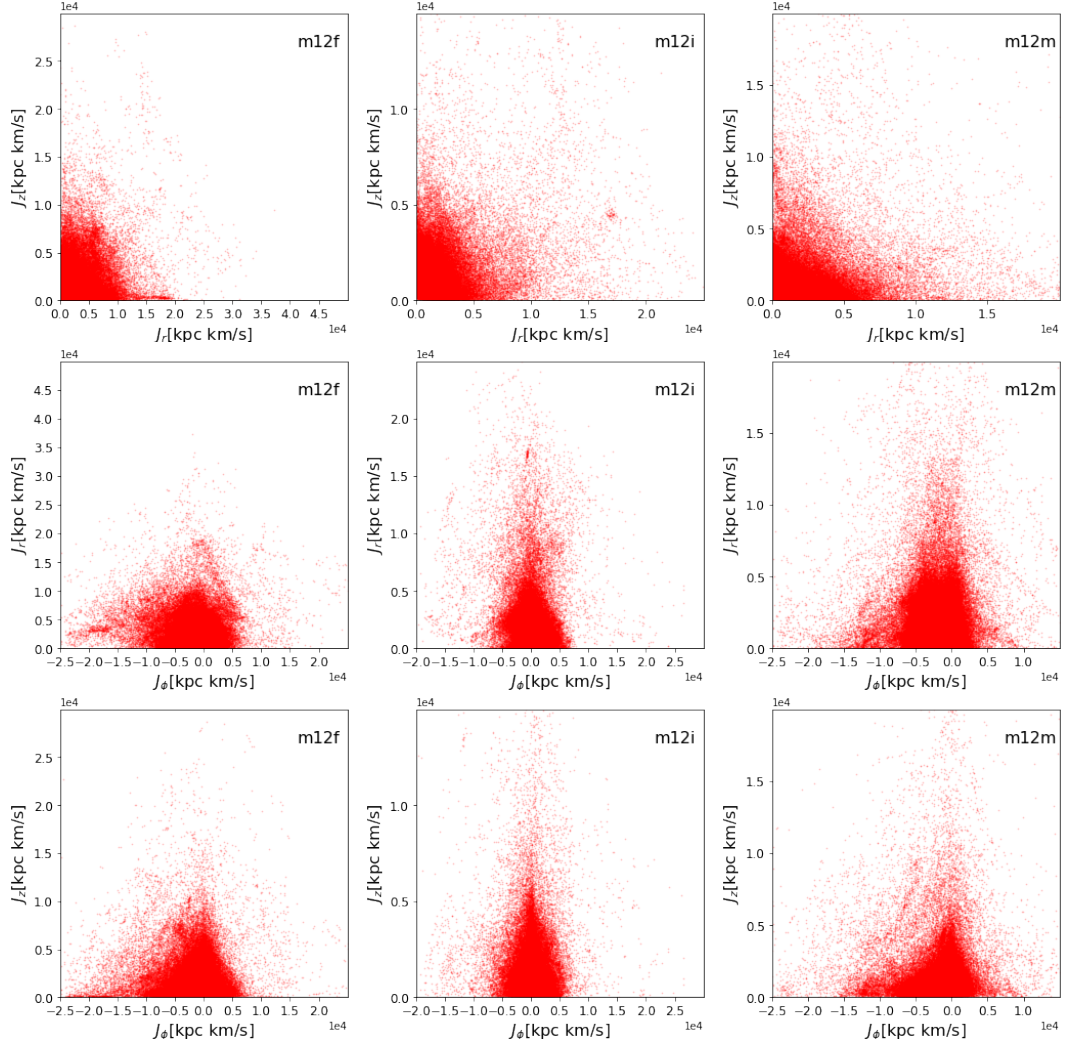
Figure 4.8: *In situ* star particles in each simulated galaxy analyzed in this research are plotted in $\{J_r, J_z, J_\phi\}$ action space. Each column is corresponding to one galaxy.

of *merit* for each well-recovered satellite from each data set. Each well-recovered satellite at a contamination ratio then has 100 values of *merit*. We calculate the average and standard deviation of those 100 values. If the previously well-recovered satellite doesn't have a best fit group in one data set (i.e., the best *recovery* group doesn't match with the best *purity* group), then the *merit* of that satellite in that run is set to 0.

Fig. 4.9 illustrates the change of values of *merit* of well-recovered satellites in three MW-like galaxies (as shown in Section 4.4.1) as the contamination ratio increases from
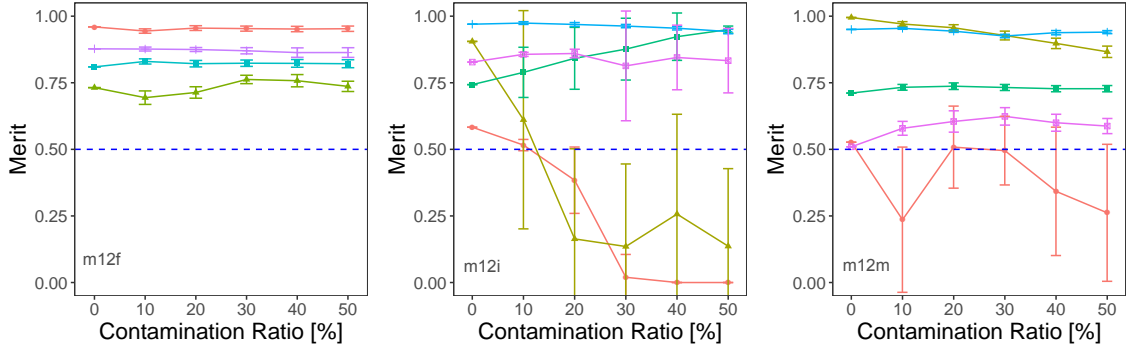
Figure 4.9: Values of *merit* of well-recovered satellites in three galaxies (m12f, m12i, m12m from left to right) at different *in situ* contamination ratios. Each differently colored line corresponds to one well-recovered satellite in each galaxy (the well-recovered satellites in three galaxies are summarized in Fig. 4.4). The values of merit come from the average of 100 runs and the error bars show the standard deviations. A blue dashed line in 3 panels shows *merit*=0.5, the threshold of "well-recovered" objects. 78% (11/14) of the well-recovered satellites have values of merit greater than 0.5 at all contamination ratios, being robust against the contamination from *in situ* star particles. As the contamination ratio increases, the values of *merit* of some satellites drop below 0.5. These "vulnerable" satellites have higher standard deviations in merit than other robust satellites, showing that they are more affected by the randomness of picking *in situ* star particles. The robustness of well-recovered satellites indicates that *Enlink* can recover most of the well-recovered satellites when *in situ* star particles are in the data set.

0 to 0.5. Each data point and error bar in the figure shows the average and standard deviation of results of 100 runs, respectively. Lines of different colors correspond to different well-recovered satellites. 78% (11/14) of the satellites are robust against the contamination from *in situ* star particles, as their values of *merit* are above 0.5 at all contamination ratios. Other satellites become unidentifiable by *Enlink* (*merit* < 0.5) as the contamination ratio increases. The standard deviation of the *merit* of these satellites are also higher than their more robust companions, showing that they are more vulnerable under the random draw of the *in situ* star particles.

4.5   Discussion and Conclusions

Inspired by the principle of conservation of orbital actions, we use cluster analysis in action space to find accreted satellites with accreted star particles in three MW like galaxies in the FIRE-2 cosmological hydrodynamical simulations. We summarize the main findings of our work below:

1. **Classification tree method finds the boundaries separating well-recovered and poorly-recovered satellites to be $T_{\text{infall}}=$ 7.1 Gyr ago and $M_{\text{tot}}=$ $4.0 \times 10^8\,\text{M}_\odot$ (or $M_{\text{stellar}} = 1.2 \times 10^6\,\text{M}_\odot$) (see Fig. 4.4 and Fig. 4.5).** We note however, that the boundary in M_{stellar} coincides with the minimum mass of groups that *Enlink* is set up to identify, determined by N_{min}. This coincidence implies that the mass boundary could be an artifact of the choice of N_{min}. The three galaxies have slightly different infall time and mass boundaries for reliable detection. For example, galaxy m12i has 3 well-recovered satellites which fell into the hosting halo more than 7.1 Gyr ago. This difference could be due to the distinct dynamical/evolutionary histories of the galaxies. Fig. 4.10 shows the offset angle, $\Delta\theta$, between the angular momentum vector of the disk at a given look-back time and the present time ($z = 0$) as a function of look-back

time for each of the three galaxies analyzed in this chapter. The disk stars at each look-back time are defined as star particles that are within 30 kpc and also have formation distance within 30 kpc from the center of the host galaxy. The graph shows that the direction of the angular momentum vector often changes suddenly and through large angles (presumably due to merger events) for look back time > 8 Gyr ago. Ref. [292] shows that many of the changes in this $\Delta\theta$ correlate with major gas-rich mergers. In particular, galaxies m12f and m12m experienced numerous chaotic changes in $\Delta\theta$ until 8 Gyr ago, after which $\Delta\theta$ changed much more slowly and steadily. The slow change in $\Delta\theta$ implies the gravitational potentials of these two galaxies have changed adiabatically over the last 8 Gyrs, and therefore orbital actions of particles should be reasonably well conserved. The conservation of orbital actions implies that satellites accreted less than 8 Gyr ago should be found clustered in action space at $z = 0$. This "8 Gyr ago" time limit for finding satellites clustered in action space is in agreement with the time boundary for good recovery that we found in Section 4.4. $\Delta\theta$ of galaxy m12i changes more smoothly compared with the other 2 galaxies, so it is expected that satellites accreted a long time ago would remain clustered in action space. This is in agreement with the fact that three satellites in this galaxy with $T_{\mathrm{infall}} > 9$ Gyr ago are still well-recovered by *Enlink*. In our Milky Way galaxy, *Gaia* Enceladus, which has $T_{\mathrm{infall}} \approx 10$ Gyr ago and progenitor stellar mass $6 \times 10^8 \, \mathrm{M}_\odot$ [245], can still be recovered in phase space. The recovery of this massive substructure which fell into the Milky Way a long time ago indicates that the Milky Way might evolve smoothly from relatively early on, like m12i in the FIRE-2 simulations.

2. **The value of** *significance* **of a group shows a high correlation with the identification power of this group (see Fig. 4.7).** Of the groups with high *significance* (>11.4, 66th percentile of the *significance* of non-background

98

groups in three galaxies), most (92%, 11/12) correspond to the well-recovered satellites. This implies that if cluster analysis in action space is applied to observational data, this *significance* assigned by *Enlink* can help us determine which groups are most likely to correspond to true accreted satellites.

3. **Most of the well-recovered satellites are robust against contamination of** *in situ* **star particles (see Fig. 4.9).** 78% (11/14) of the well-recovered satellites in Section 4.4.1 stay well-recovered (with *merit* > 0.5) at 5 different contamination ratios (0.1, 0.2, 0.3, 0.4 and 0.5), where contamination ratio is the percentage of *in situ* star particles in the data set of one galaxy. The satellites which fail to be identified by *Enlink* in the presence of contamination have higher standard deviations in *merit*, indicating that they are more sensitive to the randomness in picking *in situ* stars. This robustness against contamination from *in situ* star particles indicates that it will be possible to apply cluster analysis in action space to observation data, even if there is significant contamination from *in situ* stars. This is reassuring since the expected fraction of *in situ* stars in the MW (5%) is at the low end of the contamination fractions we have experimented with.

In this work we have demonstrated, using simulation data, that it is possible to find accreted satellites using cluster analysis in action space. We have deliberately focused on a fairly idealized set of circumstances: (a) we assumed that phase space coordinates of all star particles were known with no error; (b) we assumed nearly perfect knowledge of the gravitational potential arising from stars, dark matter and gas (although we approximated the potentials as axisymmetric even though they are triaxial); (c) we had perfect knowlegde of the merger history of the galaxies and therefore the true masses and infall times of the satellites. In future applications of this method to observational data, the following improvements should be explored.

99
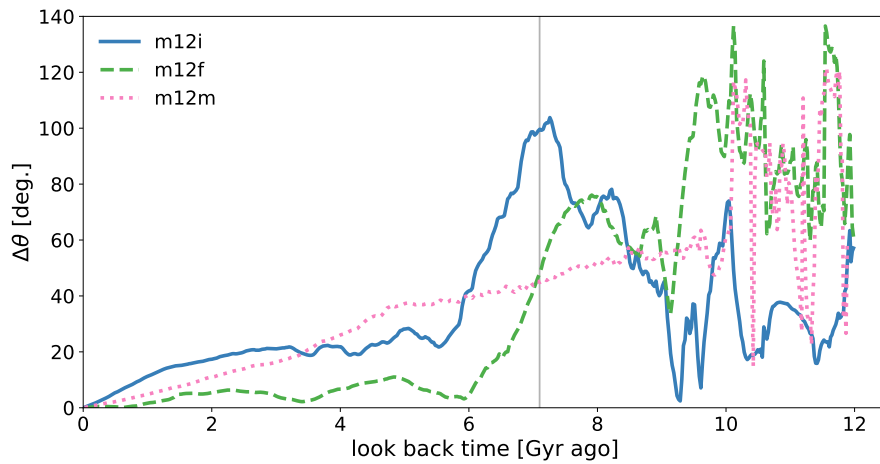
Figure 4.10: The dynamical histories of the 3 MW-like simulated galaxies in FIRE-2. The angle $\Delta\theta$ of the normal vector of the galaxy disk relative to its present-day direction is plotted versus lookback time. If $\Delta\theta$ changes rapidly, then the evolution of the galaxy is chaotic; if $\Delta\theta$ changes slowly, then the galaxy evolves smoothly. The disk orientations of galaxies m12f and m12m changed rapidly at the beginning and evolved more smoothly after 8 Gyr ago. Galaxy m12i evolved more smoothly than the other two galaxies before 8 Gyr ago, allowing massive satellites that fell into m12i up to 10.3 Gyr ago to remain clustered in action space at $z = 0$. A vertical line shows the time boundary for well-recovered satellites-7.1 Gyr ago.

1. As with all cosmological-hydrodynamical simulations, despite being until very recently the highest-resolution such simulations ever conducted of MW-mass halos [293], resolution limits our results to accreted structures at the stellar mass of classical dwarf galaxies and higher, since each star particle in the FIRE-2 simulations is 7100 $M_\odot$. The total number of accreted star particles used in our analysis is also orders of magnitude smaller than the number of accreted stars with 6D phase space coordinates (from *Gaia* and future large ground based surveys such as 4MOST [294], WEAVE [295], DESI [296; 297], which are expected to yield 6 phase space coordinates for 3–4 million stars. The performance of our clustering technique when scaled up by 3–4 orders of magnitude in particle number has yet to be tested. On the other hand, if we restrict ourselves to, e.g., RR Lyrae variables, then the conversion rate between the real data set and the simulation data set is about one star per star particle, and the analysis in this work can be more easily done. In addition, real data have observational errors and for this study we have assumed that all phase space coordinates are known perfectly. Additional studies with more realistic mock datasets like the `ananke` data set [286] are needed to assess how well *Enlink* performs under realistic conditions. Currently the precise 6D kinematics data are available only for stars within tens of kpc from the solar system, but the amount and precision of data for distant stars will increase significantly in the future. We are preparing another paper discussing the effects of errors from current and future observations, e.g. *Gaia* DR5, the Rubin observatory's Legacy Survey of and Space and Time (LSST) and Roman Space Telescope's High Latitude survey, on the cluster analysis in action space results.

2. It is necessary to find an objective way to determine $N_{\min}$, the parameter used by *Enlink* to determine a "reasonable" size for a cluster (Section 4.3.2). In this study $N_{\min}$ was selected by trial and error in order to ensure that the number

of groups that *Enlink* produced was close to the number of satellites that were known to have been accreted (as described in Section 4.2). An objective way to determine N_{min} and the other parameters that are used in the *Enlink* cluster analysis algorithm, is needed to evaluate the quality of clusters found. We found that the conventional silhouette plots [298] are not useful here, since many satellites are irregularly shaped in the action space and could be incorrectly classified by silhouette values. The choice of parameters for cluster analysis has been largely ignored in previous papers, and should be investigated in future.

3. Stellar metallicities and the abundance of individual elements in a star are also well conserved quantities that contain a substantial amount of information about the host satellite in which the star was born. However the stars in a satellite can have a range of [Fe/H] and α-element abundance ratios as well as gradients in the abundances of other elements. Ref. [290] show that including the abundance of certain elements (e.g. N, Ca) can improve the recovery of the Galactic mass model built through cluster analysis. Incorporating metallicities of stars as features into cluster analysis might improve the performance of current results from cluster analysis in action space.

4. The inclusion of metallicities of stars can also help to determine the masses of individual satellites (through the mass-metallicity relationship) and hence action-space clustering can be used to determine the number of accreted satellites per unit mass $N(M)$, a parameter that is a sensitive probe of the model of dark matter.

5. We have assumed in this work that the overall gravitational potential of each galaxy is axisymmetric rather than triaxial. This restriction was driven by the fact that the most efficient action finders available (e.g. AGAMA) are restricted to oblate axisymmetric potentials. Triaxial action finders [299; 300]

exist but are currently not fast enough to be useful for analysis of large datasets.
Development of fast triaxial action finders would be extremely helpful.

CHAPTER V

Summary and Conclusions

In this thesis, we have presented investigations of three different topics in the world of dark matter: direct detection, Dark Stars, and galactic archaeology.

First, we have quantified the combined effects of uncertainties in three astrophysical parameters — local circular velocity (v_0), local escape velocity (v_{esc}) and local dark matter density (ρ_χ)— on XENON1T exclusion limits. We have found that the effects from astrophysical uncertainties on exclusion limits are significant at low dark matter particle mass, and can cause a variation in σ_{SI} of six orders of magnitude at $m_\chi = 6\,\text{GeV}$. By comparing the effects from varying three parameters (v_0, v_{esc} and ρ_χ) with those from varying two parameters (v_0 and v_{esc}), we study the contribution of different parameters on the variation in the exclusion limit. Above 6 GeV, the variation in the exclusion limit is dominated by the uncertainties in local dark matter density, while below 6 GeV the uncertainties from escape velocity dominate.

Second, we have demonstrated the possibility of Dark Stars with self-interacting dark matter (SIDM), built the first model of SIDM Dark Stars, and investigated its properties. We have obtained the viable region in phase space that enables a particle physics model of SIDM to allow Dark Stars. All the requirements for Dark Stars— high enough density to produce heating, annihilation products trapped in the star and evading all the observational constraints— are satisfied by this model with proper

choices of parameters. The properties of the SIDM Dark Stars are shown to be similar to those of the corresponding WIMP Dark Stars with the same mass, luminosity and dark matter particle mass.

Finally, in order to find merged substructures, we apply the clustering algorithm *Enlink*, which works with quantities in action space, to accreted stars from FIRE-2 simulation data. Satellites accreted relatively recently, with $T_{\mathrm{infall}} < 7.1$ Gyr, and with high total mass or stellar mass at infall time ($M_{\mathrm{tot}} > 4.0 \times 10^8 M_\odot$ or $M_{\mathrm{stellar}} > 1.2 \times 10^6 M_\odot$) can be recovered with *Enlink* algorithm. Without the information about real satellites, groups with high values of a suitably defined quantity called *significance* are more likely to be true merged satellites. Most of the well-recovered satellites stay well-recovered under the contamination of *in situ* star particles. This method may be applied to observational data from future surveys to find more accreted satellite galaxies in the Milky Way, and help build the mass function of dark matter (sub)halos.

Several relevant topics in these three directions can be further explored in the future. For astrophysical uncertainties, the method demonstrated in Chapter II can be applied to analyze the recently released first results of the LZ experiment [59]. The local escape velocity is measured to be $v_{esc} = 445^{+25}_{-8}$ km/s (or $v_{esc} = 472^{+11}_{-12}$ km/s depending on different fitting methods) [301] by fitting the *Gaia* EDR3 data, and taking the effects of Gaia Sausage (Enceladus) into consideration. The recently measured values of escape velocity are smaller than the values used in Chapter II. Adopting them can cause the exclusion limits to be weaker towards higher cross section due to a lower cut-off speed in Equation 2.1. The lower uncertainties in the escape velocity can also translate into lower uncertainties in the exclusion curves studied in Chapter II.

Regarding the Dark Stars powered by SIDM, a detailed simulation with high resolution of the evolution of a $10^7 M_\odot$ SIDM minihalo should be carried out. In this simulation, the effects of a gas cloud should also be considered to verify or refute the gravothermal evolution proposed in Chapter III. The growth of SIDM Dark Stars

through the accretion of gas and SIDM particles is another interesting topic worth exploring. A more detailed stellar model for SIDM Dark Stars can also be built with stellar evolution code like MESA. Specifically, in the stellar evolution code, a new heating source from SIDM should be implemented. The spatial distribution of heating sources is expected to follow a cored dark matter density profile in an SIDM Dark Star, as shown in Fig. 3.4.

Finally, there are promising potential applications of the clustering analysis in Chapter IV to observational data. However, the uncertainties of the measurements in position and velocity should be reduced first. The importance of the precise measurements of position and motion is illustrated in Fig. 5.1. This figure shows the comparison of merged substructures in action space in m12i from FIRE-2 simulations for different error levels in the distance and proper motion measurements. The proper motion errors for stars in the Milky Way from the Nancy Roman telescope and from *Gaia* are taken from Ref. [302]. Star particles from the same substructure are plotted in the same color. The first row corresponds to the original substructures with no errors. In the second row we plot the substructures under 10% error in distance $+$ 6 μas yr^{-1} proper motion error accessible from Nancy Roman telescope. The substructures with 20% distance error $+$ *Gaia* proper motion error are plotted in the third row, where the *Gaia* proper motion error is an increasing function of the heliocentric distance. The substructures in the second row are still clustered in action space, although the edges start to become smeared. In the third row, however, the merged satellites are so smeared that no clear clusters can be identified. This comparison shows the importance of precise distance and proper motion measurements in the identification of substructures.
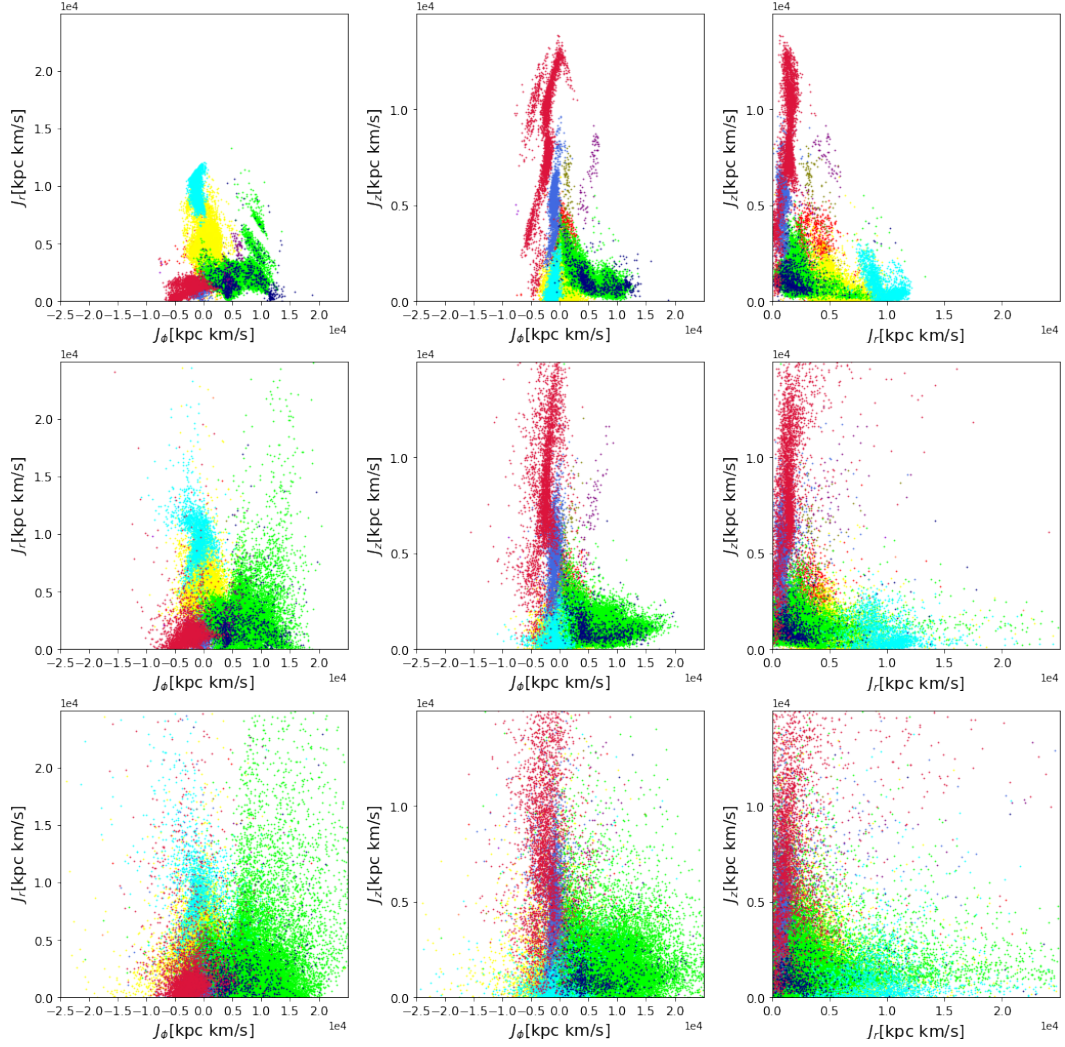
Figure 5.1: Comparison of the accreted substructures plotted in action space in m12i galaxy of FIRE-2 simulations. Different colors are corresponding to different substructures. The original substructures with no errors in distance and proper motion implemented are in the first row. The second row shows the substructures with 10% distance error + 6 μas yr^{-1} proper motion error accessible from Nancy Roman telescope. The substructures under 20% distance error + proper motion error from *Gaia* are plotted in the third row. From the first to the third row, the substructures become less and less clustered in action space.

APPENDIX

APPENDIX A

Appendix of Chapter 4

A.1   Satellite Distributions in Position and Phase Space

The disrupted satellites in galaxies m12i and m12m in position space (left column), velocity space (middle column) and r vs. v_r phase space (right column) are shown in Fig. A.1 and Fig. A.2, respectively.

A.2   Recovery, Purity, Merit and Contrast as Functions of Infall Time, Total Mass and Stellar Mass

The values of recovery, purity, merit and contrast of 39 disrupted satellites in three MW-like galaxies from the FIRE-2 simulations are plotted against infall time (first row), total mass (second row) and stellar mass (third row) in Fig. A.3. Well-recovered satellites are marked as triangles and poorly-recovered satellites are marked as circles. Blue dashed lines show the boundaries obtained in Section 4.4.1: $T_{\text{infall}} = 7.1$ Gyr ago, $M_{\text{tot}} = 4.0 \times 10^8$ M$_\odot$ and $M_{\text{stellar}} = 1.2 \times 10^6$ M$_\odot$.
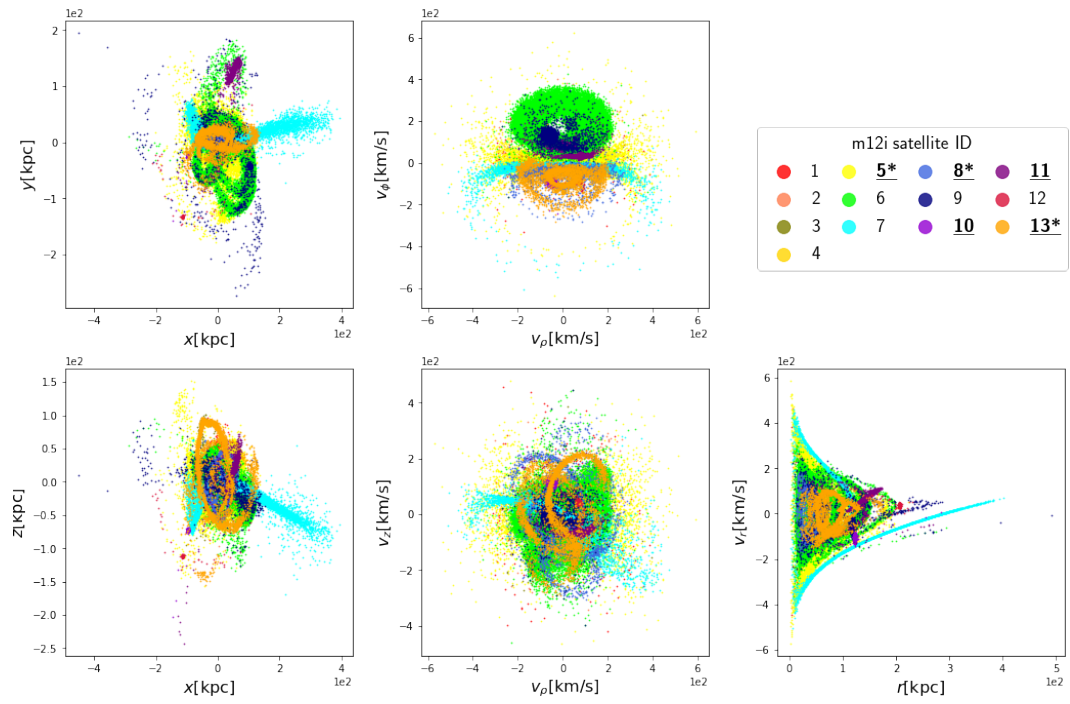
Figure A.1: Same as Fig. 4.1, but with satellites from galaxy m12i.
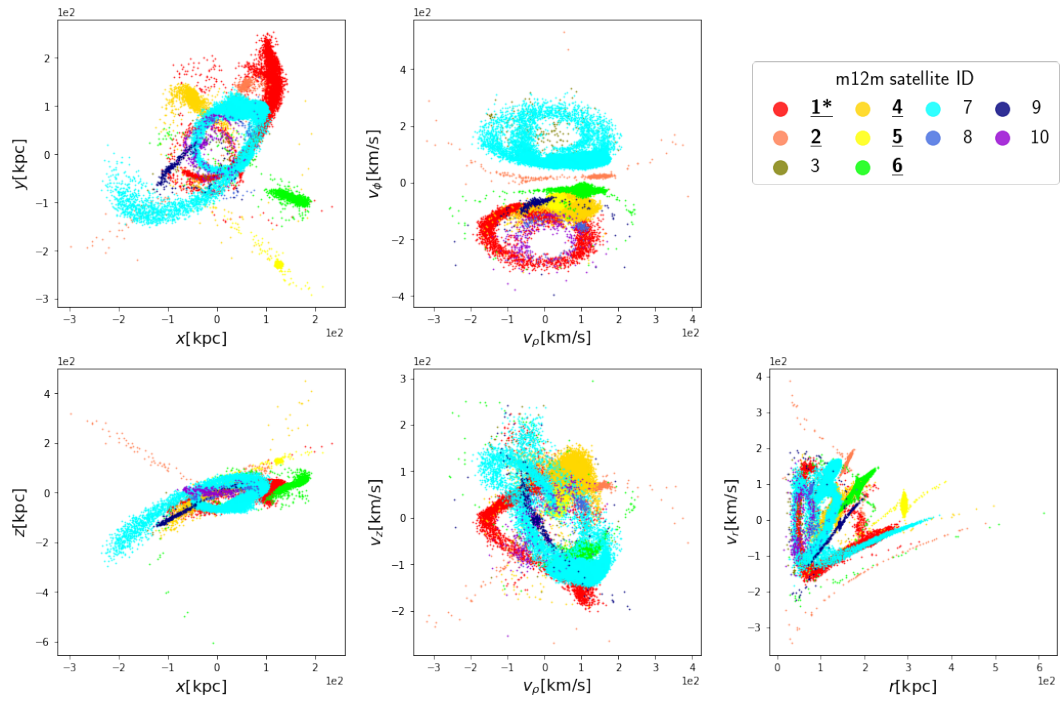
Figure A.2: Same as Fig. 4.1, but with satellites from galaxy m12m.
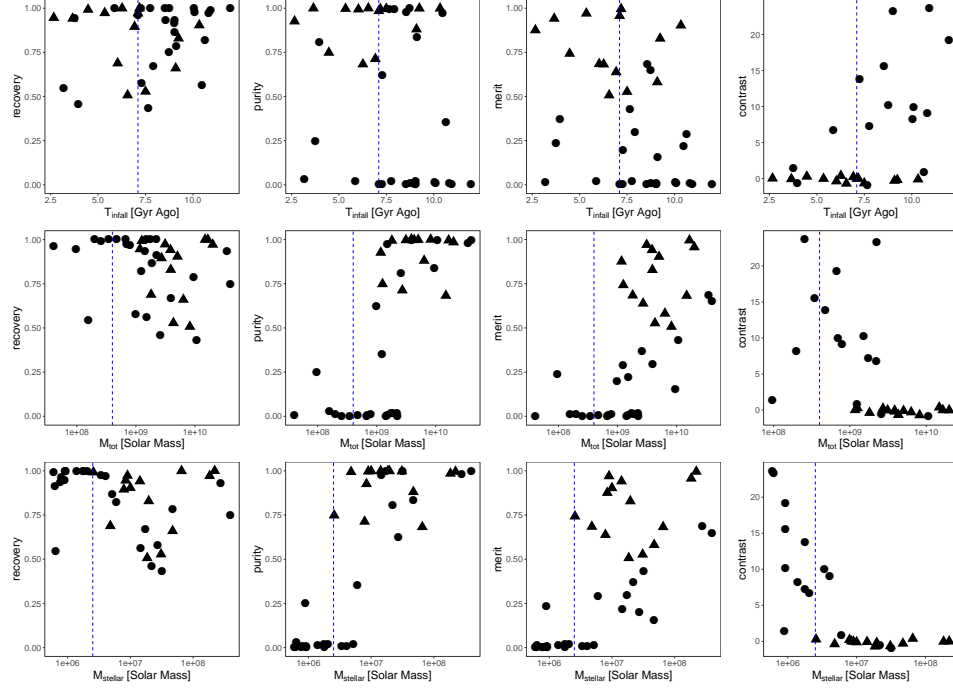
Figure A.3: The values of recovery, purity, merit and contrast of 39 disrupted satellites in three MW-like galaxies from the FIRE-2 simulations are plotted as functions of infall time (first row), total mass (second row) and stellar mass (third row). Well-recovered satellites are marked as triangles and poorly-recovered satellites are marked as circles. Blue dashed lines show the boundaries obtained in Section 4.4.1: $T_{\text{infall}}=$ 7.1 Gyr ago, $M_{\text{tot}}= 4.0 \times 10^8\,\text{M}_\odot$ and $M_{\text{stellar}} = 1.2 \times 10^6\,\text{M}_\odot$. In contrast plots, only satellites with best fit groups are plotted.

A.3 Classification Tree Method

We use a binary classification tree [303] to objectively determine the boundaries between well-recovered and poorly-recovered satellites in the T_{infall} - M_{tot} space and T_{infall} -M_{stellar} space. A classification tree tries to divide the multi-dimensional space covered by the input data into a series of regions, so that the data points inside each region are as pure (having the same label) as possible. To grow such a classification tree, we do several binary splits based on whether a feature is greater than or equal to ($\geq$) or smaller than ($<$) the split value. The rectangular region before a split is called a parent node, while the two sub-regions resulting from the binary split are called the children nodes. If a node has no children nodes, then it is called a leaf node. The impurity of a node indicates how diverse the labels of data points in a node are, and can be measured by cross-entropy, Gini-index or misclassification error. For details on these scales of impurity, see Ref. [304]. For one parent node with N_{parent} data points and two children nodes with N_{left} and N_{right} data points resulting from a split at one feature $f_i = x$, calculate the quality of split $Q(f_i, x)$:

$$
\begin{aligned}
Q(f_i, x) = {} & \text{Impurity(parent node)} \\
& - \frac{N_{\text{left}}}{N_{\text{parent}}} \text{Impurity(left child)} \\
& - \frac{N_{\text{right}}}{N_{\text{parent}}} \text{Impurity(right child)}
\end{aligned} \tag{A.1}
$$

The feature f_i and value x that maximize $Q(f_i, x)$ are the split feature and split value of a binary split. A tree can be grown by adding binary splits in this way until each terminal node is pure and cannot be further split. We then prune the tree by giving a penalty proportional to the size of the tree, until a balance between accuracy and size of tree is reached. Fig. A.4 shows the diagram of tree generated from $\log_{10}(M_{\text{tot}}/\,\mathrm{M_\odot})$ and T_{infall} in Gyr ago as input data. In each leaf node, a "well" or "poorly" indicates
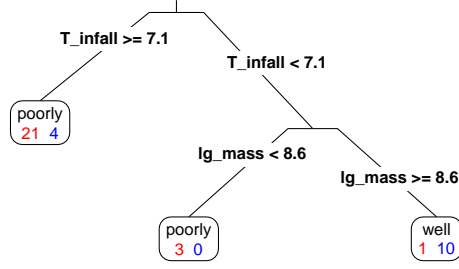
Figure A.4: A classification tree used in Section 4.4.1 to derive the boundaries between well-recovered and poorly-recovered satellites. "T_infall" indicates T_{infall} in Gyr ago, "lg_mass" represents $\log_{10}(M_{\text{tot}}/M_\odot)$. A "well" or "poorly" in each leaf node indicates the prediction of the label of data points in this node by majority vote, with "well" corresponding to well-recovered and "poorly" corresponding to poorly-recovered. The red and blue numbers in each leaf node indicate the numbers of poorly-recovered and well-recovered satellites in this leaf node, respectively. The tree with $\log_{10}(M_{\text{stellar}}/M_\odot)$ and T_{infall} in Gyr ago as input is similar, except that the split in $\log_{10}(M_{\text{stellar}}/M_\odot)$ is located at 6.1.

the prediction on the label of this node by majority vote. A red number in each leaf node is the number of satellites that are not well-recovered in this node, while the blue number corresponds to the number of well-recovered satellites in this node. The tree with $\log_{10}(M_{\text{stellar}}/M_\odot)$ and T_{infall} in Gyr ago as input is similar to the tree in Fig. A.4, except that the split in $\log_{10}(M_{\text{stellar}}/M_\odot)$ locates at 6.1.

BIBLIOGRAPHY

BIBLIOGRAPHY

[1] T.S. van Albada, J.N. Bahcall, K. Begeman and R. Sancisi, *Distribution of dark matter in the spiral galaxy NGC 3198.*, *ApJ* **295** (1985) 305.

[2] Planck Collaboration, P.A.R. Ade, N. Aghanim, M. Arnaud, M. Ashdown, J. Aumont et al., *Planck 2015 results. XIII. Cosmological parameters*, *A&A* **594** (2016) A13 [1502.01589].

[3] W. Hu and S. Dodelson, *Cosmic Microwave Background Anisotropies*, *Ann. Rev. Astron. Astrophys.* **40** (2002) 171 [astro-ph/0110414].

[4] J. Billard, M. Boulay, S. Cebrián, L. Covi, G. Fiorillo, A. Green et al., *Direct detection of dark matter-APPEC committee report*, *Reports on Progress in Physics* **85** (2022) 056201 [2104.07634].

[5] Gaia Collaboration, A.G.A. Brown, A. Vallenari, T. Prusti, J.H.J. de Bruijne, C. Babusiaux et al., *Gaia Data Release 2. Summary of the contents and survey properties*, *A&A* **616** (2018) A1 [1804.09365].

[6] A. Helmi, *Streams, Substructures, and the Early History of the Milky Way*, *ARA&A* **58** (2020) 205 [2002.04340].

[7] X. collaboration, *First dark matter search results from the xenon1t experiment,*, *Phys. Rev. Lett.* **119** (2017) 181301.

[8] T.P. et al., *The rave survey: the galactic escape speed and the mass of the milky way,*, *Astron. Astrophys.* **562** (2014) A91.

[9] W.-X. Feng, H.-B. Yu and Y.-M. Zhong, *Seeding Supermassive Black Holes with Self-interacting Dark Matter: A Unified Scenario with Baryons*, *ApJLett.* **914** (2021) L26 [2010.15132].

[10] J.H. Wise, M.J. Turk and T. Abel, *Resolving the Formation of Protogalaxies. II. Central Gravitational Collapse*, *ApJ* **682** (2008) 745 [0710.1678].

[11] PARTICLE DATA GROUP collaboration, *Review of Particle Physics*, *PTEP* **2022** (2022) 083C01.

[12] G. Bertone and D. Hooper, *History of dark matter*, *Reviews of Modern Physics* **90** (2018) 045002 [1605.04909].

[13] F. Zwicky, *On the Masses of Nebulae and of Clusters of Nebulae*, *ApJ* **86** (1937) 217.

[14] H.J. Rood, *The Dynamics of the Coma Cluster of Galaxies.*, Ph.D. thesis, University of Michigan, Jan., 1965.

[15] S.D.M. White, *Mass segregation and missing mass in the Coma cluster.*, *MNRAS* **179** (1977) 33.

[16] J.F. Meekins, G. Fritz, T.A. Chubb and H. Friedman, *Physical Sciences: X-rays from the Coma Cluster of Galaxies*, *Nature* **231** (1971) 107.

[17] S. Van den Bergh, *Collapsed Objects in Clusters of Galaxies*, *Nature* **224** (1969) 891.

[18] J. Tarter and J. Silk, *Current Constraints on Hidden Mass in the Coma Cluster*, *QJRAS* **15** (1974) 122.

[19] D.H. Rogstad and G.S. Shostak, *Gross Properties of Five Scd Galaxies as Determined from 21-CENTIMETER Observations*, *ApJ* **176** (1972) 315.

[20] R.N. Whitehurst and M.S. Roberts, *High-Velocity Neutral Hydrogen in the Central Region of the Andromeda Galaxy*, *ApJ* **175** (1972) 347.

[21] M.S. Roberts and A.H. Rots, *Comparison of Rotation Curves of Different Galaxy Types*, *A&A* **26** (1973) 483.

[22] A. Bosma, *The distribution and kinematics of neutral hydrogen in spiral galaxies of various morphological types*, Ph.D. thesis, University of Groningen, Netherlands, Mar., 1978.

[23] V.C. Rubin, J. Ford, W. K. and N. Thonnard, *Extended rotation curves of high-luminosity spiral galaxies. IV. Systematic dynamical properties, Sa -> Sc.*, *ApJ* **225** (1978) L107.

[24] T. Clifton, P.G. Ferreira, A. Padilla and C. Skordis, *Modified gravity and cosmology*, *Phys. Rep.* **513** (2012) 1 [1106.2476].

[25] B. Carr and F. Kühnel, *Primordial Black Holes as Dark Matter: Recent Developments*, *Annual Review of Nuclear and Particle Science* **70** (2020) 355 [2006.02838].

[26] R.D. Peccei and H.R. Quinn, *CP conservation in the presence of pseudoparticles*, *Phys. Rev. Lett.* **38** (1977) 1440.

[27] S. Weinberg, *A New Light Boson?*, *Phys. Rev. Lett.* **40** (1978) 223.

[28] F. Wilczek, *Problem of Strong P and T Invariance in the Presence of Instantons*, *Phys. Rev. Lett.* **40** (1978) 279.

[29] O.F. Piattella, *Lecture Notes in Cosmology, arXiv e-prints* (2018) arXiv:1803.00070 [`1803.00070`].

[30] J.F. Navarro, C.S. Frenk and S.D.M. White, *The Structure of Cold Dark Matter Halos*, *ApJ* **462** (1996) 563 [`astro-ph/9508025`].

[31] A. Burkert, *The Structure of Dark Matter Halos in Dwarf Galaxies*, *ApJ* **447** (1995) L25 [`astro-ph/9504041`].

[32] S.S. McGaugh and W.J.G. de Blok, *Testing the Dark Matter Hypothesis with Low Surface Brightness Galaxies and Other Evidence*, *ApJ* **499** (1998) 41 [`astro-ph/9801123`].

[33] S. Côté, C. Carignan and K.C. Freeman, *The Various Kinematics of Dwarf Irregular Galaxies in Nearby Groups and Their Dark Matter Distributions*, *AJ* **120** (2000) 3027.

[34] W.J.G. de Blok, S.S. McGaugh, A. Bosma and V.C. Rubin, *Mass Density Profiles of Low Surface Brightness Galaxies*, *ApJ* **552** (2001) L23 [`astro-ph/0103102`].

[35] A. Borriello and P. Salucci, *The dark matter distribution in disc galaxies*, *MNRAS* **323** (2001) 285 [`astro-ph/0001082`].

[36] F.C. van den Bosch and R.A. Swaters, *Dwarf galaxy rotation curves and the core problem of dark matter haloes*, *MNRAS* **325** (2001) 1017 [`astro-ph/0006048`].

[37] W.J.G. de Blok, S.S. McGaugh and V.C. Rubin, *High-Resolution Rotation Curves of Low Surface Brightness Galaxies. II. Mass Models*, *AJ* **122** (2001) 2396.

[38] D. Marchesini, E. D'Onghia, G. Chincarini, C. Firmani, P. Conconi, E. Molinari et al., *Hα Rotation Curves: The Soft Core Question*, *ApJ* **575** (2002) 801 [`astro-ph/0202075`].

[39] G. Gentile, A. Burkert, P. Salucci, U. Klein and F. Walter, *The Dwarf Galaxy DDO 47 as a Dark Matter Laboratory: Testing Cusps Hiding in Triaxial Halos*, *ApJ* **634** (2005) L145 [`astro-ph/0506538`].

[40] R. Kuzio de Naray, S.S. McGaugh, W.J.G. de Blok and A. Bosma, *High-Resolution Optical Velocity Fields of 11 Low Surface Brightness Galaxies*, *ApJS* **165** (2006) 461 [`astro-ph/0604576`].

[41] G. Gentile, P. Salucci, U. Klein and G.L. Granato, *NGC 3741: the dark halo profile from the most extended rotation curve*, *MNRAS* **375** (2007) 199 [`astro-ph/0611355`].

[42] P. Salucci, A. Lapi, C. Tonini, G. Gentile, I. Yegorova and U. Klein, *The universal rotation curve of spiral galaxies - II. The dark matter distribution out to the virial radius*, *MNRAS* **378** (2007) 41 [`astro-ph/0703115`].

[43] R. Kuzio de Naray, S.S. McGaugh and W.J.G. de Blok, *Mass Models for Low Surface Brightness Galaxies with High-Resolution Optical Velocity Fields*, *ApJ* **676** (2008) 920 [`0712.0860`].

[44] M. Kaplinghat, T. Ren and H.-B. Yu, *Dark matter cores and cusps in spiral galaxies and their explanations*, *J. Cosmology Astropart. Phys.* **2020** (2020) 027 [`1911.00544`].

[45] A. Fitts, M. Boylan-Kolchin, B. Bozek, J.S. Bullock, A. Graus, V. Robles et al., *Dwarf galaxies in CDM, WDM, and SIDM: disentangling baryons and dark matter physics*, *MNRAS* **490** (2019) 962 [`1811.11791`].

[46] S. Tulin and H.-B. Yu, *Dark matter self-interactions and small scale structure*, *Phys. Rep.* **730** (2018) 1 [`1705.02358`].

[47] A. Drukier and L. Stodolsky, *Principles and Applications of a Neutral Current Detector for Neutrino Physics and Astronomy*, *Phys. Rev. D* **30** (1984) 2295.

[48] M.W. Goodman and E. Witten, *Detectability of Certain Dark Matter Candidates*, *Phys. Rev. D* **31** (1985) 3059.

[49] S.P. Ahlen, F.T. Avignone, R.L. Brodzinski, A.K. Drukier, G. Gelmini and D.N. Spergel, *Limits on cold dark matter candidates from an ultralow background germanium spectrometer*, *Physics Letters B* **195** (1987) 603.

[50] D.O. Caldwell, R.M. Eisberg, D.M. Grumm, M.S. Witherell, B. Sadoulet, F.S. Goulding et al., *Laboratory Limits on Galactic Cold Dark Matter*, *Phys. Rev. Lett.* **61** (1988) 510.

[51] CDMS-II collaboration, *Dark Matter Search Results from the CDMS II Experiment*, *Science* **327** (2010) 1619 [`0912.3592`].

[52] EDELWEISS collaboration, *Final results of the EDELWEISS-I dark matter search with cryogenic heat-and-ionization Ge detectors*, *Phys. Rev. D* **71** (2005) 122002 [`astro-ph/0503265`].

[53] B. Majorovits et al., *The CRESST dark matter search*, in *5th International Workshop on the Identification of Dark Matter*, pp. 212–217, 11, 2004 [`astro-ph/0411396`].

[54] XENON100 collaboration, *Dark Matter Results from 225 Live Days of XENON100 Data*, *Phys. Rev. Lett.* **109** (2012) 181301 [`1207.5988`].

[55] PandaX collaboration, *Dark Matter Search Results from the Commissioning Run of PandaX-II*, *Phys. Rev. D* **93** (2016) 122009 [`1602.06563`].

[56] LUX collaboration, *First results from the LUX dark matter experiment at the Sanford Underground Research Facility, Phys. Rev. Lett.* **112** (2014) 091303 [1310.8214].

[57] DARKSIDE collaboration, *First Results from the DarkSide-50 Dark Matter Experiment at Laboratori Nazionali del Gran Sasso, Phys. Lett. B* **743** (2015) 456 [1410.0653].

[58] XENON collaboration, *Dark Matter Search Results from a One Ton-Year Exposure of XENON1T, Phys. Rev. Lett.* **121** (2018) 111302 [1805.12562].

[59] J. Aalbers, D.S. Akerib, C.W. Akerlof, A.K. Al Musalhi, F. Alder, A. Alqahtani et al., *First Dark Matter Search Results from the LUX-ZEPLIN (LZ) Experiment, arXiv e-prints* (2022) arXiv:2207.03764 [2207.03764].

[60] (XENON COLLABORATION)††, XENON collaboration, *Search for New Physics in Electronic Recoil Data from XENONnT, Phys. Rev. Lett.* **129** (2022) 161805 [2207.11330].

[61] PANDAX collaboration, *Constraints on the axial-vector and pseudo-scalar mediated WIMP-nucleus interactions from PandaX-4T experiment, Phys. Lett. B* **834** (2022) 137487 [2208.03626].

[62] DARKSIDE 20K collaboration, *Sensitivity of future liquid argon dark matter search experiments to core-collapse supernova neutrinos, JCAP* **03** (2021) 043 [2011.07819].

[63] DARWIN collaboration, *DARWIN: towards the ultimate dark matter detector, JCAP* **11** (2016) 017 [1606.07001].

[64] R. Bernabei, P. Belli, F. Cappella, R. Cerulli, C.J. Dai, A. D'Angelo et al., *First results from DAMA/LIBRA and the combined results with DAMA/NaI, European Physical Journal C* **56** (2008) 333 [0804.2741].

[65] R. Bernabei, P. Belli, F. Cappella, R. Cerulli, C.J. Dai, A. D'Angelo et al., *New results from DAMA/LIBRA, European Physical Journal C* **67** (2010) 39 [1002.1028].

[66] COSINE-100 collaboration, *Strong constraints from COSINE-100 on the DAMA dark matter results using the same sodium iodide target, Sci. Adv.* **7** (2021) abk2699 [2104.03537].

[67] J. Amare et al., *Annual modulation results from three-year exposure of ANAIS-112, Phys. Rev. D* **103** (2021) 102005 [2103.01175].

[68] SABRE collaboration, *Direct search of dark matter with the SABRE experiment*, in *53rd Rencontres de Moriond on Cosmology*, pp. 319–322, 2018 [2004.11308].

[69] G. Angloher, P. Carniti, I. Dafinei, N. Di Marco, A. Fuss, C. Gotti et al., *COSINUS: Cryogenic Calorimeters for the Direct Dark Matter Search with NaI Crystals*, *Journal of Low Temperature Physics* **200** (2020) 428.

[70] M. Schumann, *Direct detection of WIMP dark matter: concepts and status*, *Journal of Physics G Nuclear Physics* **46** (2019) 103003 [1903.03026].

[71] D. Spolyar, K. Freese and P. Gondolo, *Dark matter and the first stars: a new phase of stellar evolution*, *Phys. Rev. Lett.* **100** (2008) 051101 [0705.0521].

[72] T. Abel, G.L. Bryan and M.L. Norman, *The formation of the first star in the Universe*, *Science* **295** (2002) 93 [astro-ph/0112088].

[73] K. Freese, P. Bodenheimer, D. Spolyar and P. Gondolo, *Stellar Structure of Dark Stars: a first phase of Stellar Evolution due to Dark Matter Annihilation*, *ApJ* **685** (2008) L101 [0806.0617].

[74] A. Natarajan, J.C. Tan and B.W. O'Shea, *Dark Matter Annihilation and Primordial Star Formation*, *ApJ* **692** (2009) 574 [0807.3769].

[75] K. Freese, C. Ilie, D. Spolyar, M. Valluri and P. Bodenheimer, *Supermassive Dark Stars: Detectable in JWST*, *ApJ* **716** (2010) 1397 [1002.2233].

[76] T. Rindler-Daller, M.H. Montgomery, K. Freese, D.E. Winget and B. Paxton, *Dark Stars: Improved Models and First Pulsation Results*, *ApJ* **799** (2015) 210 [1408.2082].

[77] T. Rindler-Daller, K. Freese, R.H.D. Townsend and L. Visinelli, *Stability and pulsation of the first dark stars*, *MNRAS* **503** (2021) 3677 [2011.00231].

[78] K. Freese, T. Rindler-Daller, D. Spolyar and M. Valluri, *Dark Stars: A Review*, *Rept. Prog. Phys.* **79** (2016) 066902 [1501.02394].

[79] J.S. Bullock and M. Boylan-Kolchin, *Small-Scale Challenges to the ΛCDM Paradigm*, *ARA&A* **55** (2017) 343 [1707.04256].

[80] J. Zavala and C.S. Frenk, *Dark Matter Haloes and Subhaloes*, *Galaxies* **7** (2019) 81 [1907.11775].

[81] M.R. Lovell and J. Zavala, *Matching the mass function of Milky Way satellites in competing dark matter models*, *arXiv e-prints* (2022) arXiv:2209.06834 [2209.06834].

[82] D. Maoz, F. Mannucci and G. Nelemans, *Observational Clues to the Progenitors of Type Ia Supernovae*, *ARA&A* **52** (2014) 107 [1312.0628].

[83] J.J. Cowan, C. Sneden, J.E. Lawler, A. Aprahamian, M. Wiescher, K. Langanke et al., *Origin of the heaviest elements: The rapid neutron-capture process*, *Reviews of Modern Physics* **93** (2021) 015002 [1901.01410].

[84] J.L. Sanders and P. Das, *Isochrone ages for ∼3 million stars with the second Gaia data release*, *MNRAS* **481** (2018) 4093 [1806.02324].

[85] A.B.A. Queiroz, F. Anders, B.X. Santiago, C. Chiappini, M. Steinmetz, M. Dal Ponte et al., *StarHorse: a Bayesian tool for determining stellar masses, ages, distances, and extinctions for field stars*, *MNRAS* **476** (2018) 2556 [1710.09970].

[86] A. Mints and S. Hekker, *Isochrone fitting in the Gaia era*, *A&A* **618** (2018) A54 [1804.06578].

[87] E. Michel, A. Baglin, M. Auvergne, C. Catala, R. Samadi, F. Baudin et al., *CoRoT Measures Solar-Like Oscillations and Granulation in Stars Hotter Than the Sun*, *Science* **322** (2008) 558 [0812.1267].

[88] W.J. Chaplin, S. Basu, D. Huber, A. Serenelli, L. Casagrande, V. Silva Aguirre et al., *Asteroseismic Fundamental Properties of Solar-type Stars Observed by the NASA Kepler Mission*, *ApJS* **210** (2014) 1 [1310.4001].

[89] D.R. Soderblom, *The Ages of Stars*, *ARA&A* **48** (2010) 581 [1003.6074].

[90] J. Binney and S. Tremaine, *Galactic Dynamics: Second Edition*, Princeton University Press:Princeton, NJ, USA (2008).

[91] E. Vasiliev, *AGAMA: action-based galaxy modelling architecture*, *MNRAS* **482** (2018) 1525 [1802.08239].

[92] A.R. Wetzel, P.F. Hopkins, J. hoon Kim, C.-A. Faucher-Giguère, D. Kereš and E. Quataert, *RECONCILING DWARF GALAXIES WITH λCDM COSMOLOGY: SIMULATING a REALISTIC POPULATION OF SATELLITES AROUND a MILKY WAY–MASS GALAXY*, *ApJ* **827** (2016) L23.

[93] S. Sharma and K.V. Johnston, *A GROUP FINDING ALGORITHM FOR MULTIDIMENSIONAL DATA SETS*, *ApJ* **703** (2009) 1061.

[94] Y. Wu, K. Freese, C. Kelso, P. Stengel and M. Valluri, *Uncertainties in direct dark matter detection in light of Gaia's escape velocity measurements*, *J. Cosmology Astropart. Phys.* **2019** (2019) 034 [1904.04781].

[95] A.K. Drukier, K. Freese and D.N. Spergel, *Detecting Cold Dark Matter Candidates*, *Phys. Rev.* **D33** (1986) 3495.

[96] N.B. et al., *Predictions of hydrodynamic simulations for direct dark matter detection,*, *J. Phys. Conf. Ser.* **718** (2016) 042007.

[97] C. Kelso, C. Savage, M. Valluri, G.S. K. Freese and J. Bailin, *The impact of baryons on the direct detection of dark matter*, *J. Cosmology Astropart. Phys.* **2016** (2016) 071.

[98] A.B. J.D. Sloane, M.R. Buckley and F. Governato, *Assessing astrophysical uncertainties in direct detection with galaxy simulations,*, *ApJ* **831** (2016) 93.

[99] A. Green, *Effect of halo modeling on wimp exclusion limits,*, *Phys. Rev.* **66** (2002) 083003.

[100] C. McCabe, *The astrophysical uncertainties of dark matter direct detection experiments,*, *Phys. Rev.* **82** (2010) 023530.

[101] T.D. M. Fairbairn and J. Swift, *Quantifying astrophysical uncertainties on dark matter direct detection results,*, *Astropart. Phys.* **47** (2013) 45.

[102] M. Benito, N. Bernal, N. Bozorgnia, F. Calore and F. Iocco, *Particle dark matter constraints: the effect of galactic uncertainties*, *J. Cosmology Astropart. Phys.* **2017** (2017) 007 [1612.02010].

[103] A. Green, *Astrophysical uncertainties on the local dark matter distribution and direct detection experiments,*, *J. Phys.* **44** (2017) 084001.

[104] A. Fowlie, *Halo-independence with quantified maximum entropy at dama/libra*, *J. Cosmology Astropart. Phys.* **2017** (2017) 002 [1708.00181].

[105] B.K. A. Ibarra and A. Rappelt, *Bracketing the impact of astrophysical uncertainties on local dark matter searches*, *J. Cosmology Astropart. Phys.* **2018** (2018) 018 [1806.08714].

[106] A. Fowlie, *Non-parametric uncertainties in the dark matter velocity distribution*, *J. Cosmology Astropart. Phys.* **2019** (2019) 006.

[107] M. Petač and P. Ullio, *Two-integral distribution functions in axisymmetric galaxies: implications for dark matter searches,*, *Phys. Rev.* **99** (2019) 043003.

[108] L. Necib, M. Lisanti and V. Belokurov, *Inferred Evidence for Dark Matter Kinematic Substructure with SDSS-Gaia*, *ApJ* **874** (2019) 3 [1807.02519].

[109] C.O. N.W. Evans and C. McCabe, *Refinement of the standard halo model for dark matter searches in light of the gaia sausage,*, *Phys. Rev.* **99** (2019) 023012.

[110] G.G. P. Salucci, F. Nesti and C. Martins, *The dark matter density at the sun's location,*, *Astron. Astrophys.* **523** (2010) A83.

[111] R. Catena and P. Ullio, *A novel determination of the local dark matter density*, *J. Cosmology Astropart. Phys.* **2010** (2010) 004 [0907.0018].

[112] M. Weber and W. de Boer, *Determination of the local dark matter density in our galaxy,*, *Astron. Astrophys.* **509** (2010) A25.

[113] G.B. F. Iocco, M. Pato and P. Jetzer, *Dark matter distribution in the milky way: microlensing and dynamical constraints, J. Cosmology Astropart. Phys.* **2011** (2011) 029 [1107.5810].

[114] P. McMillan, *Mass models of the milky way,, MNRAS* **414** (2011) 2446.

[115] F.I. M. Pato and G. Bertone, *Dynamical constraints on the dark matter distribution in the milky way, J. Cosmology Astropart. Phys.* **2015** (2015) 001 [1504.06324].

[116] A.P. C.F. McKee and D. Hollenbach, *Stars, gas and dark matter in the solar neighborhood,, ApJ* **814** (2015) 13.

[117] Q.X. et al., *Determining the local dark matter density with lamost data,, MNRAS* **458** (2016) 3839.

[118] Y.H. et al., *The milky way's rotation curve out to 100 kpc and its constraint on the galactic mass distribution,, MNRAS* **463** (2016) 2623.

[119] P. McMillan, *The mass distribution and gravitational potential of the milky way,, MNRAS* **465** (2017) 76.

[120] S. Sivertsson, H. Silverwood, G. J.I. Read and P. Steger, *The local dark matter density from sdss-segue g-dwarfs,, MNRAS* **478** (2018) 1677.

[121] S.L. J. Buch and J. Fan, *Using gaia dr2 to constrain local dark matter density and thin dark disk, J. Cosmology Astropart. Phys.* **2019** (2019) 026 [1808.05603].

[122] A. Widmark, *Measuring the local matter density using gaia dr2,, Astron. Astrophys.* **623** (2019) A30.

[123] P.F. de Salas, K. Malhan, K. Freese, K. Hattori and M. Valluri, *On the estimation of the local dark matter density using the rotation curve of the Milky Way, J. Cosmology Astropart. Phys.* **2019** (2019) 037 [1906.06133].

[124] The GAMBIT Dark Matter Workgroup collaboration, *Darkbit: a gambit module for computing dark matter observables and likelihoods,, Eur. Phys. J.* **77** (2017) 831.

[125] G.M. et al., *The escape speed curve of the galaxy obtained from gaia dr2 implies a heavy milky way,, Astron. Astrophys.* **616** (2018) L9.

[126] J. Lavalle and S. Magni, *Making sense of the local galactic escape speed estimates in direct dark matter searches,, Phys. Rev.* **91** (2015) 023510.

[127] J. Read, *The local dark matter density,, J. Phys.* **41** (2014) 063101.

[128] P.M. et al., *Rotation curve of the milky way from classical cepheids,, ApJ* **870** (2019) L10.

[129] H.-W.R. A.-C. Eilers, D.W. Hogg and M. Ness, *The circular velocity curve of the milky way from 5 to 25 kpc,, ApJ* **871** (2019) 120.

[130] M. Reid and A. Brunthaler, *The proper motion of sgr a*. ii. the mass of sgr a*,, ApJ* **616** (2004) 872.

[131] GRAVITY collaboration, *Detection of the gravitational redshift in the orbit of the star s2 near the galactic centre massive black hole,, Astron. Astrophys.* **615** (2018) L15.

[132] GRAVITY Collaboration, R. Abuter, A. Amorim, M. Bauböck, J.P. Berger, H. Bonnet et al., *A geometric distance measurement to the Galactic center black hole with 0.3% uncertainty, A&A* **625** (2019) L10 [`1904.05721`].

[133] R. Barlow, *Asymmetric Statistical Errors, arXiv e-prints* (2004) physics/0406120 [`physics/0406120`].

[134] A.D. et al., *The local high-velocity tail and the galactic escape speed,, MNRAS* **485** (2019) 3514.

[135] Y. Wu, S. Baum, K. Freese, L. Visinelli and H.-B. Yu, *Dark stars powered by self-interacting dark matter, Phys. Rev. D* **106** (2022) 043028 [`2205.10904`].

[136] L. Gao, T. Abel, C.S. Frenk, A. Jenkins, V. Springel and N. Yoshida, *The first generation of stars in ΛCDM cosmology, MNRAS* **378** (2007) 449 [`astro-ph/0610174`].

[137] K. Freese, D. Spolyar and A. Aguirre, *Dark Matter Capture in the first star: a Power source and a limit on Stellar Mass, JCAP* **0811** (2008) 014 [`0802.1724`].

[138] K. Freese, P. Gondolo, J.A. Sellwood and D. Spolyar, *Dark Matter Densities during the Formation of the First Stars and in Dark Stars, ApJ* **693** (2009) 1563 [`0805.3540`].

[139] F. Iocco, *Dark Matter Capture and Annihilation on the First Stars: Preliminary Estimates, ApJLett.* **677** (2008) L1 [`0802.0941`].

[140] F. Iocco, A. Bressan, E. Ripamonti, R. Schneider, A. Ferrara and P. Marigo, *Dark matter annihilation effects on the first stars, MNRAS* **390** (2008) 1655 [`0805.4016`].

[141] C. Ilie, K. Freese, M. Valluri, I.T. Iliev and P. Shapiro, *Observing supermassive dark stars with James Webb Space Telescope, MNRAS* **422** (2012) 2164 [`1110.6202`].

[142] D.N. Spergel and P.J. Steinhardt, *Observational evidence for selfinteracting cold dark matter, Phys. Rev. Lett.* **84** (2000) 3760 [`astro-ph/9909386`].

124

[143] R. Dave, D.N. Spergel, P.J. Steinhardt and B.D. Wandelt, *Halo properties in cosmological simulations of selfinteracting cold dark matter*, *ApJ* **547** (2001) 574 [`astro-ph/0006218`].

[144] M. Rocha, A.H.G. Peter, J.S. Bullock, M. Kaplinghat, S. Garrison-Kimmel, J. Onorbe et al., *Cosmological Simulations with Self-Interacting Dark Matter I: Constant Density Cores and Substructure*, *MNRAS* **430** (2013) 81 [`1208.3025`].

[145] M. Vogelsberger, J. Zavala and A. Loeb, *Subhaloes in Self-Interacting Galactic Dark Matter Haloes*, *MNRAS* **423** (2012) 3740 [`1201.5892`].

[146] M. Kaplinghat, S. Tulin and H.-B. Yu, *Dark Matter Halos as Particle Colliders: Unified Solution to Small-Scale Structure Puzzles from Dwarfs to Clusters*, *Phys. Rev. Lett.* **116** (2016) 041302 [`1508.03339`].

[147] M. Kaplinghat, R.E. Keeley, T. Linden and H.-B. Yu, *Tying Dark Matter to Baryons with Self-interactions*, *Phys. Rev. Lett.* **113** (2014) 021302 [`1311.6524`].

[148] O.D. Elbert, J.S. Bullock, M. Kaplinghat, S. Garrison-Kimmel, A.S. Graus and M. Rocha, *A Testable Conspiracy: Simulating Baryonic Effects on Self-Interacting Dark Matter Halos*, *ApJ* **853** (2018) 109 [`1609.08626`].

[149] O. Sameie, P. Creasey, H.-B. Yu, L.V. Sales, M. Vogelsberger and J. Zavala, *The impact of baryonic discs on the shapes and profiles of self-interacting dark matter haloes*, *MNRAS* **479** (2018) 359 [`1801.09682`].

[150] D. Yang and H.-B. Yu, *Self-interacting dark matter and small-scale gravitational lenses in galaxy clusters*, *Phys. Rev. D* **104** (2021) 103031 [`2102.02375`].

[151] A. Kamada, M. Kaplinghat, A.B. Pace and H.-B. Yu, *How the Self-Interacting Dark Matter Model Explains the Diverse Galactic Rotation Curves*, *Phys. Rev. Lett.* **119** (2017) 111102 [`1611.02716`].

[152] P. Creasey, O. Sameie, L.V. Sales, H.-B. Yu, M. Vogelsberger and J. Zavala, *Spreading out and staying sharp – creating diverse rotation curves via baryonic and self-interaction effects*, *MNRAS* **468** (2017) 2283 [`1612.03903`].

[153] T. Ren, A. Kwa, M. Kaplinghat and H.-B. Yu, *Reconciling the Diversity and Uniformity of Galactic Rotation Curves with Self-Interacting Dark Matter*, *Phys. Rev. X* **9** (2019) 031020 [`1808.05695`].

[154] K.A. Oman et al., *The unexpected diversity of dwarf galaxy rotation curves*, *MNRAS* **452** (2015) 3650 [`1504.01437`].

[155] P. Salucci, *Dark Matter in Galaxies: evidences and challenges*, *Found. Phys.* **48** (2018) 1517 [`1807.08541`].

[156] S. McGaugh, *Predictions and Outcomes for the Dynamics of Rotating Galaxies*, *Galaxies* **8** (2020) 35 [2004.14402].

[157] P. Salucci, *The distribution of dark matter in galaxies*, *Astron. Astrophys. Rev.* **27** (2019) 2 [1811.08843].

[158] A. Del Popolo and M. Le Delliou, *Small scale problems of the ΛCDM model: a short review*, *Galaxies* **5** (2017) 17 [1606.07790].

[159] L. Perivolaropoulos and F. Skara, *Challenges for ΛCDM: An update*, 2105.05208.

[160] K.E. Andrade, J. Fuson, S. Gad-Nasr, D. Kong, Q. Minor, M.G. Roberts et al., *A Stringent Upper Limit on Dark Matter Self-Interaction Cross Section from Cluster Strong Lensing*, *MNRAS* **510** (2021) 54 [2012.06611].

[161] G.R. Blumenthal, S.M. Faber, R. Flores and J.R. Primack, *Contraction of Dark Matter Galactic Halos Due to Baryonic Infall*, *ApJ* **301** (1986) 27.

[162] J. Barnes and S.D.M. White, *The response of a spheroid to a disc field or were bulges ever ellipticals?*, *MNRAS* **211** (1984) 753.

[163] B.S. Ryden and J.E. Gunn, *Galaxy formation by gravitational collapse*, *ApJ* **318** (1987) 15.

[164] P. Young, *Numerical models of star clusters with a central black hole. I - Adiabatic models.*, *ApJ* **242** (1980) 1232.

[165] O.Y. Gnedin, A.V. Kravtsov, A.A. Klypin and D. Nagai, *Response of Dark Matter Halos to Condensation of Baryons: Cosmological Simulations and Improved Adiabatic Contraction Model*, *ApJ* **616** (2004) 16 [astro-ph/0406247].

[166] J.A. Sellwood and S.S. McGaugh, *The Compression of dark matter halos by baryonic infall*, *ApJ* **634** (2005) 70 [astro-ph/0507589].

[167] S. Balberg, S.L. Shapiro and S. Inagaki, *Selfinteracting dark matter halos and the gravothermal catastrophe*, *ApJ* **568** (2002) 475 [astro-ph/0110561].

[168] K.-J. Ahn and P.R. Shapiro, *Formation and evolution of the self-interacting dark matter halos*, *MNRAS* **363** (2005) 1092 [astro-ph/0412169].

[169] J. Koda and P.R. Shapiro, *Gravothermal collapse of isolated self-interacting dark matter haloes: N-body simulation versus the fluid model*, *MNRAS* **415** (2011) 1125 [1101.3097].

[170] J. Pollack, D.N. Spergel and P.J. Steinhardt, *Supermassive Black Holes from Ultra-Strongly Self-Interacting Dark Matter*, *ApJ* **804** (2015) 131 [1501.00017].

[171] R. Essig, S.D. Mcdermott, H.-B. Yu and Y.-M. Zhong, *Constraining Dissipative Dark Matter Self-Interactions*, *Phys. Rev. Lett.* **123** (2019) 121102 [1809.01144].

[172] J. Choquette, J.M. Cline and J.M. Cornell, *Early formation of supermassive black holes via dark matter self-interactions*, *JCAP* **07** (2019) 036 [1812.05088].

[173] H. Nishikawa, K.K. Boddy and M. Kaplinghat, *Accelerated core collapse in tidally stripped self-interacting dark matter halos*, *Phys. Rev. D* **101** (2020) 063009 [1901.00499].

[174] O. Sameie, H.-B. Yu, L.V. Sales, M. Vogelsberger and J. Zavala, *Self-Interacting Dark Matter Subhalos in the Milky Way's Tides*, *Phys. Rev. Lett.* **124** (2020) 141102 [1904.07872].

[175] S. Tulin, H.-B. Yu and K.M. Zurek, *Beyond Collisionless Dark Matter: Particle Physics Dynamics for Dark Matter Halo Structure*, *Phys. Rev. D* **87** (2013) 115007 [1302.3898].

[176] F. Kahlhoefer, K. Schmidt-Hoberg and S. Wild, *Dark matter self-interactions from a general spin-0 mediator*, *JCAP* **08** (2017) 003 [1704.02149].

[177] T. Bringmann, F. Kahlhoefer, K. Schmidt-Hoberg and P. Walia, *Strong constraints on self-interacting dark matter with light mediators*, *Phys. Rev. Lett.* **118** (2017) 141802 [1612.00845].

[178] M. Cirelli, P. Panci, K. Petraki, F. Sala and M. Taoso, *Dark Matter's secret liaisons: phenomenology of a dark U(1) sector with bound states*, *JCAP* **05** (2017) 036 [1612.07295].

[179] S.-M. Choi, Y.-J. Kang and H.M. Lee, *On thermal production of self-interacting dark matter*, *JHEP* **12** (2016) 099 [1610.04748].

[180] X. Chu, C. Garcia-Cely and H. Murayama, *Velocity Dependence from Resonant Self-Interacting Dark Matter*, *Phys. Rev. Lett.* **122** (2019) 071103 [1810.04709].

[181] PANDAX-II collaboration, *Constraining Dark Matter Models with a Light Mediator at the PandaX-II Experiment*, *Phys. Rev. Lett.* **121** (2018) 021304 [1802.06912].

[182] N. Bernal, X. Chu, S. Kulkarni and J. Pradler, *Self-interacting dark matter without prejudice*, *Phys. Rev. D* **101** (2020) 055044 [1912.06681].

[183] E. Ma, *Two-loop Z_4 Dirac neutrino masses and mixing, with self-interacting dark matter*, *Nucl. Phys. B* **946** (2019) 114725 [1907.04665].

[184] Y.-D. Tsai, R. McGehee and H. Murayama, *Resonant Self-Interacting Dark Matter from Dark QCD*, 2008.08608.

[185] PandaX-II collaboration, *Constraining self-interacting dark matter with the full dataset of PandaX-II*, *Sci. China Phys. Mech. Astron.* **64** (2021) 111062 [2104.14724].

[186] J. Fan, M. Reece and L.-T. Wang, *Non-relativistic effective theory of dark matter direct detection*, *JCAP* **11** (2010) 042 [1008.1591].

[187] A.L. Fitzpatrick, W. Haxton, E. Katz, N. Lubbers and Y. Xu, *The Effective Field Theory of Dark Matter Direct Detection*, *JCAP* **02** (2013) 004 [1203.3542].

[188] J.B. Dent, L.M. Krauss, J.L. Newstead and S. Sabharwal, *General analysis of direct dark matter detection: From microphysics to observational signatures*, *Phys. Rev. D* **92** (2015) 063515 [1505.03117].

[189] S. Cassel, *Sommerfeld factor for arbitrary partial wave processes*, *J. Phys. G* **37** (2010) 105009 [0903.5307].

[190] Planck collaboration, *Planck 2018 results. VI. Cosmological parameters*, *Astron. Astrophys.* **641** (2020) A6 [1807.06209].

[191] T.R. Slatyer, *Indirect dark matter signatures in the cosmic dark ages. I. Generalizing the bound on s-wave dark matter annihilation from Planck results*, *Phys. Rev. D* **93** (2016) 023527 [1506.03811].

[192] T.R. Slatyer, *Indirect Dark Matter Signatures in the Cosmic Dark Ages II. Ionization, Heating and Photon Production from Arbitrary Energy Injections*, *Phys. Rev. D* **93** (2016) 023521 [1506.03812].

[193] K. Abazajian et al., *CMB-S4 Science Case, Reference Design, and Project Plan*, 1907.04473.

[194] D. Green, P.D. Meerburg and J. Meyers, *Aspects of Dark Matter Annihilation in Cosmology*, *JCAP* **04** (2019) 025 [1804.01055].

[195] J.L. Feng, M. Kaplinghat and H.-B. Yu, *Sommerfeld Enhancements for Thermal Relic Dark Matter*, *Phys. Rev. D* **82** (2010) 083525 [1005.4678].

[196] L.G. van den Aarssen, T. Bringmann and C. Pfrommer, *Is dark matter with long-range interactions a solution to all small-scale problems of \Lambda CDM cosmology?*, *Phys. Rev. Lett.* **109** (2012) 231301 [1205.5809].

[197] F.-Y. Cyr-Racine, K. Sigurdson, J. Zavala, T. Bringmann, M. Vogelsberger and C. Pfrommer, *ETHOS—an effective theory of structure formation: From dark particle physics to the matter distribution of the Universe*, *Phys. Rev. D* **93** (2016) 123527 [1512.05344].

[198] R. Huo, M. Kaplinghat, Z. Pan and H.-B. Yu, *Signatures of Self-Interacting Dark Matter in the Matter Power Spectrum and the CMB*, *Phys. Lett. B* **783** (2018) 76 [1709.09717].

[199] R. Huo, *Matter Power Spectrum of Light Freeze-in Dark Matter: With or without Self-Interaction*, *Phys. Lett. B* **802** (2020) 135251 [1907.02454].

[200] D. Egana-Ugrinovic, R. Essig, D. Gift and M. LoVerde, *The Cosmological Evolution of Self-interacting Dark Matter*, *JCAP* **05** (2021) 013 [2102.06215].

[201] N. Arkani-Hamed, D.P. Finkbeiner, T.R. Slatyer and N. Weiner, *A Theory of Dark Matter*, *Phys. Rev. D* **79** (2009) 015014 [0810.0713].

[202] M.J. Dolan, F. Kahlhoefer, C. McCabe and K. Schmidt-Hoberg, *A taste of dark matter: Flavour constraints on pseudoscalar mediators*, *JHEP* **03** (2015) 171 [1412.5174].

[203] M. Hufnagel, K. Schmidt-Hoberg and S. Wild, *BBN constraints on MeV-scale dark sectors. Part II. Electromagnetic decays*, *JCAP* **11** (2018) 032 [1808.09324].

[204] P.F. Depta, M. Hufnagel and K. Schmidt-Hoberg, *Updated BBN constraints on electromagnetic decays of MeV-scale particles*, *JCAP* **04** (2021) 011 [2011.06519].

[205] R. Essig, N. Sehgal and L.E. Strigari, *Bounds on Cross-sections and Lifetimes for Dark Matter Annihilation and Decay into Charged Leptons from Gamma-ray Observations of Dwarf Galaxies*, *Phys. Rev. D* **80** (2009) 023506 [0902.4750].

[206] FERMI-LAT collaboration, *Searching for Dark Matter Annihilation from Milky Way Dwarf Spheroidal Galaxies with Six Years of Fermi Large Area Telescope Data*, *Phys. Rev. Lett.* **115** (2015) 231301 [1503.02641].

[207] S. Hoof, A. Geringer-Sameth and R. Trotta, *A Global Analysis of Dark Matter Signals from 27 Dwarf Spheroidal Galaxies using 11 Years of Fermi-LAT Observations*, *JCAP* **02** (2020) 012 [1812.06986].

[208] S. Ando, A. Geringer-Sameth, N. Hiroshima, S. Hoof, R. Trotta and M.G. Walker, *Structure formation models weaken limits on WIMP dark matter from dwarf spheroidal galaxies*, *Phys. Rev. D* **102** (2020) 061302 [2002.11956].

[209] M. Kaplinghat, T. Linden and H.-B. Yu, *Galactic Center Excess in γ Rays from Annihilation of Self-Interacting Dark Matter*, *Phys. Rev. Lett.* **114** (2015) 211303 [1501.03507].

[210] N.J. Outmezguine, K.K. Boddy, S. Gad-Nasr, M. Kaplinghat and L. Sagunski, *Universal gravothermal evolution of isolated self-interacting dark matter halos for velocity-dependent cross sections*, 2204.06568.

[211] S. Yang, X. Du, Z.C. Zeng, A. Benson, F. Jiang, E.O. Nadler et al., *Gravothermal solutions of SIDM halos: mapping from constant to velocity-dependent cross section*, 2205.02957.

[212] D. Yang and H.-B. Yu, *Gravothermal evolution of dark matter halos with differential elastic scattering*, 2205.03392.

[213] R. Huo, H.-B. Yu and Y.-M. Zhong, *The Structure of Dissipative Dark Matter Halos*, *JCAP* **06** (2020) 051 [1912.06757].

[214] H.C. Turner, M.R. Lovell, J. Zavala and M. Vogelsberger, *The onset of gravothermal core collapse in velocity-dependent self-interacting dark matter subhaloes*, *MNRAS* **505** (2021) 5327 [2010.02924].

[215] C.A. Correa, *Constraining velocity-dependent self-interacting dark matter with the Milky Way's dwarf spheroidal galaxies*, *MNRAS* **503** (2021) 920 [2007.02958].

[216] O. Sameie, M. Boylan-Kolchin, R. Sanderson, D. Vargya, P.F. Hopkins, A. Wetzel et al., *The central densities of Milky Way-mass galaxies in cold and self-interacting dark matter models*, *MNRAS* **507** (2021) 720 [2102.12480].

[217] Z.C. Zeng, A.H.G. Peter, X. Du, A. Benson, S. Kim, F. Jiang et al., *Core-collapse, evaporation and tidal effects: the life story of a self-interacting dark matter subhalo*, 2110.00259.

[218] M. Silverman, J.S. Bullock, M. Kaplinghat, V.H. Robles and M. Valli, *Motivations for a Large Self-Interacting Dark Matter Cross Section from Milky Way Satellites*, 2203.10104.

[219] P. Bodenheimer, H.W. Yorke, M. Rozyczka, G.P. Laughlin and T. Plewa, *Numerical methods in astrophysics : an introduction*, New York: Taylor & Francis (2006), 10.1201/9781420011869.

[220] C.A. Iglesias and F.J. Rogers, *Updated Opal Opacities*, *ApJ* **464** (1996) 943.

[221] P. Lenzuni, D.F. Chernoff and E.E. Salpeter, *Rosseland and Planck Mean Opacities of a Zero-Metallicity Gas*, *ApJSuppl.* **76** (1991) 759.

[222] A.R. Zentner, *High-Energy Neutrinos From Dark Matter Particle Self-Capture Within the Sun*, *Phys. Rev. D* **80** (2009) 063501 [0907.3448].

[223] C. Kouvaris, *Limits on Self-Interacting Dark Matter*, *Phys. Rev. Lett.* **108** (2012) 191301 [1111.4364].

[224] J.P. Gardner et al., *The James Webb Space Telescope*, *Space Sci. Rev.* **123** (2006) 485 [astro-ph/0606175].

[225] Y. Wu, M. Valluri, N. Panithanpaisal, R.E. Sanderson, K. Freese, A. Wetzel et al., *Using action space clustering to constrain the recent accretion history of Milky Way-like galaxies*, *MNRAS* **509** (2022) 5882 [`2104.08185`].

[226] O. Fakhouri and C.-P. Ma, *The nearly universal merger rate of dark matter haloes in ΛCDM cosmology*, *MNRAS* **386** (2008) 577 [`0710.4567`].

[227] D. Erkal, V. Belokurov, J. Bovy and J.L. Sanders, *1606.04946*, *MNRAS* **463** (2016) 102 [`1606.04946`].

[228] A.M. Price-Whelan and A. Bonaca, *Off the Beaten Path: Gaia Reveals GD-1 Stars outside of the Main Stream*, *ApJ* **863** (2018) L20 [`1805.00425`].

[229] A. Bonaca, D.W. Hogg, A.M. Price-Whelan and C. Conroy, *The Spur and the Gap in GD-1: Dynamical Evidence for a Dark Substructure in the Milky Way Halo*, *ApJ* **880** (2019) 38 [`1811.03631`].

[230] R. Feldmann and D. Spolyar, *Detecting dark matter substructures around the Milky Way with Gaia*, *MNRAS* **446** (2015) 1000 [`1310.2243`].

[231] L.M. Widrow, S. Gardner, B. Yanny, S. Dodelson and H.-Y. Chen, *Galactoseismology: Discovery of Vertical Waves in the Galactic Disk*, *ApJ* **750** (2012) L41 [`1203.6861`].

[232] T. Antoja, A. Helmi, M. Romero-Gómez, D. Katz, C. Babusiaux, R. Drimmel et al., *A dynamically young and perturbed Milky Way disk*, *Nature* **561** (2018) 360 [`1804.10196`].

[233] A. Lazar, J.S. Bullock, M. Boylan-Kolchin, T.K. Chan, P.F. Hopkins, A.S. Graus et al., *A dark matter profile to model diverse feedback-induced core sizes of ΛCDM haloes*, *MNRAS* **497** (2020) 2393 [`2004.10817`].

[234] K.V. Johnston, L. Hernquist and M. Bolte, *Fossil Signatures of Ancient Accretion Events in the Halo*, *ApJ* **465** (1996) 278 [`astro-ph/9602060`].

[235] S. Tremaine, *The geometry of phase mixing*, *MNRAS* **307** (1999) 877 [`astro-ph/9812146`].

[236] A. Helmi and P.T. de Zeeuw, *Mapping the substructure in the Galactic halo with the next generation of astrometric satellites*, *MNRAS* **319** (2000) 657 [`astro-ph/0007166`].

[237] P. Harding, H.L. Morrison, E.W. Olszewski, J. Arabadjis, M. Mateo, R.C. Dohm-Palmer et al., *Mapping the Galactic Halo. III. Simulated Observations of Tidal Streams*, *AJ* **122** (2001) 1397 [`astro-ph/0012307`].

[238] M.A.C. Perryman, K.S. de Boer, G. Gilmore, E. Høg, M.G. Lattanzi, L. Lindegren et al., *GAIA: Composition, formation and evolution of the Galaxy*, *A&A* **369** (2001) 339 [`astro-ph/0101235`].

[239] C. Fabricius, U. Bastian, J. Portell, J. Castañeda, M. Davidson, N.C. Hambly et al., *Gaia Data Release 1. Pre-processing and source list creation*, *A&A* **595** (2016) A3 [1609.04273].

[240] L. Lindegren, U. Lammers, U. Bastian, J. Hernández, S. Klioner, D. Hobbs et al., *Gaia Data Release 1. Astrometry: one billion positions, two million proper motions and parallaxes*, *A&A* **595** (2016) A4 [1609.04303].

[241] L. Lindegren, J. Hernández, A. Bombrun, S. Klioner, U. Bastian, M. Ramos-Lerate et al., *Gaia Data Release 2. The astrometric solution*, *A&A* **616** (2018) A2 [1804.09366].

[242] D.W. Evans, M. Riello, F. De Angeli, J.M. Carrasco, P. Montegriffo, C. Fabricius et al., *Gaia Data Release 2. Photometric content and validation*, *A&A* **616** (2018) A4 [1804.09368].

[243] F.A. Gómez, A. Helmi, A.G.A. Brown and Y.-S. Li, *On the identification of merger debris in the Gaia era*, *MNRAS* **408** (2010) 935 [1004.4974].

[244] V. Belokurov, D. Erkal, N.W. Evans, S.E. Koposov and A.J. Deason, *Co-formation of the disc and the stellar halo*, *MNRAS* **478** (2018) 611 [1802.03414].

[245] A. Helmi, C. Babusiaux, H.H. Koppelman, D. Massari, J. Veljanoski and A.G.A. Brown, *The merger that led to the formation of the Milky Way's inner stellar halo and thick disk*, *Nature* **563** (2018) 85 [1806.06038].

[246] G.C. Myeong, N.W. Evans, V. Belokurov, J.L. Sand ers and S.E. Koposov, *The Milky Way Halo in Action Space*, *ApJ* **856** (2018) L26 [1802.03351].

[247] G.C. Myeong, N.W. Evans, V. Belokurov, J.L. Sanders and S.E. Koposov, *Discovery of new retrograde substructures: the shards of Centauri?*, *MNRAS* **478** (2018) 5449.

[248] N.W. Borsato, S.L. Martell and J.D. Simpson, *Identifying stellar streams in Gaia DR2 with data mining techniques*, *MNRAS* **492** (2020) 1370 [1907.02527].

[249] I.U. Roederer, K. Hattori and M. Valluri, *Kinematics of Highly r-process-enhanced Field Stars: Evidence for an Accretion Origin and Detection of Several Groups from Disrupted Satellites*, *AJ* **156** (2018) 179 [1808.09467].

[250] Z. Yuan, G.C. Myeong, T.C. Beers, N.W. Evans, Y.S. Lee, P. Banerjee et al., *Dynamical Relics of the Ancient Galactic Halo*, *ApJ* **891** (2020) 39 [1910.07538].

[251] G. Limberg, S. Rossi, T.C. Beers, H.D. Perottoni, A. Pérez-Villegas, R.M. Santucci et al., *Dynamically Tagged Groups of Very Metal-poor Halo Stars from the HK and Hamburg/ESO Surveys*, ApJ **907** (2021) 10 [2011.08305].

[252] D. Gudin, D. Shank, T.C. Beers, Z. Yuan, G. Limberg, I.U. Roederer et al., *The R-Process Alliance: Chemodynamically Tagged Groups of Halo r-process-enhanced Stars Reveal a Shared Chemical-evolution History*, ApJ **908** (2021) 79 [2012.13808].

[253] L. Necib, B. Ostdiek, M. Lisanti, T. Cohen, M. Freytsis and S. Garrison-Kimmel, *Chasing Accreted Structures within Gaia DR2 using Deep Learning*, arXiv e-prints (2019) arXiv:1907.07681 [1907.07681].

[254] L. Necib, B. Ostdiek, M. Lisanti, T. Cohen, M. Freytsis, S. Garrison-Kimmel et al., *Evidence for a vast prograde stellar stream in the solar vicinity*, Nature Astronomy (2020) [1907.07190].

[255] D.B. Zucker, J.D. Simpson, S.L. Martell, G.F. Lewis, A.R. Casey, Y.-S. Ting et al., *The GALAH Survey: No Chemical Evidence of an Extragalactic Origin for the Nyx Stream*, ApJ **912** (2021) L30 [2104.08684].

[256] G.C. Myeong, E. Vasiliev, G. Iorio, N.W. Evans and V. Belokurov, *Evidence for two early accretion events that built the Milky Way stellar halo*, MNRAS **488** (2019) 1235 [1904.03185].

[257] D. Lynden-Bell and R.M. Lynden-Bell, *Ghostly streams from the formation of the Galaxy's halo*, MNRAS **275** (1995) 429.

[258] G. Besla, N. Kallivayalil, L. Hernquist, B. Robertson, T.J. Cox, R.P. van der Marel et al., *Are the Magellanic Clouds on Their First Passage about the Milky Way?*, ApJ **668** (2007) 949 [astro-ph/0703196].

[259] G. Besla, N. Kallivayalil, L. Hernquist, R.P. van der Marel, T.J. Cox and D. Kereš, *Simulations of the Magellanic Stream in a First Infall Scenario*, ApJ **721** (2010) L97 [1008.2210].

[260] P.F. Hopkins, A. Wetzel, D. Kereš, C.-A. Faucher-Giguère, E. Quataert, M. Boylan-Kolchin et al., *FIRE-2 simulations: physics versus numerics in galaxy formation*, MNRAS **480** (2018) 800 [1702.06148].

[261] P.F. Hopkins, *A new class of accurate, mesh-free hydrodynamic simulation methods*, MNRAS **450** (2015) 53 [1409.7395].

[262] S. Garrison-Kimmel, P.F. Hopkins, A. Wetzel, J.S. Bullock, M. Boylan-Kolchin, D. Kereš et al., *The Local Group on FIRE: dwarf galaxy populations across a suite of hydrodynamic simulations*, MNRAS **487** (2019) 1380 [1806.04143].

[263] J. Samuel, A. Wetzel, E. Tollerud, S. Garrison-Kimmel, S. Loebman, K. El-Badry et al., *A profile in FIRE: resolving the radial distributions of satellite galaxies in the Local Group with simulations*, *MNRAS* **491** (2020) 1471 [1904.11508].

[264] J. Samuel, A. Wetzel, S. Chapman, E. Tollerud, P.F. Hopkins, M. Boylan-Kolchin et al., *Planes of satellites around Milky Way/M31-mass galaxies in the FIRE simulations and comparisons with the Local Group*, *arXiv e-prints* (2020) arXiv:2010.08571 [2010.08571].

[265] P.S. Behroozi, R.H. Wechsler and H.-Y. Wu, *The ROCKSTAR Phase-space Temporal Halo Finder and the Velocity Offsets of Cluster Cores*, *ApJ* **762** (2013) 109 [1110.4372].

[266] P.S. Behroozi, R.H. Wechsler, H.-Y. Wu, M.T. Busha, A.A. Klypin and J.R. Primack, *Gravitationally Consistent Halo Catalogs and Merger Trees for Precision Cosmology*, *ApJ* **763** (2013) 18 [1110.4370].

[267] A. Wetzel and S. Garrison-Kimmel, *GizmoAnalysis: Read and analyze Gizmo simulations*, Feb., 2020.

[268] A. Wetzel and S. Garrison-Kimmel, *HaloAnalysis: Read and analyze halo catalogs and merger trees*, Feb., 2020.

[269] I.B. Santistevan, A. Wetzel, K. El-Badry, J. Bland-Hawthorn, M. Boylan-Kolchin, J. Bailin et al., *The formation times and building blocks of Milky Way-mass galaxies in the FIRE simulations*, *MNRAS* **497** (2020) 747 [2001.03178].

[270] S. Yu, J.S. Bullock, A. Wetzel, R.E. Sand erson, A.S. Graus, M. Boylan-Kolchin et al., *Stars made in outflows may populate the stellar halo of the Milky Way*, *MNRAS* **494** (2020) 1539 [1912.03316].

[271] A. Zolotov, B. Willman, A.M. Brooks, F. Governato, C.B. Brook, D.W. Hogg et al., *The Dual Origin of Stellar Halos*, *ApJ* **702** (2009) 1058 [0904.3333].

[272] A.P. Cooper, S. Cole, C.S. Frenk, S.D.M. White, J. Helly, A.J. Benson et al., *Galactic stellar haloes in the CDM model*, *MNRAS* **406** (2010) 744 [0910.3211].

[273] A.S. Font, I.G. McCarthy, R.A. Crain, T. Theuns, J. Schaye, R.P.C. Wiersma et al., *Cosmological simulations of the formation of the stellar haloes around disc galaxies*, *MNRAS* **416** (2011) 2802 [1102.2526].

[274] A. Zolotov, A.M. Brooks, B. Willman, F. Governato, A. Pontzen, C. Christensen et al., *Baryons Matter: Why Luminous Satellite Galaxies have Reduced Central Masses*, *ApJ* **761** (2012) 71 [1207.0007].

[275] P.B. Tissera, C. Scannapieco, T.C. Beers and D. Carollo, *Stellar haloes of simulated Milky-Way-like galaxies: chemical and kinematic properties*, *MNRAS* **432** (2013) 3391 [1301.1301].

[276] A. Pillepich, P. Madau and L. Mayer, *Building Late-type Spiral Galaxies by In-situ and Ex-situ Star Formation*, *ApJ* **799** (2015) 184 [1407.7855].

[277] A. Monachesi, F.A. Gómez, R.J.J. Grand , C.M. Simpson, G. Kauffmann, S. Bustamante et al., *The Auriga stellar haloes: connecting stellar population properties with accretion and merging history*, *MNRAS* **485** (2019) 2589 [1804.07798].

[278] E.F. Bell, D.B. Zucker, V. Belokurov, S. Sharma, K.V. Johnston, J.S. Bullock et al., *The Accretion Origin of the Milky Way's Stellar Halo*, *ApJ* **680** (2008) 295 [0706.0004].

[279] R.P. Naidu, C. Conroy, A. Bonaca, B.D. Johnson, Y.-S. Ting, N. Caldwell et al., *Evidence from the H3 Survey That the Stellar Halo Is Entirely Comprised of Substructure*, *ApJ* **901** (2020) 48 [2006.08625].

[280] A. Bonaca, C. Conroy, A. Wetzel, P.F. Hopkins and D. Kereš, *Gaia Reveals a Metal-rich, in situ Component of the Local Stellar Halo*, *ApJ* **845** (2017) 101 [1704.05463].

[281] M. Haywood, P. Di Matteo, M.D. Lehnert, O. Snaith, S. Khoperskov and A. Gómez, *In Disguise or Out of Reach: First Clues about In Situ and Accreted Stars in the Stellar Halo of the Milky Way from Gaia DR2*, *ApJ* **863** (2018) 113 [1805.02617].

[282] P. Di Matteo, M. Haywood, M.D. Lehnert, D. Katz, S. Khoperskov, O.N. Snaith et al., *The Milky Way has no in-situ halo other than the heated thick disc. Composition of the stellar halo and age-dating the last significant merger with Gaia DR2 and APOGEE*, *A&A* **632** (2019) A4 [1812.08232].

[283] C. Gallart, E.J. Bernard, C.B. Brook, T. Ruiz-Lara, S. Cassisi, V. Hill et al., *Uncovering the birth of the Milky Way through accurate stellar ages with Gaia*, *Nature Astronomy* **3** (2019) 932 [1901.02900].

[284] V. Belokurov, J.L. Sanders, A. Fattahi, M.C. Smith, A.J. Deason, N.W. Evans et al., *The biggest splash*, *MNRAS* **494** (2020) 3880 [1909.04679].

[285] B. Ostdiek, L. Necib, T. Cohen, M. Freytsis, M. Lisanti, S. Garrison-Kimmel et al., *Cataloging Accreted Stars within Gaia DR2 using Deep Learning*, *Astron. Astrophys.* **636** (2020) A75 [1907.06652].

[286] R.E. Sanderson, A. Wetzel, S. Loebman, S. Sharma, P.F. Hopkins, S. Garrison-Kimmel et al., *Synthetic Gaia Surveys from the FIRE Cosmological Simulations of Milky Way-mass Galaxies*, *ApJS* **246** (2020) 6 [1806.10564].

[287] S. Garrison-Kimmel, P.F. Hopkins, A. Wetzel, K. El-Badry, R.E. Sanderson, J.S. Bullock et al., *The origin of the diverse morphologies and kinematics of Milky Way-mass galaxies in the FIRE-2 simulations*, *MNRAS* **481** (2018) 4133 [1712.03966].

[288] N. Panithanpaisal, R.E. Sanderson, A. Wetzel, E.C. Cunningham, J. Bailin and C.-A. Faucher-Giguère, *The Galaxy Progenitors of Stellar Streams around Milky Way-mass Galaxies in the FIRE Cosmological Simulations*, *arXiv e-prints* (2021) arXiv:2104.09660 [2104.09660].

[289] J. Binney, *Actions for axisymmetric potentials*, *MNRAS* **426** (2012) 1324 [1207.4910].

[290] R. Sanderson, A. Wetzel, S. Sharma and P. Hopkins, *Better Galactic Mass Models through Chemistry*, *Galaxies* **5** (2017) 43.

[291] B. Harmsen, A. Monachesi, E.F. Bell, R.S. de Jong, J. Bailin, D.J. Radburn-Smith et al., *Diverse stellar haloes in nearby Milky Way mass disc galaxies*, *MNRAS* **466** (2017) 1491 [1611.05448].

[292] I.B. Santistevan, A. Wetzel, R.E. Sanderson, K. El-Badry, J. Samuel and C.-A. Faucher-Giguère, *The origin of metal-poor stars on prograde disk orbits in FIRE simulations of Milky Way-mass galaxies*, *arXiv e-prints* (2021) arXiv:2102.03369 [2102.03369].

[293] E. Applebaum, A.M. Brooks, C.R. Christensen, F. Munshi, T.R. Quinn, S. Shen et al., *Ultra-faint dwarfs in a Milky Way context: Introducing the Mint Condition DC Justice League Simulations*, *arXiv e-prints* (2020) arXiv:2008.11207 [2008.11207].

[294] R.S. de Jong, O. Bellido-Tirado, C. Chiappini, É. Depagne, R. Haynes, D. Johl et al., *4MOST: 4-metre multi-object spectroscopic telescope*, in *Ground-based and Airborne Instrumentation for Astronomy IV*, I.S. McLean, S.K. Ramsay and H. Takami, eds., vol. 8446 of *Society of Photo-Optical Instrumentation Engineers (SPIE) Conference Series*, pp. 252 – 266, International Society for Optics and Photonics, SPIE, 2012, DOI.

[295] G. Dalton, S. Trager, D.C. Abrams, P. Bonifacio, J.A. López Aguerri, K. Middleton et al., *Project overview and update on WEAVE: the next generation wide-field spectroscopy facility for the William Herschel Telescope*, in *Proc. SPIE*, vol. 9147 of *Society of Photo-Optical Instrumentation Engineers (SPIE) Conference Series*, p. 91470L, SPIE (2014), DOI.

[296] DESI Collaboration, A. Aghamousa, J. Aguilar, S. Ahlen, S. Alam, L.E. Allen et al., *The DESI Experiment Part I: Science,Targeting, and Survey Design*, *ArXiv e-prints, arXiv:1611.00036* (2016) [1611.00036].

[297] DESI Collaboration, A. Aghamousa, J. Aguilar, S. Ahlen, S. Alam, L.E. Allen et al., *The DESI Experiment Part II: Instrument Design*, *ArXiv e-prints*, *arXiv:1611.00037* (2016) [1611.00037].

[298] P.J. Rousseeuw, *Silhouettes: A graphical aid to the interpretation and validation of cluster analysis*, *Journal of Computational and Applied Mathematics* **20** (1987) 53 .

[299] J.L. Sanders and J. Binney, *TACT: The Action Computation Tool*, Dec., 2015.

[300] J.L. Sanders and J. Binney, *A fast algorithm for estimating actions in triaxial potentials*, *MNRAS* **447** (2015) 2479 [1412.2093].

[301] L. Necib and T. Lin, *Substructure at High Speed. II. The Local Escape Velocity and Milky Way Mass with Gaia eDR3*, *ApJ* **926** (2022) 189 [2102.02211].

[302] WFIRST Astrometry Working Group, R.E. Sanderson, A. Bellini, S. Casertano, J.R. Lu, P. Melchior et al., *Astrometry with the Wide-Field Infrared Space Telescope*, *Journal of Astronomical Telescopes, Instruments, and Systems* **5** (2019) 044005 [1712.05420].

[303] L. Breiman, J. Friedman, C.J. Stone and R.A. Olshen, *Classification and regression trees*, CRC press (1984).

[304] T. Hastie, R. Tibshirani and J. Friedman, *The Elements of Statistical Learning*, Springer Series in Statistics, Springer New York Inc., New York, NY, USA (2001).